ISSN: 2160-049X Volume 8, Number 9, September 2018

Scientific Research Publishing

World Journal of Mechanics

ISSN: 2160-049X
9 772160 049007 09

www.scirp.org/journal/wjm

Journal Editorial Board

ISSN 2160-049X (Print) ISSN 2160-0503 (Online)

http://www.scirp.org/journal/wjm

Editors-in-Chief

Scientific Research Publishing

World Journal of Mechanics, 2018, 8, 311-415
http://www.scirp.org/journal/wjm
ISSN Online: 2160-0503
ISSN Print: 2160-049X

Table of Contents

Volume 8 Number 9 September 2018

World Journal of Mechanics (WJM)
Journal Information

SUBSCRIPTIONS

The *World Journal of Mechanics* (Online at Scientific Research Publishing, www.SciRP.org) is published monthly by Scientific Research Publishing, Inc., USA.

Subscription rates:
Print: $69 per issue.
To subscribe, please contact Journals Subscriptions Department, E-mail: sub@scirp.org

SERVICES

Advertisements
Advertisement Sales Department, E-mail: service@scirp.org

Reprints (minimum quantity 100 copies)
Reprints Co-ordinator, Scientific Research Publishing, Inc., USA.
E-mail: sub@scirp.org

COPYRIGHT

PRODUCTION INFORMATION

For manuscripts that have been accepted for publication, please contact:
E-mail: wjm@scirp.org

World Journal of Mechanics, 2018, 8, 311-342
http://www.scirp.org/journal/wjm
ISSN Online: 2160-0503
ISSN Print: 2160-049X

Reaction Forces on a Fixed Ladder in Static Equilibrium: Analysis and Definitive Experimental Test of the Ladder Problem

M. P. Silverman

Department of Physics, Trinity College, Hartford, USA
Email: mark.silverman@trincoll.edu

How to cite this paper: Silverman, M.P. (2018) Reaction Forces on a Fixed Ladder in Static Equilibrium: Analysis and Definitive Experimental Test of the Ladder Problem. *World Journal of Mechanics*, **8**, 311-342.
https://doi.org/10.4236/wjm.2018.89024

Received: August 2, 2018
Accepted: August 27, 2018
Published: August 30, 2018

Abstract

The development of a theoretical model to predict the four equilibrium forces of reaction on a simple ladder of non-adjustable length leaning against a wall has long remained an unresolved matter. The difficulty is that the problem is statically indeterminate and therefore requires complementary information to obtain a unique solution. This paper reports 1) a comprehensive theoretical analysis of the three fundamental models based on treating the ladder as a single Euler-Bernoulli beam, and 2) a detailed experimental investigation of the forces of reaction as a function of applied load and location of load. In contrast to previous untested proposals that the solution to the ladder problem lay in the axial constraint on compression or the transverse constraint on flexure, the experimental outcome of the present work showed unambiguously that 1) the ladder could be modeled the best by a pinned support at the base (on the ground) and a roller support at the top (at the wall), and 2) the only complementary relation needed to resolve the static indeterminacy is the force of friction at the wall. Measurements were also made on the impact loading of a ladder by rapid ascent and descent of a climber. The results obtained were consistent with a simple dynamical model of the ladder as a linear elastic medium subject to a pulse perturbation. The solution to the ladder problem herein presented provides a basis for theoretical extension to other types of ladders. Of particular importance, given that accidents involving ladders in the workplace comprise a significant fraction of all industrial accidents, the theoretical relations reported here can help determine whether a collapsed structure, against which a ladder was applied, met regulatory safety limits or not.

Keywords

Reaction Forces on a Ladder, Reaction Forces on a Beam, Impulse Load on a

Ladder, Ladder in Static Equilibrium, Statically Indeterminate Forces

1. Introduction: The Ladder Problem

Although determination of the reaction forces on a beam is a standard part of the mechanics of continuous media, the exact conditions under which an actual physical structure comprised of beams is stressed are not always apparent. Models based on different assumptions can predict hugely different reaction forces, and careful experimentation is required to determine which model may most accurately characterize a structure. One of the most important mechanical structures for which reaction forces need to be determined is that of a ladder. Although ladders have been in use since antiquity, to date no definitive model of the reaction forces on a ladder has been experimentally tested and confirmed. This paper reports what the author believes to be the most comprehensive theoretical analysis and definitive experimental test of the reaction forces on a fixed ladder.

1.1. The Fixed Ladder as an Euler-Bernoulli Beam

A fixed ladder is defined by the American Ladder Institute as a non-self-supporting ladder of fixed (*i.e.* non-adjustable) length [1]. It comprises two identical rails of uniform density connected by short rungs. As a suitable first approximation to modeling such a ladder, the rungs are ordinarily disregarded and the two rails are merged into a single uniform beam, such as shown in panel A of **Figure 1**. The single-beam ladder of length L is in static equilibrium supported obliquely by the flat horizontal ground and a flat vertical wall. The weight W of the ladder is regarded as a uniformly distributed load of linear density

$$w = W/L \tag{1}$$

that acts vertically downward at the center of mass of any isolated segment of the beam. A climber is modeled as a point load P acting vertically downward at a distance βL $(1 \geq \beta \geq 0)$ along the beam from the contact point at the ground, which is taken to be the origin.

As shown in panel A of the figure, there are four reaction forces: 1) normal force at the ground (R_1), 2) parallel force at the ground (R_2), 3) normal force at the wall (R_3), and 4) parallel force at the wall (R_4). The prediction of these four forces constitutes what is called the ladder problem. Before discussing the theoretical solutions and experimental test of the ladder problem, it is worthwhile to consider why the problem is a significant one. This significance is both conceptual and practical.

First, conceptually, the solution to any model serving as an archetype for a class of real-world problems within some branch of physics is significant by virtue of its fundamentality. The single-beam ladder is an archetype within the mechanics of continuous media. Moreover, understanding the forces on a fixed

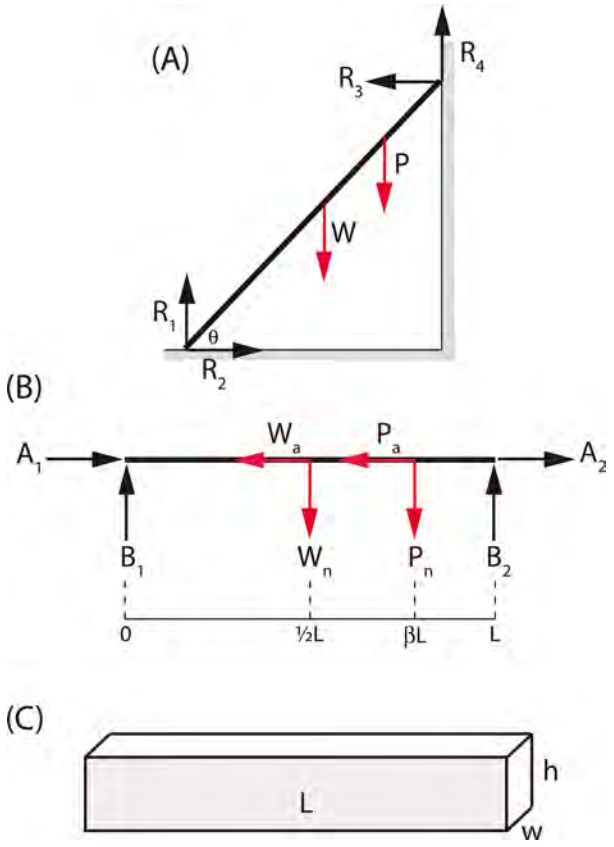

Figure 1. (A) Schematic diagram of the reaction forces (R_1, R_2, R_3, R_4) on a single-beam ladder by the ground and wall. W is the beam weight acting at the center of mass $L/2$; P is a point load applied at the point βL; (B) Decomposition of forces to show axial (A_1, A_2) and normal (B_1, B_2) components relative to the long axis of the beam. Subscript 1 denotes the contact point at the ground; subscript 2 denotes the contact point at the wall.

ladder would provide useful modeling guidelines for predicting the reaction forces on more complex ladder types, such as extension ladders, step ladders, trestle ladders, and others. Second, from a practical standpoint, the ability to predict the forces on ladders has direct impact on matters relating to safety in the use of ladders and to legal issues that arise when use of a ladder in the workplace results in injury or death. For example, with a valid fixed ladder model, the analyst can determine the acceptable range of inclination angles to avoid slippage, or determine whether the net force exerted by a ladder on a wall or railing that collapsed was within or exceeded regulatory limits [2].

One might think that prediction of the reaction forces on a structure as simple as a single-beam ladder is a relatively straightforward matter. Indeed, the problem is trivially solvable if the parallel reaction at the wall is ignored, which is the case in countless physics textbooks (see, for example, [3]) and expository internet articles. The fixed ladder leaning against a frictionless wall has been an iconic example of static equilibrium in elementary mechanics books for at least a century. This problem is statically determinate; *i.e.* the three reaction forces

(R_1, R_2, R_3) are uniquely solvable from the three equations of static equilibrium in which the net horizontal force, net vertical force, and rotational moment about any point at rest all vanish. The resulting solution, however, is of academic interest only and does not describe correctly the interactions of real ladders with real surfaces.

When account is taken of the parallel reaction at the wall, the problem becomes statically *indeterminate*, and therefore more complicated, since there are now 4 unknowns and 3 equations. One proposed solution assumed that the ladder undergoes an axial deformation which is constrained by the supports [4]. This model cannot be correct as it stands because the transverse (bending) deformation—as calculated in Section 2—is approximately two orders of magnitude greater than the axial deformation and should not have been neglected. Another proposal [5] took account of both axial compression and transverse flexion, and concluded that the problem could not be solved by static analysis because it was not possible to determine which deformation dominated. This conclusion is not substantiated by the findings of the present paper. Neither of these proposals provided experimental measurements to test their validity.

Experimentally, there have been many investigations, of which some representative examples are [6] [7] [8], to elucidate the conditions under which ladders can be used safely. In general, these investigations focused on matters relating to friction, angle of inclination, climbing speed, weight of climber, and other empirically accessible variables, but did not attempt to provide a model that would succinctly incorporate these data in a mathematical theory.

This paper reports the theoretical solution of three basic models by which to analyze the reaction forces of a fixed ladder represented as a single Euler-Bernoulli (E-B) beam. The characteristics of an E-B beam pertinent to the present study are as follows [9]:

1) the length of the beam is much greater than the linear dimension of the cross-section;

2) the long axis of the beam lies within the neutral surface;

3) the cross section of the beam remains plane and perpendicular to the long axis during deflection;

4) deformation of the cross section within its own plane is neglected;

5) the beam is a linear elastic material subject to Hooke's law; *i.e.* normal stress within a cross section varies linearly with perpendicular distance from the neutral axis.

The *neutral surface* of a beam is the interface that separates the fibers under compression from the fibers under tension when the beam is deflected transversely. The *neutral axis* within any cross section is the line of intersection of the neutral surface with the cross section.

1.2. The Analytical Models

The three basic ladder models analyzed in this paper are distinguished by the nature of the supports at the points of contact with the surfaces of the ground

and wall. In the mechanics of beams, the three common types of supports are 1) roller, 2) pin, and 3) fixed [10]. The names refer to the constraints on the motion of the affected segment of the beam, and not necessarily to the actual presence of a roller, pin, or clamping mechanism. Thus, if one end of a beam is supported by a roller, it can displace laterally, but not vertically. If the end of the beam is pinned, it cannot displace either laterally or vertically, but it can rotate about the pin. And, finally, if the end is fixed, it cannot displace or rotate at all. [There is a fourth kind of support usually designated as simple, which is idealized as a frictionless surface. This would apply to the support of the single-beam ladder at a wall as treated in the elementary physics books.]

If a right-handed Cartesian coordinate system (x, y, z) is chosen such that an initially horizontal beam lies along the x axis, and a load is applied that can deflect the beam vertically downward along the negative y axis, then the boundary and continuity conditions at the three kinds of supports can be summarized as follows

$$\begin{aligned} &\text{Roller}: \quad \Delta y = 0,\ \mathrm{d}y/\mathrm{d}x \neq 0,\ M_z = 0 \\ &\text{Pin}: \quad\ \Delta y = 0,\ \mathrm{d}y/\mathrm{d}x \neq 0,\ M_z = 0 \\ &\text{Fixed}: \quad \Delta y = 0,\ \mathrm{d}y/\mathrm{d}x = 0,\ M_z \neq 0 \end{aligned} \tag{2}$$

where the symbol Δ signifies displacement, and M_z is an internal bending moment (torque) about the z axis. The salient features of relations (2) are that a) the displacement and slope of the deflected beam are zero at a fixed support but the support creates an internal bending moment, whereas b) at roller and pin supports there is no internal moment, and the slope of the bending curve there need not be zero.

The models analyzed in this paper are based on the supports described by Equation (2).

- In Model 1, the ground support of the single-beam ladder is fixed and the wall support is equivalent to a pin. Under a vertical load due to the distributed weight of the ladder and the point weight of a hypothetical climber, the ladder is subject to both axial and transverse stresses, but is constrained from compression, elongation, or rotation at the supports. This is a case of static indeterminateness in two variables: one axial and one transverse. Although friction is presumably the source of the constraints, no specific assumptions are made in regard to the mathematical form of the frictional force.
- In Model 2, the ground support of the single-beam ladder is fixed, and the wall support is equivalent to a roller. The axial component of the load can compress the ladder, and thereby remove the static indeterminateness along the length. The reaction at the wall is assumed to be governed by the phenomenological relation for friction taken to be proportional to the normal force at the wall [11]. There remains a static indeterminateness in one of the transverse reactions because of the unknown internal moment at the ground support.
- In Model 3, the ground support of the single-beam ladder is equivalent to a

pin and the wall support is equivalent to a roller. The ladder is free to compress under an axial force and flex about the ground support, thereby relieving all static constraints. The reaction at the wall is assumed governed by friction as in Model 2. This is a case of static indeterminateness in one variable in which the equations of static equilibrium, complemented by the frictional force law, suffice to determine a unique solution.

The three models are schematically illustrated in Figure 2.

1.3. Outline of Paper

In Section 2 the reaction forces on a ladder characterized as a single E-B beam are calculated for each model and examined as a function of load, location of load along the ladder, and angle of inclination of the ladder with respect to the ground. In the case of Models 1 and 3, the full bending curve is calculated within the Euler-Bernoulli approximation (neglect of the square of the slope dy/dx), and the magnitudes of transverse and axial deformations are compared. (The bending curve of Models 2 and 1 are the same).

In Section 3 are reported experiments using horizontal and vertical force platforms to measure the reactions on a fixed metal ladder inclined against a wall. It is noted here briefly that the model that was found to account for the observed results was Model 3.

In Section 4 the impact loading on a ladder by a climber is examined theoretically and experimentally.

In Section 5 are reported measurements of the reactions on a wood beam inclined obliquely against a wall. The intent of the experiment was to ascertain whether the same theoretical model that best applied to a ladder *modeled as a beam* applied as well to an actual single beam.

In Section 6 conclusions drawn from this research are summarized.

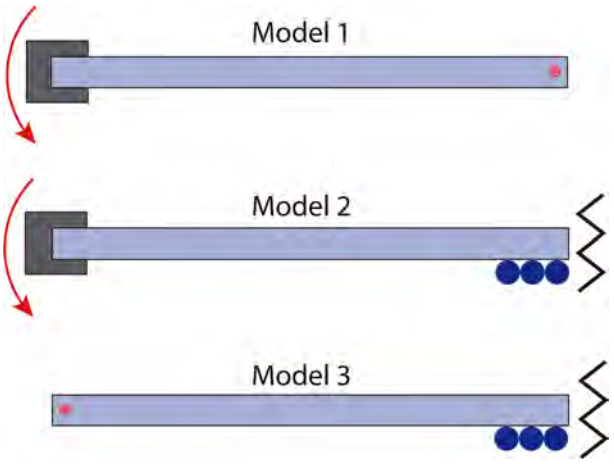

Figure 2. Schematic diagram symbolizing the supports upon which each model is based: gray clamp = fixed support; red solid circle = pin support; 3 blue circles = roller. The fixed support is accompanied by an internal moment (red arc). The zigzag line symbolizes friction. The light blue bar represents the single-beam ladder as portrayed horizontally in panel B of Figure 1.

2. Analysis of a Single-Beam Fixed Ladder

Panel A of Figure 1 shows the disposition of the reaction forces on the ladder as it appears inclined against a vertical wall at an angle θ to the ground. Because the material out of which an actual ladder is constructed—primarily aluminum, fiberglass, or wood—has a relatively high elastic modulus ($E_{\mathrm{Al}} \sim 69$ GPa, $E_{\mathrm{FG}} \sim 72$ GPa, $E_{\mathrm{wood}} \sim 10\text{-}13$ GPa) [12] [13] [14], the deformation is ordinarily small, and one can analyze the axial and transverse deformations independently provided the axial force is not excessively large [15]. Thus, by taking appropriate components, one obtains the axial and transverse reaction forces shown in panel B of Figure 1, which are related to the forces normal and parallel to the ground and wall as follows

$$\begin{aligned} A_1 &= R_1 \sin\theta + R_2 \cos\theta \\ B_1 &= R_1 \cos\theta - R_2 \sin\theta \\ A_2 &= -R_3 \cos\theta + R_4 \sin\theta \\ B_2 &= R_3 \sin\theta + R_4 \cos\theta \end{aligned} \tag{3}$$

with inverse relations

$$\begin{aligned} R_1 &= B_1 \cos\theta + A_1 \sin\theta \\ R_2 &= -B_1 \sin\theta + A_2 \cos\theta \\ R_3 &= -B_2 \sin\theta - A_2 \cos\theta \\ R_4 &= B_2 \cos\theta + A_2 \sin\theta \end{aligned} \tag{4}$$

The equations of static equilibrium then take either of the forms

$$\text{(I)} \quad \begin{aligned} R_1 + R_4 &= W + P \\ R_2 - R_3 &= 0 \end{aligned} \qquad \text{(II)} \quad \begin{aligned} B_1 + B_2 &= W_n + P_n \\ A_1 + A_2 &= W_a + P_a \end{aligned} \tag{5}$$

in which the normal and axial components of the ladder weight and a point load representative of a climber are respectively

$$\begin{aligned} W_n &= W\cos\theta & W_a &= W\sin\theta \\ P_n &= P\cos\theta & P_a &= P\sin\theta. \end{aligned} \tag{6}$$

The sets of equations in (5) do not contain an equation for the vanishing of a rotational moment about a designated point at rest. In the absence of information regarding the supports of the ladder at the ground, it is not possible to write a torque equation based on static equilibrium alone. This is a consequence of the fact that the system may contain an initially unknown internal moment created by the ground support in order to maintain static equilibrium.

Since there are four unknown reactions in Equation (5) and fewer than four equations of static equilibrium, the set of equations is statically indeterminate and must be supplemented by what are termed complementary conditions. Under the circumstances stated above, these conditions can be applied to the axial and normal directions independently. The complementary conditions take different forms depending on the specific model, as discussed in the following subsections.

2.1. Model 1: Fixed Ground and Pinned Wall Supports

With respect to the schematic diagram in panel B of **Figure 1**, Model 1 entails a fixed support at the left end $x=0$ (with initially unknown internal moment $M_z(0)$) and a pin support at the right end $x=L$. The total strain energy U of the beam

$$U = U_a + U_b \tag{7}$$

is the sum of the axial strain energy

$$U_a = \frac{1}{2EA}\int_0^L F_a(x)^2\,\mathrm{d}x \tag{8}$$

due to the compression or tension by force $F_a(x)$ and the energy of flexure (bending)

$$U_b = \frac{1}{2EI_z}\int_0^L M_z(x)^2\,\mathrm{d}x \tag{9}$$

due to the moment $M_z(x)$ about the z axis (see Ref. [15], pp 188-196). The material parameters in Equations (8) and (9) are the beam cross section area A, beam area moment of inertia I_z about the transverse z axis, and the elastic modulus (Young's modulus) E. For a beam of width w and height h as portrayed in panel C of **Figure 1**, the cross section and area moment of inertia take the forms (see [15], pp 448-449)

$$A = wh \tag{10}$$

$$I_z = \frac{1}{12}wh^3. \tag{11}$$

Because the overall load comprises both distributed and point contributions, the force $F_a(x)$ and moment $M_z(x)$ are piecewise continuous functions. These functions can be represented economically by use of the Heaviside unit step function [16] defined here as

$$H(x-x_0) = \begin{cases} 0 & x < x_0 \\ 1 & x \geq x_0. \end{cases} \tag{12}$$

Mathematically, the Heaviside function is usually defined by pure inequalities in both partitions of the real axis and left undefined at the point where the argument is zero. In the mechanics of continuous media, however, the point load occurs at the partition between segments and therefore it is more useful to define the Heaviside function as unity there. One can then express the axial force and bending moment in the following ways

$$F_a(x) = A_2 - \frac{W_a}{L}(L-x) - P_a H(\beta L - x) \tag{13}$$

$$M_z(x) = B_2(L-x) - \frac{W_n}{2L}(L-x)^2 - P_n(\beta L - x)H(\beta L - x). \tag{14}$$

From the complementary energy theorem (Castigliano's theorem) of continuum mechanics (see [15] pp 201-217) for systems where the force-deformation

relation is linear, the deflection of a point i on a beam in the direction of a load F_i applied at that point is given by

$$\delta_i = \frac{\partial U}{\partial F_i}. \tag{15}$$

Since a physical condition of Model 1 is that the right endpoint of the beam in panel B of Figure 1 suffers no deflection, it follows that

$$\delta_L^{(a)} = \frac{\partial U}{\partial A_2} = 0 \tag{16}$$

and

$$\delta_L^{(b)} = \frac{\partial U}{\partial B_2} = 0 \tag{17}$$

where superscript a signifies axial and superscript b signifies bending. Equations (16) and (17) are the complementary relations required to supplement the set of relations (5) and resolve the static indeterminacy of Model 1.

Substitution of relations (13) and (14) respectively into strain energies (8) and (9), taking derivatives (16) and (17), and setting the resulting integrals to zero lead to expressions for the axial reaction A_2 and transverse reaction B_2. The reactions A_1 and B_1 are then obtained from Equation (5) of static equilibrium. The resulting set of four axial and transverse reactions are found to be

$$\begin{aligned} A_1 &= \frac{1}{2}W\sin\theta + (1-\beta)P\sin\theta \\ A_2 &= \frac{1}{2}W\sin\theta + \beta P\sin\theta \\ B_1 &= \frac{5}{8}W\cos\theta + \left(1 - \frac{3}{2}\beta^2 + \frac{1}{2}\beta^3\right)P\cos\theta \\ B_2 &= \frac{3}{8}W\cos\theta + \left(\frac{3}{2}\beta^2 - \frac{1}{2}\beta^3\right)P\cos\theta \end{aligned} \tag{18}$$

from which follow by transformation (4) the reactions normal and parallel with respect to the ground and wall

$$\begin{aligned} R_1 &= \frac{1}{2}W\left(1 + \frac{1}{4}\cos^2\theta\right) + P\left[1 - \left(\frac{3}{2}\beta^2 - \frac{1}{2}\beta^3\right)\cos^2\theta - \beta\sin^2\theta\right] \\ R_2 &= R_3 = \left[\frac{1}{16}W + \left(\frac{1}{2}\beta - \frac{3}{4}\beta^2 + \frac{1}{4}\beta^4\right)P\right]\sin 2\theta \\ R_4 &= \frac{1}{2}W\left(1 - \frac{1}{4}\cos^2\theta\right) + P\left[\left(\frac{3}{2}\beta^2 - \frac{1}{2}\beta^3\right)\cos^2\theta + \beta\sin^2\theta\right]. \end{aligned} \tag{19}$$

The directions of R_2 and R_3 are shown in Figure 1, and no algebraic sign denoting direction is needed since these two forces are not superposed in any calculation in this paper.

Figure 3 shows the variation in normal force at the ground (panel A) and at the wall (panel B) as a function of the fractional location $(1 \geq \beta \geq 0)$ of the applied load along the beam for different load magnitudes ranging from 0 to 100

pounds (lbs). The ladder weight is taken to be 25 lbs (111.2 N), in accordance with the use of English units in ladder specifications given in the US, but calculations are performed and recorded in metric units (newtons N). The angle of inclination was taken to be 60˚. Plots of the parallel force at the ground (R_2) and at the wall (R_4) are not shown since by relations (18) the former are the same as the plots in panel B, and the latter correspond to reversing the horizontal scale (abscissa) in panel A.

A complementary perspective is given in Figure 4, which shows the variation in normal force at the ground (panel A) and at the wall (panel B) as a function of the angle of inclination for different fractional locations of the applied load along the beam. According to Model 1, the location of a hypothetical climber (of

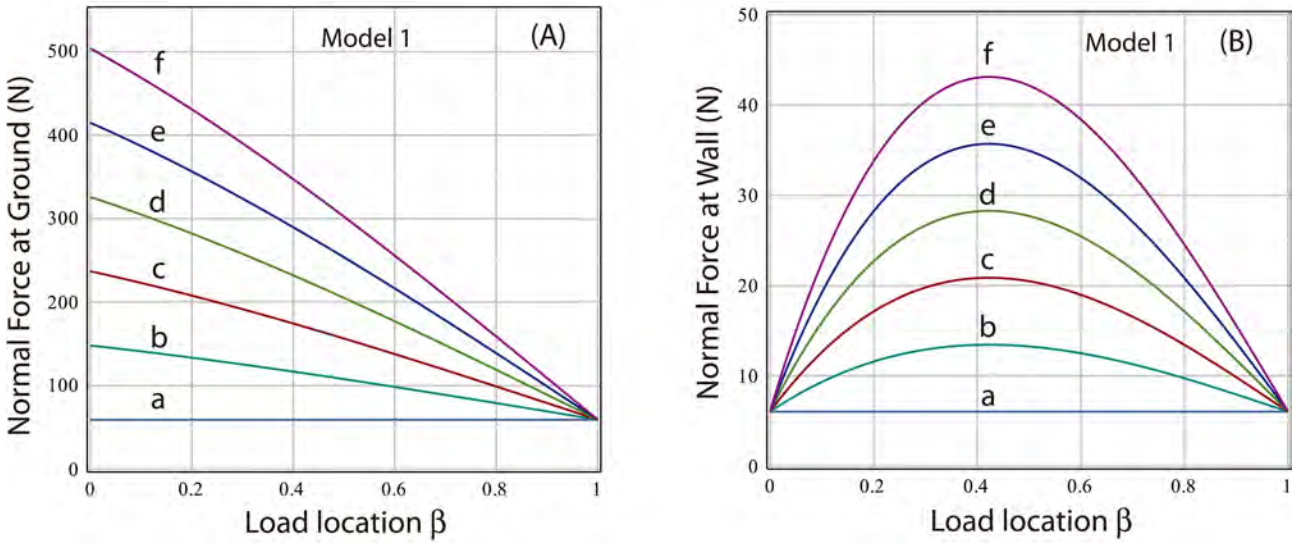

Figure 3. Model 1 variation in normal force at (A) ground and (B) wall as a function of load location for loads (in lbs): (a) 0, (b) 20, (c) 40, (d) 60, (e) 80, (f) 100. The ordinate unit is in newtons. Ladder weight is 25 lbs; angle of inclination is 60˚.

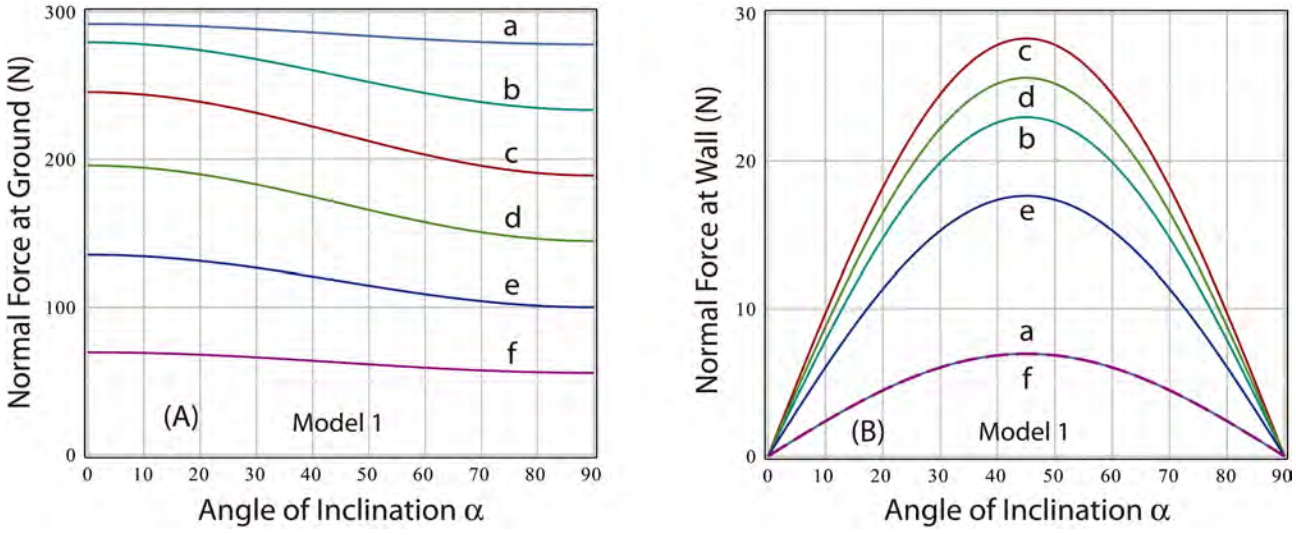

Figure 4. Model 1 variation in normal force at (A) ground and (B) wall as a function of inclination angle for load locations β: (a) 0.0, (b) 0.2, (c) 0.4, (d) 0.6, (e)).8, (f) 1.0. Ladder weight is 25 lbs; point load is 50 lbs.

fixed weight) influences the normal reaction at the wall strongly and the normal reaction at the ground relatively weakly as the inclination of the ladder is changed.

Applying Equation (15) to the total strain energy U, one can determine the deformation at any point in the elastic curve of the single-beam ladder and thereby compare the magnitudes of the axial compression $\delta^{(a)}$ and transverse (bending) deflection $\delta^{(b)}$. Taking $\beta = \frac{1}{2}$ for illustration yields the deformations

$$\delta^{(a)}_{\frac{1}{2}L} = \left.\frac{\partial U}{\partial P_a}\right|_{\beta=\frac{1}{2}} = \frac{L}{2AE}(W+P)\sin\theta \tag{20}$$

$$\delta^{(b)}_{\frac{1}{2}L} = \left.\frac{\partial U}{\partial P_n}\right|_{\beta=\frac{1}{2}} = \frac{L^3}{768EI_z}(4W+7P)\cos\theta\,. \tag{21}$$

Given typical parameters of beam length $L = 2.5$ m, width $w = 2$ cm, height $h = 5$ cm, inclination angle $\theta = 45^\circ$, ladder weight $W = 25$ lbs (111.2 N), climber weight $P = 150$ lbs (667.2 N), and elastic modulus of aluminum $E = 69$ GPa, Equations (20) and (21) lead to deformations $\delta^{(a)}_{\frac{1}{2}L} \approx 10$ μm, $\delta^{(b)}_{\frac{1}{2}L} \approx 5.1$ mm. The deformation due to bending is approximately 500 times the deformation due to axial compression. Therefore, any model of a ladder subject to ordinary loads that takes account of axial deformation cannot neglect deformation due to flexure.

As a final consideration, it is useful to derive the deflection curve of Model 1 as a check on the calculated deformations and to ascertain that the reactions of a single-beam ladder derived from Model 1 correctly fulfill the complementary conditions. The exact flexure formula for an E-B beam relates the bending moment to the radius of curvature and takes the form of a nonlinear second-order differential equation (see [10] pp. 576-583)

$$\frac{\mathrm{d}^2y/\mathrm{d}x^2}{\left[1+(\mathrm{d}y/\mathrm{d}x)^2\right]^{3/2}} = \frac{1}{EI_z}M_z(x) \tag{22}$$

whose solution is called the elastica [17]. Although an exact solution would be required for a highly flexible beam such as a fishing rod [9], the deflection of the rail of a ladder is sufficiently low that one can neglect the square of the slope in the denominator of Equation (22), as is conventionally done in engineering practice. The equation then becomes linear and can be readily solved subject to the imposed boundary conditions

$$\begin{aligned} &y(0) = y(L) = 0 \\ &y(x) \text{ is continuous at } x = \beta L \\ &\mathrm{d}y/\mathrm{d}x \text{ is continuous at } x = \beta L \end{aligned} \tag{23}$$

to yield the piecewise continuous function

$$y(x) = y_1(x)H(\beta L - x) + y_2(x)H(x - \beta L) \tag{24}$$

with

$$\begin{aligned} y_1(x)_{\text{Model 1}} &= \frac{1}{EI_z}\left[-L\left(\frac{1}{16}W_n + \left(\frac{1}{2}\beta - \frac{3}{4}\beta^2 + \frac{1}{4}\beta^3\right)P_n\right)x^2\right. \\ &\left. + \left(\frac{5}{48}W_n + \frac{1}{6}\left(1 - \frac{3}{2}\beta^2 + \frac{1}{2}\beta^3\right)P_n\right)x^3 - \frac{W_n}{24L}x^4\right] \\ y_2(x)_{\text{Model 1}} &= \frac{1}{EI_z}\left[\frac{1}{6}\beta^3 L^3 P_n - \frac{1}{2}\left(\beta^2 L^2 P_n\right)x + L\left(-\frac{1}{16}W_n + \left(\frac{3}{4}\beta^2 - \frac{1}{4}\beta^3\right)P_n\right)x^2\right. \\ &\left. + \left(\frac{5}{48}W_n - \frac{1}{6}\left(\frac{3}{2}\beta^2 - \frac{1}{2}\beta^3\right)P_n\right)x^3 - \frac{W_n}{24L}x^4\right]. \end{aligned} \tag{25}$$

Figure 5 shows plots of the deflection curve $y(x)$ for different locations of a 150 lb load on a ladder 2.5 m in length and 25 lbs in weight inclined at an angle of 45˚ against a vertical wall. The cross section of the single beam is $2\text{ cm} \times 5\text{ cm}$ and the modulus of elasticity is $E = 69$ GPa. As seen in the figure, the deflection curve is the same for a load directly at the base $x = 0$ or at the top of the ladder $x = L$. The deflection $\delta_{\frac{1}{2}L}^{(b)} \sim 5.1$ mm occurs at the mid-position $\beta = \frac{1}{2}$, which is the result predicted by Equation (21) obtained by Castigliano's theorem. The deflection curve is not symmetric for any location of the load, even at mid-position, because the slope is required to be 0 at the ground support (left end) but not at the wall support (right end).

Calculation of deflections (20), (21) and the elastica curve (24) involved

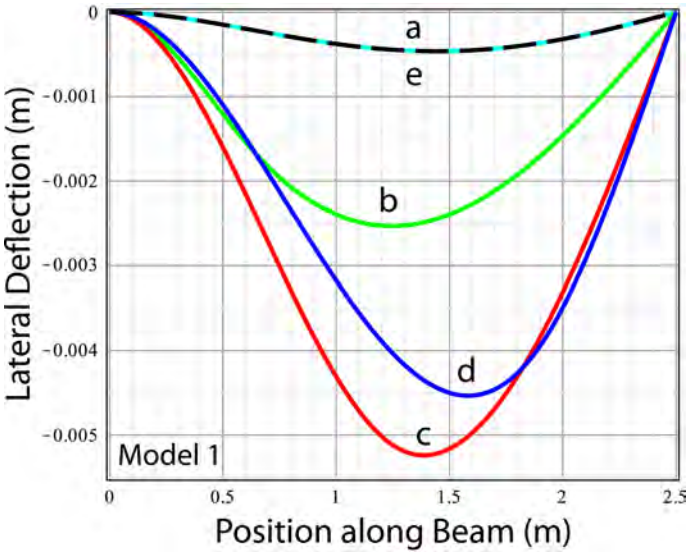

Figure 5. Deflection curves of the Model 1 single-beam ladder of length 2.5 m and weight 25 lbs for a point load of 150 lbs at fractional lengths β along the beam of (a) 0 [ground point], (b) 1/4, (c) 1/2, (d) 3/4, (e) 1 [wall point] (note that plots (a) (solid line) and (e) (dashed line) overlap). The inclination angle of the ladder was taken to be 45˚. Material parameters are $E = 69$ GPa, $A = 2 \times 5\text{ cm}^2$, $I_z = \frac{1}{12}(2\text{ cm})(5\text{ cm})^3$

integration of expressions of the form $x^n H\left(x-x_0\right)$ for non-negative integer n. The integration of Heaviside functions is summarized in the **Appendix**.

2.2. Model 2: Fixed Ground and Roller Wall Supports

With respect to the schematic diagram in panel B of Figure 1, Model 2 entails a fixed support at the left end and a roller support at the right end. Resolution of the static indeterminateness of the bending reactions is accomplished in exactly the same way as for Model 1, and therefore forces B_1 and B_2 are given as shown in Equations (18). To determine the other forces, one makes use of the transformation (3) for B_2 and the phenomenological relation for friction

$$R_4 = \mu R_3 \tag{26}$$

with coefficient of friction μ to obtain

$$B_2 = R_3 \sin\theta + R_4 \cos\theta = R_3\left(\sin\theta + \mu\cos\theta\right), \tag{27}$$

from which follows

$$R_3 = R_2 = \frac{R_4}{\mu} = \frac{\frac{3}{8}W + \left(\frac{3}{2}\beta^2 - \frac{1}{2}\beta^3\right)P}{\tan\theta + \mu} \tag{28}$$

and therefore from Equation (5)

$$R_1 = W + P - R_4 = W + P - \mu R_3 = W + P - \mu\left[\frac{\frac{3}{8}W + \left(\frac{3}{2}\beta^2 - \frac{1}{2}\beta^3\right)P}{\tan\theta + \mu}\right]. \tag{29}$$

The axial forces A_1 and A_2 are given by the transformation (3)

$$\begin{aligned} A_1 &= \left(W + P\right)\sin\theta + \left(\frac{3}{8}W + \left(\frac{3}{2}\beta^2 - \frac{1}{2}\beta^3\right)P\cos\theta\right)\left[\frac{1-\mu\tan\theta}{\tan\theta+\mu}\right] \\ A_2 &= -\left(\frac{3}{8}W + \left(\frac{3}{2}\beta^2 - \frac{1}{2}\beta^3\right)P\cos\theta\right)\left[\frac{1-\mu\tan\theta}{\tan\theta+\mu}\right] \end{aligned} \tag{30}$$

rather than by a complementary condition constraining axial compression.

Figure 6 shows the variation in normal force at the ground (panel A) and at the wall (panel B) as a function of load location for different loads under the same conditions as for Figure 3. The coefficient of friction was taken to be 0.4. Correspondingly, Figure 7 shows the variation in these two reactions as a function of angle of inclination with the ground under the same conditions as for Figure 4. Models 1 and 2 are seen to predict reactions that depend very differently on load location.

Since the reaction forces normal to the beam $\left(B_1, B_2\right)$ are the same as for Model 1, the bending deflection curve, which does not depend on the axial reactions, is also the same.

2.3. Model 3: Pinned Ground and Roller Wall Supports

With respect to the schematic diagram in panel B of Figure 1, Model 3 entails a

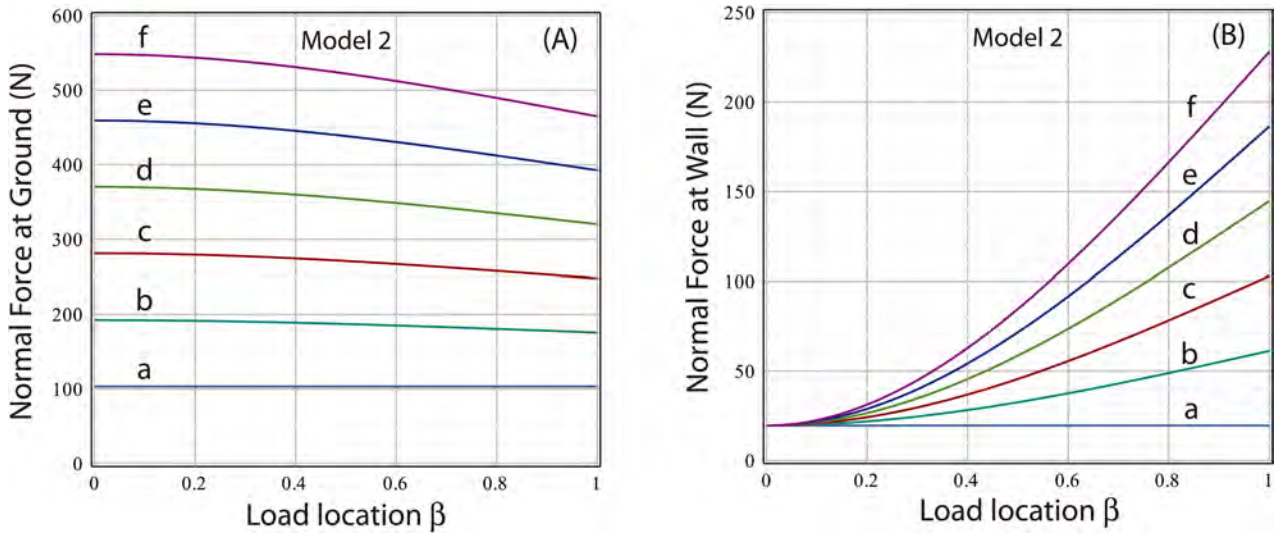

Figure 6. Model 2 variation in normal force at (A) ground and (B) wall as a function of load location for loads (in lbs): (a) 0, (b) 20, (c) 40, (d) 60, (e) 80, (f) 100. The weight and angle are the same as in **Figure 3**; the coefficient of friction is 0.4.

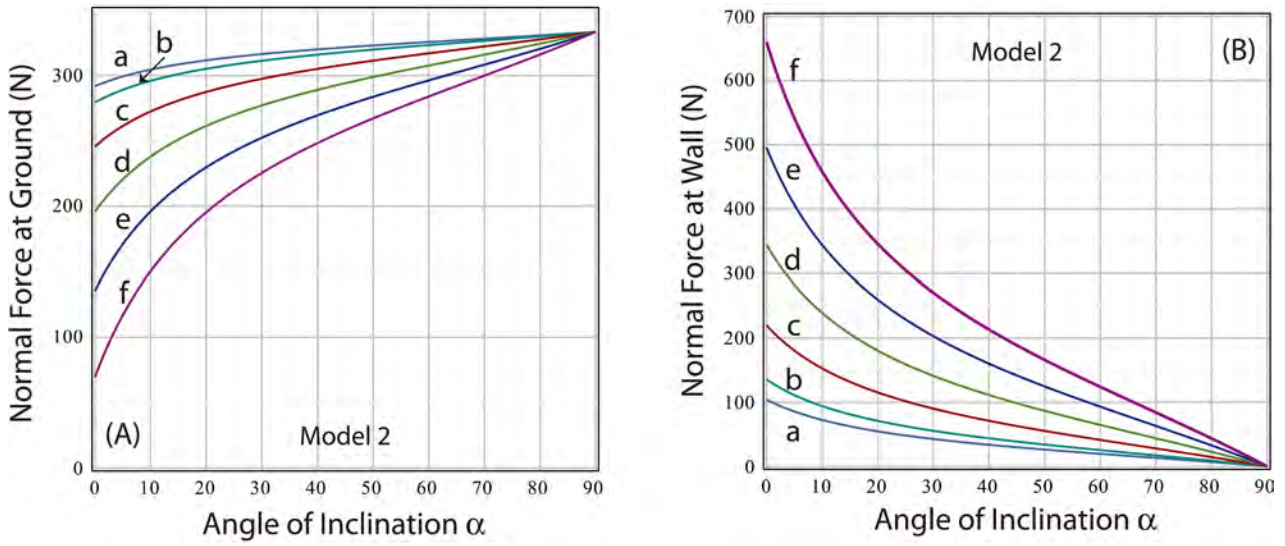

Figure 7. Model 2 variation in normal force at (A) ground and (B) wall as a function of inclination angle for load locations β: (a) 0.0, (b) 0.2, (c) 0.4, (d) 0.6, (e)).8, (f) 1.0. The weight and load are the same as in **Figure 4**; the coefficient of friction is 0.4.

pinned support at the left end and a roller support at the right end. Because there is no unknown internal moment at pinned and roller supports, the set of equations (5) can be supplemented by an equation for the vanishing of the external moment M_z about any fixed point. For example, if the pivot is taken to be the point of contact with the ground, then the vanishing of $M_z(0)$ can be expressed by either of the equations

$$R_3 \sin\theta + R_4 \cos\theta = \frac{1}{2} W \cos\theta + \beta P \cos\theta \tag{31}$$

or

$$B_2 = \frac{1}{2} W_n + \beta P_n . \tag{32}$$

Together with the complementary relation (26) for force of friction and the other equations of static equilibrium, one obtains

$$R_3 = R_2 = \frac{R_4}{\mu} = \frac{\frac{1}{2}W + \beta P}{\tan\theta + \mu} \tag{33}$$

$$B_1 = \frac{1}{2}W_n + (1-\beta)P_n \tag{34}$$

and

$$R_1 = W + P - \mu R_3 = \frac{W\left(\tan\theta + \frac{1}{2}\mu\right) + P\left(\tan\theta + (1-\beta)\mu\right)}{\tan\theta + \mu}. \tag{35}$$

From the set of transformations (3) follow the axial reactions

$$\begin{aligned} A_1 &= (W+P)\sin\theta + \left(\frac{3}{8}W + \left(\frac{3}{2}\beta^2 - \frac{1}{2}\beta^3\right)P\cos\theta\right)\left[\frac{1-\mu\tan\theta}{\tan\theta+\mu}\right] \\ A_2 &= -\left(\frac{3}{8}W + \left(\frac{3}{2}\beta^2 - \frac{1}{2}\beta^3\right)P\cos\theta\right)\left[\frac{1-\mu\tan\theta}{\tan\theta+\mu}\right] \end{aligned} \tag{36}$$

Figure 8 and Figure 9 respectively show the variation in normal force at the ground (panel A) and at the wall (panel B) as a function of load location along the ladder and as a function of inclination angle with the ground. The plots are similar to, but not numerically identical with, the plots of Figure 6 and Figure 7.

The bending curve (elastica) of Model 3 takes a different shape than that of Models 1 and 2 because of the difference in the nature of the support at the ground. Solving the Euler-Bernoulli approximation to the flexure equation (22)

$$\mathrm{d}^2 y/\mathrm{d}x^2 = M_z(x)/EI_z \tag{37}$$

with moment (see panel B of Figure 1)

$$M_z(x) = B_1 x - \frac{W_n}{2L}x^2 - P_n(x-\beta L)H(x-\beta L) \tag{38}$$

and boundary conditions (23) leads to the piecewise continuous function (24) with components

$$\begin{aligned} y_1(x)_{\text{Model 3}} &= \frac{1}{EI_z}\left[-L^2\left(\frac{1}{24}W_n + \left(\frac{1}{3}\beta - \frac{1}{2}\beta^2 + \frac{1}{6}\beta^3\right)P_n\right)x \right. \\ &\quad \left. + \left(\frac{1}{12}W_n + \frac{1}{6}(1-\beta)P_n\right)x^3 - \frac{W_n}{24L}x^4\right] \\ y_2(x)_{\text{Model 3}} &= \frac{1}{EI_z}\left[\frac{\beta^3 L^3}{6}P_n - L^2\left(\frac{1}{24}W_n + \left(\frac{1}{3}\beta + \frac{1}{6}\beta^3\right)P_n\right)x + \left(\frac{1}{2}\beta L P_n\right)x^2 \right. \\ &\quad \left. + \left(\frac{1}{12}W_n - \frac{1}{6}\beta P_n\right)x^3 - \frac{W_n}{24L}x^4\right] \end{aligned} \tag{39}$$

Figure 10 shows plots of the deflection curve $y(x)$ for different locations of a 150 lb load on a ladder 2.5 m in length and 25 lbs in weight inclined at an angle of 45˚ against a vertical wall. As seen in the figure, the deflection curve is again

the same for a load directly at the base $x=0$ or at the top of the ladder $x=L$. In contrast to the deflection curves of Models 1 and 2, the deflection curve of Model 3 is symmetric for a load applied at the middle of the beam; the slopes are nonzero and equal at both the ground and wall contact points. For other locations of the load, the deflection curve is no longer symmetric, but at no location are the slopes zero at the end points.

The maximum deflection $\delta_{\frac{1}{2}L}^{(b)} \sim 11.8$ mm occurs at the mid-position $\beta = 1/2$. This is the same result one would get from applying Castigliano's theorem, as implemented in Section 2.1, which leads to the deformation

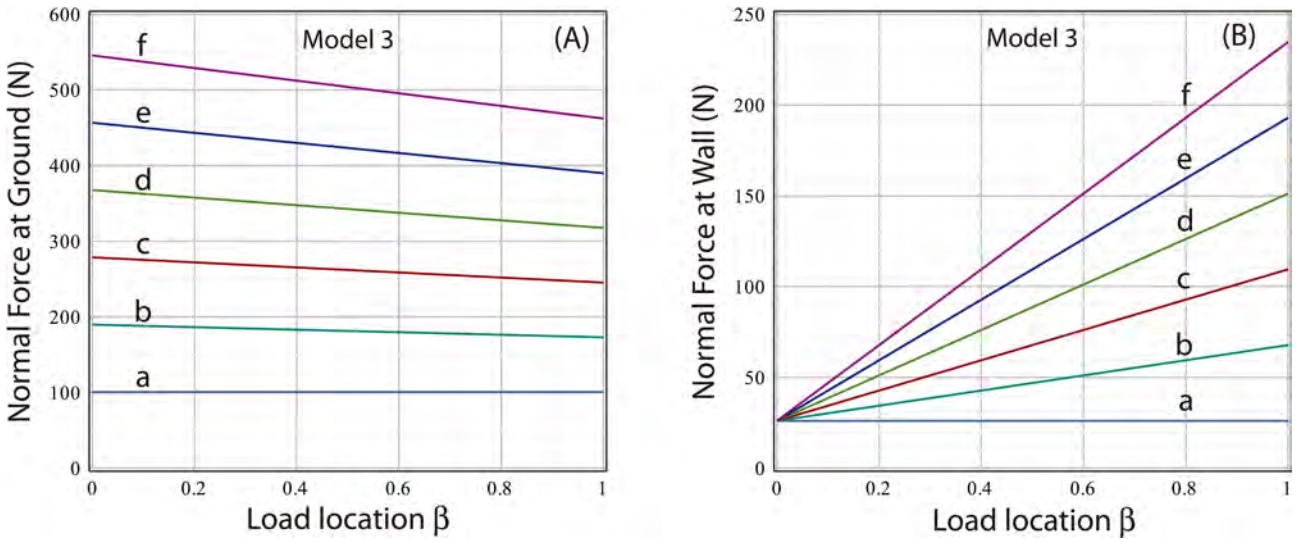

Figure 8. Model 3 variation in normal force at (A) ground and (B) wall as a function of load location for loads (in lbs): (a) 0, (b) 20, (c) 40, (d) 60, (e) 80, (f) 100. The weight and angle are the same as in Figure 3; the coefficient of friction is 0.4.

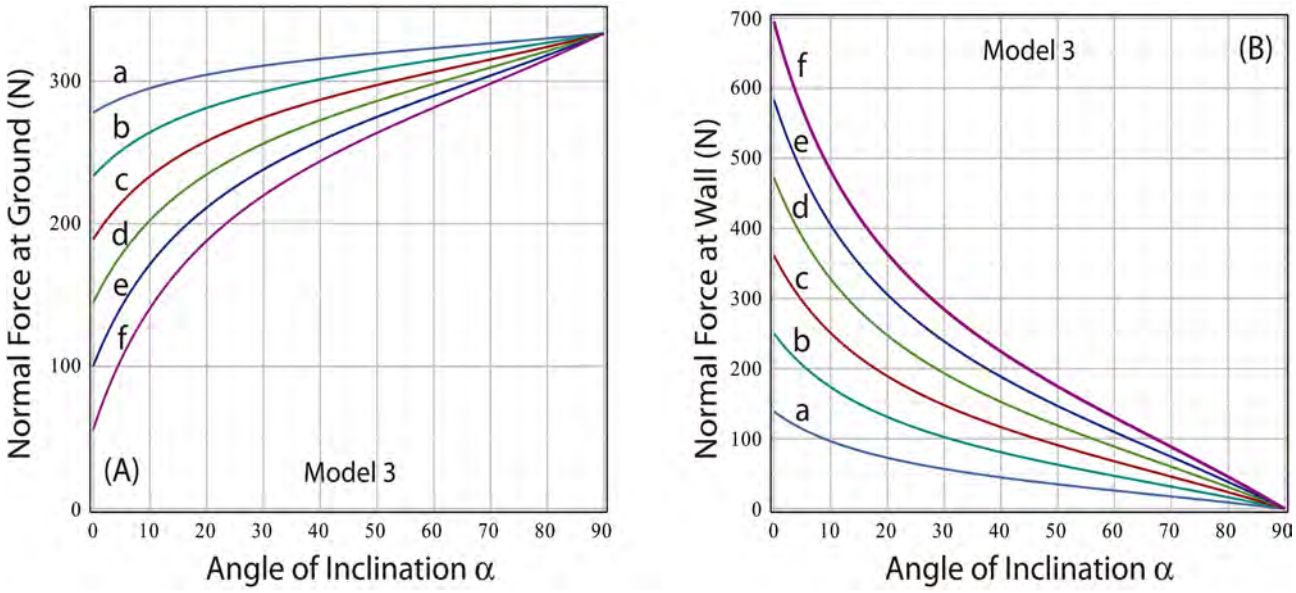

Figure 9. Model 3 variation in normal force at (A) ground and (B) wall as a function of inclination angle for load locations: (a) 0.0, (b) 0.2, (c) 0.4, (d) 0.6, (e)).8, (f) 1.0. The weight and load are the same as in Figure 4; the coefficient of friction is 0.4.

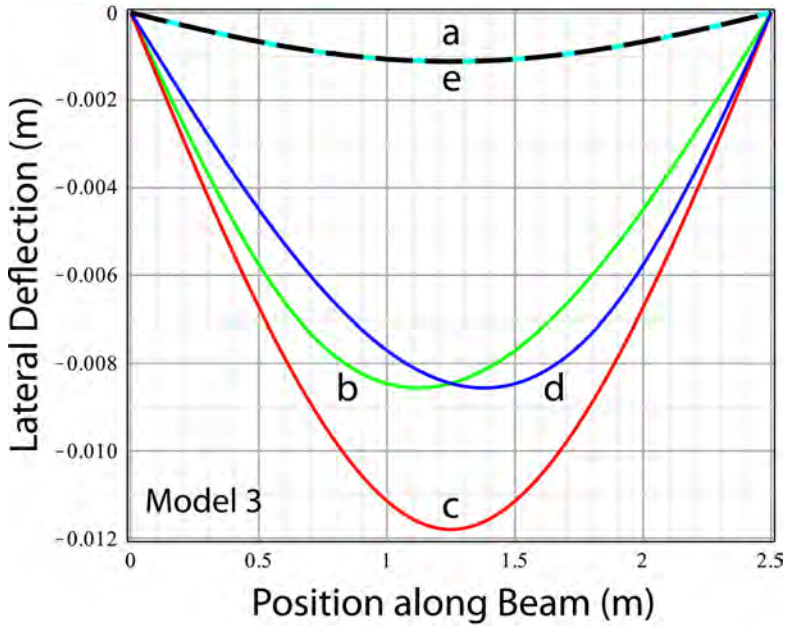

Figure 10. Deflection curves of the Model 3 single-beam ladder under the same conditions as for **Figure 5** for fractional lengths β along the beam of (a) 0 [ground point], (b) 1/4, (c) 1/2, (d) 3/4, (e) 1 [wall point] (note that plots (a) (solid line) and (e) (dashed line) overlap). The coefficient of friction is 0.4.

$$\delta_{\frac{1}{2}L}^{(b)} = \frac{L^3}{384EI_z}(5W + 8P)\cos\theta. \tag{40}$$

The deflection produced by the axial forces of Equation (36) is given by

$$\delta_{\beta L}^{(a)} = \frac{L}{AE}\left(A_2 - \left(\frac{1}{2}W + \beta P\right)\sin\theta\right)\left(\frac{1-\mu\tan\theta}{\tan\theta+\mu}\right). \tag{41}$$

For the load at mid-position and the other parameters of **Figure 10**, Equation (41) leads to an axial compression 13.3 μm. Thus, as was the case with Model 1, the bending deflection is again seen to be at least two orders of magnitude greater than the corresponding deformation due to axial compression.

3. Measured Reaction Forces on a Fixed Ladder

To determine which, if any, of the three basic models describes most closely the reaction forces on a fixed ladder, an experiment was performed to measure forces R_1, R_2, and R_3. The experiment was performed as follows. A ladder of length 244 cm and weight 18.9 lbs (84.07 N) was placed against a vertical wall at an angle of 68˚ to the ground. A two-axis force platform (Pasco Model PS-2142) was situated horizontally on the ground beneath each of the two rails of the ladder. The top of the ladder rested on a third force platform attached vertically to the wall. Each force platform, used in conjunction with a computer and the appropriate interface, was designed to measure the applied force normal to its surface (up to a maximum of 4400 N) and along an axis parallel to its surface (up to 1100 N).

The ladder comprised seven rungs located at fractional lengths along the rails of

$$\beta = \left(\frac{32}{244}, \frac{62}{244}, \frac{92}{244}, \frac{122}{244}, \frac{152}{244}, \frac{182}{244}, \frac{212}{244}\right) \approx (0.131, 0.254, 0.377, 0.500, 0.623, 0.746, 0.869)$$

of which the first six rungs were used in the experiment. External loads were applied to the rungs in the form of lead bricks, each brick weighing 25 lbs (111.21 N). Measurements of the normal and parallel forces were made for discrete loads of 1, 2, 3, or 4 bricks placed on each rung in progressive order from rung 1 to rung 6. The sum of the forces normal to the horizontal surface of force platforms 1 and 2 (supporting the rails) constituted reaction R_1. The sum of the forces parallel to the surface of platforms 1 and 2 constituted reaction R_2. The force normal to the vertical surface of force platform 3 (against which the top of the ladder rested) constituted reaction R_3. Although the initial intention was to measure reaction R_4 as well, this measurement could not be made because the force platforms did not measure shear forces accurately when the platform was oriented vertically[1]. The omitted reaction, however, was not needed to establish the conclusions drawn from this experiment.

Table 1 records the measurements of the 3 reactions (R_1, R_2, R_3) at each of 6 rungs for each of 4 loads (25, 50, 75, 100 lbs). The experimental forces are respectively compared with the corresponding theoretical predictions of the three models in Figures 11-13.

In order to apply the theoretical relations of Models 2 and 3, it is necessary to know the coefficient of friction μ of the ladder with the wall—or, more accurately, with the surface of the force platform attached to the wall. This coefficient cannot be calculated theoretically, but must be obtained empirically from the data. The method employed here was trial and inspection; *i.e.* to assume a value for μ, calculate and plot the resulting reactions, and adjust as necessary the value of μ until a satisfactory match with data was achieved, provided that the model itself is a valid representation of the underlying mechanical processes. The entire procedure can be executed in a matter of seconds with a fast computer and available mathematical software such as *Maple* or *Mathcad*. It is to be emphasized that the totality of the 72 measurements (3 reactions × 4 loads × 6 load locations) tightly constrained the value of μ. For Model 2 or 3 to be valid it is necessary that a *single* value of μ suffice to account for all the data. If different statistically significant values of μ for the various reactions are needed to match the data, or if no value of μ matches the data, then Model 2 or 3 would not describe the static equilibrium of a ladder against a wall.

[1]A force normal to the surface of the platform is measured by means of 4 beams connecting the 4 footpads of the device to strain gauges. A force parallel to the surface (oriented along an indicator arrow) is measured by a single strain gauge connected to the center of the upper surface. Small deviations from center in placement of the top of the ladder resulted in erratic values of the parallel force.

Table 1. Experimental Normal and Parallel Reactions on a Ladder.

$\theta = 68.0^{\circ}$	LOAD (lbs)	25	50	75	100
REACTIONS (N)	**RUNG**				
Ground Normal R_1					
	1	347.81	303.74	412.54	526.04
	2	188.54	302.98	413.19	526.67
	3	193.31	304.92	409.82	522.06
	4	189.95	303.37	413.52	520.52
	5	187.31	300.74	409.77	516.84
	6	188.50	298.47	403.50	508.11
Ground Parallel R_2					
	1	20.19	23.87	31.56	37.00
	2	22.92	35.01	47.29	58.86
	3	32.47	48.67	63.63	80.60
	4	37.15	60.90	86.58	106.12
	5	37.50	67.05	95.88	121.87
	6	47.62	81.22	113.40	145.17
Wall Normal R_3					
	1	10.01	14.09	17.70	21.40
	2	16.45	28.49	36.74	46.61
	3	24.14	39.44	53.67	69.85
	4	28.82	51.80	74.75	95.94
	5	32.76	60.15	87.46	112.59
	6	40.07	73.52	104.20	138.55

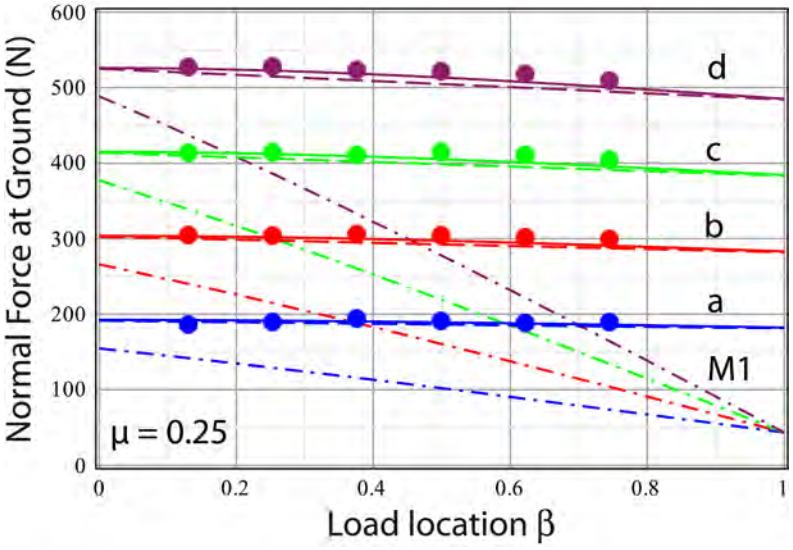

Figure 11. Experimental measurement (solid circles) of the normal reaction R_1 at the ground compared with predictions of Model 1 (dash-dot), Model 2 (solid), and Model 3 (dash) for loads (in lbs) of (a) 25 (blue), (b) 50 (red), (c) 75 (green), (d) 100 (burgundy). The set of Model 1 curves designated M1 do not match the data at all.

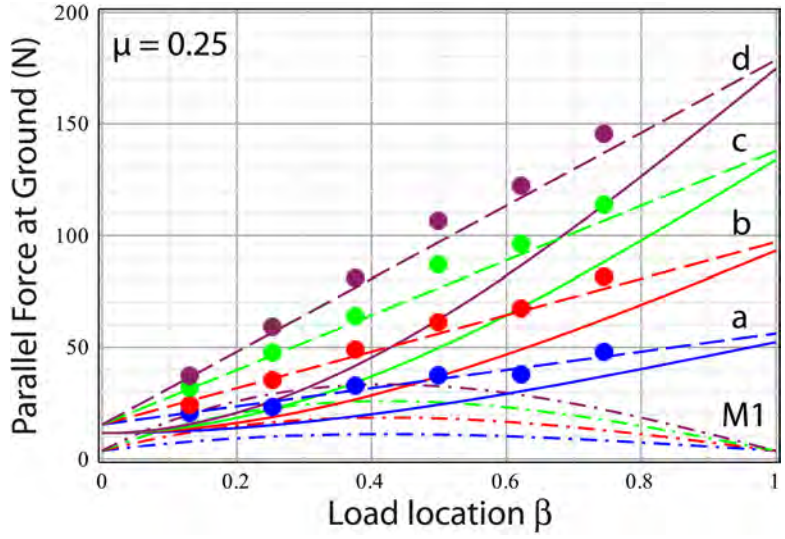

Figure 12. Experimental measurement of the parallel reaction R_2 at the ground compared with predictions of the three models. The symbolism in color and line style is the same as for Figure 11. Model 3 best matches the data.

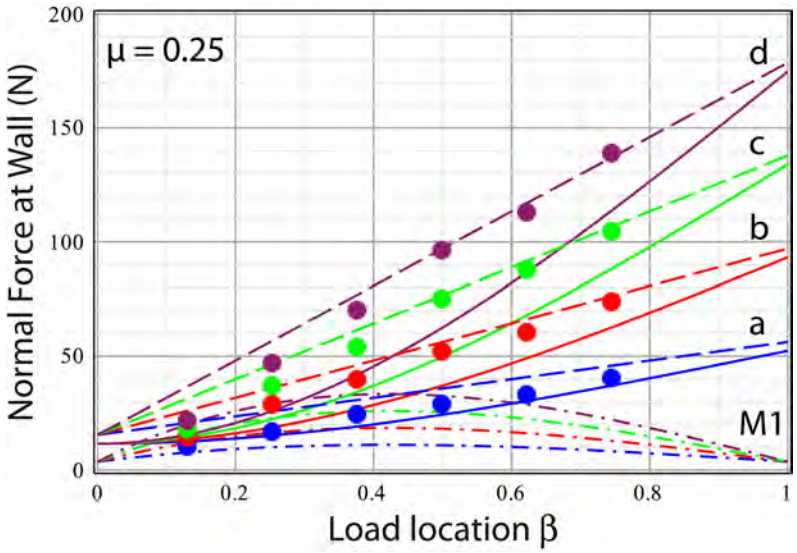

Figure 13. Experimental measurement of the normal reaction R_3 at the wall compared with predictions of the three models. The symbolism in color and line style is the same as for Figure 11. Model 3 best matches the data.

From examination of Figures 11-13 one can conclude the following:

- Model 1 does not account for any of the measured reactions.
- Models 2 and 3 account more or less equally well for the normal reaction R_1 at the ground support (Figure 11).
- Model 2 does not account for the measurements of the parallel reaction R_2 at the ground (Figure 12) or normal reaction R_3 at the wall (Figure 13).
- Model 3 accounts satisfactorily for all three reaction forces for $\mu \approx 0.25$ estimated from the data by trial and inspection.

To test the consistency of Model 3, the reaction parallel to the wall R_4 was

obtained from the data by the two independent relations

$$\begin{aligned} &(a)\ R_4 = \mu R_3 \\ &(b)\ R_1 + R_4 = W + P \end{aligned} \tag{42}$$

where relation (a) is one of the defining conditions of the model, and relation (b) is required by Newton's 2nd law applied to static equilibrium. Panel A of Figure 14 shows plots of R_4 for different loads and load locations obtained from relation (a) of Equation (42). Of the three models, Model 3 is again seen to account most closely for the patterns of measured points. Panel B of Figure 14 plots relation (b) of Equation (42) with R_4 given by independent relation (a). As expected, the expression $R_1 + R_4$ sums to a constant equal to $W + P$ for each of the four values of applied load P.

Interpretation of Results

From the foregoing comprehensive experimental test, one can conclude that, of the various mechanical conditions presumed to describe the static equilibrium of a ladder against a wall, those upon which Model 3 is based best represent the actual physical situation. It is useful to summarize explicitly the nature of these conditions.

- The elimination of Model 1 indicates that the length of the ladder is not constrained by axial forces at the ground or wall. Recall that it was this constraint that provided a complementary relation for resolving static indeterminateness in the axial direction. However, the reported experiment is consistent with no unrelieved axial strain. This means that the ladder, in response to its own weight and/or to the applied load, has relaxed to its (very slightly) compressed length in the course of reaching static equilibrium.

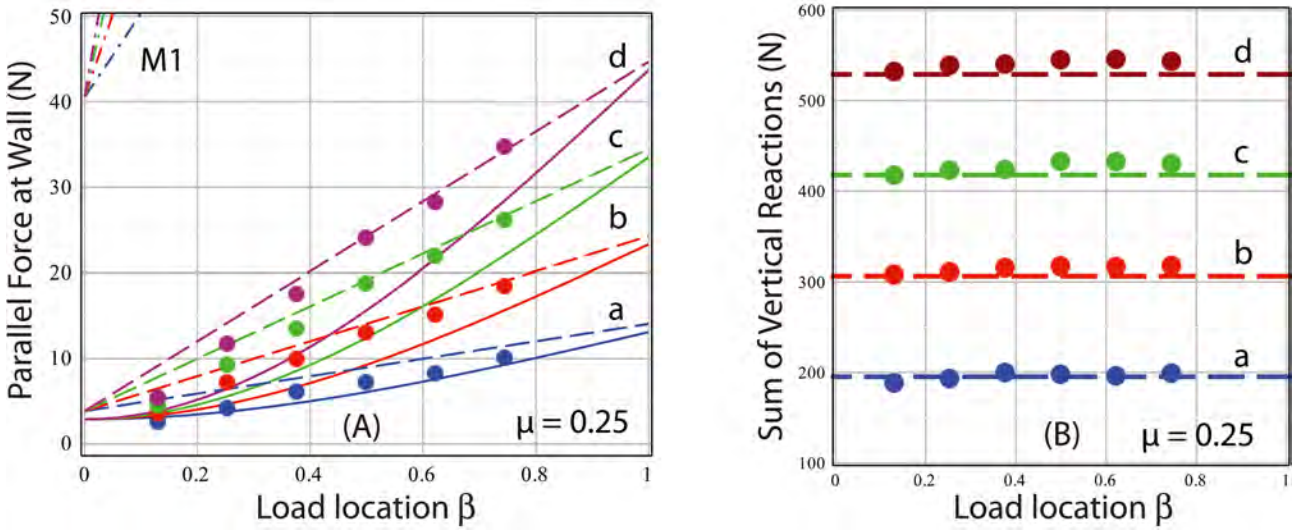

Figure 14. (A) Parallel reaction force at the wall R_4 (solid circles) deduced from the measurement of reaction R_3 normal to the wall and the experimental estimate of the coefficient of friction μ between the ladder and the wall. Line styles and colors of plots represent the same models and applied loads of Figure 11. M1 explicitly designates Model 1; (B) Test of the consistency of R_4 predicted by Model 3 (dashed line) for the applied loads P of Figure 11. For each load P (25, 50, 75, 100 lbs), the reactions $R_1 + \mu R_3$ should sum to a constant $W + P$, where W is the ladder weight.

- The elimination of Model 2 (and Model 1) likewise indicates that the bending of the ladder does not engender a torque at the ground support. Recall that it was this initially unknown moment that necessitated a complementary relation to resolve the static indeterminateness in the transverse direction. The reported experiment is consistent with no internal rotational moment at the base. This means that the ladder, initially presumed to be straight, has relaxed (very slightly) to the shape of an elastic deformation curve like those shown in **Figure 10** in the course of reaching static equilibrium.
- The satisfactory accord between Model 3 and the experimental results tends to confirm that, for a ladder stationary, but not clamped, at its base, it is the friction at the wall that provides the complementary relation needed to resolve static indeterminateness so that all four forces of reaction can be calculated. The theoretical expressions for the reactions do not depend on the elastic modulus of the ladder. They do depend, however, on the coefficient of friction of the ladder at the wall. The experimental results are consistent with an empirical relation whereby the friction at a surface is proportional to the normal force on that surface.

The theoretical models tested in this paper each embodied one or more distinct physical attributes conceivably responsible for the forces of reaction on a fixed ladder modeled by a single beam. In this regard, the models were never intended to provide an exact theory of the stresses and strains within an actual ladder. To achieve that would require a detailed mechanical model, outside the scope of this paper, taking account of the exact shape, weight distribution, and area moments of inertia of the components of the ladder, including rungs. This caveat must be borne in mind when comparing theory and experiment in **Figures 11-14**. The dashed lines signifying Model 3 in the figures do not pass through all the experimental points, although they are sufficiently close for the purposes of distinguishing among the models. Small adjustments in the value of the coefficient of friction μ could achieve better agreement in one reaction or another, but there is little reason to make such refinements. Nor is there any reason to attempt to obtain an optimum value of μ by a statistical fitting process such as the method of maximum likelihood, or least square's analysis, or by Bayes' theorem [18]. A nonlinear fit of that kind would be computationally intensive and, assuming it even converged, would yield values of μ not much better than the estimate obtained simply and quickly by trial and inspection.

The great practical utility of Model 3, now that it is validated by experiment, is that it provides a simple, but satisfactory, way to estimate the forces exerted by ladders on structures as a function of the climber's weight and position of ascent and the ladder's angle of inclination. Moreover, it is readily generalizable in special situations of practical interest that may arise in engineering design or matters of litigation, such as cases where the ground is flat but sloped, or the wall is flat but not vertical, or the ladder inclines against a railing, not a wall, and overhangs it.

4. Effects of Impact Loads

Although the primary focus of this paper has been on the static equilibrium of a ladder against a wall, the manner in which ladders are used in practice makes it necessary to discuss, albeit briefly, the question of impact loads. The experimental data of Table 1 were obtained by carefully and sequentially placing calibrated masses at designated rungs along the ladder so as to avoid imparting momentum to the ladder. Figure 15 shows the normal and parallel reactions (in arbitrary units) at the wall recorded as a function of time as a climber slowly ascends and then slowly descends the ladder, resting for a few seconds at each rung. The horizontal red bars mark the approximate values of the equilibrium reactions when the climber is stationary at each rung.

One sees, however, significant fluctuations about the equilibrium values as the climber transitions from one rung to the next. In particular, on the ascent, the reactions at the wall drop suddenly as the climber lifts his foot from a rung, and then rises suddenly as he places his foot on the next higher rung. On the descent, the reverse occurs for the normal reaction at the wall: the reaction increases dramatically as the climber raises his foot to step on the rung below.

The conveyance of momentum to a structure over a time interval is referred to as impact or impulse loading [19]. According to Newton's laws of motion, when the climber accelerates upward, the ladder must recoil downward, thereby exerting an additional force on whatever the ladder is leaning against. In physics, the integral of a force $F(t)$ over time t is designated impulse. An essential

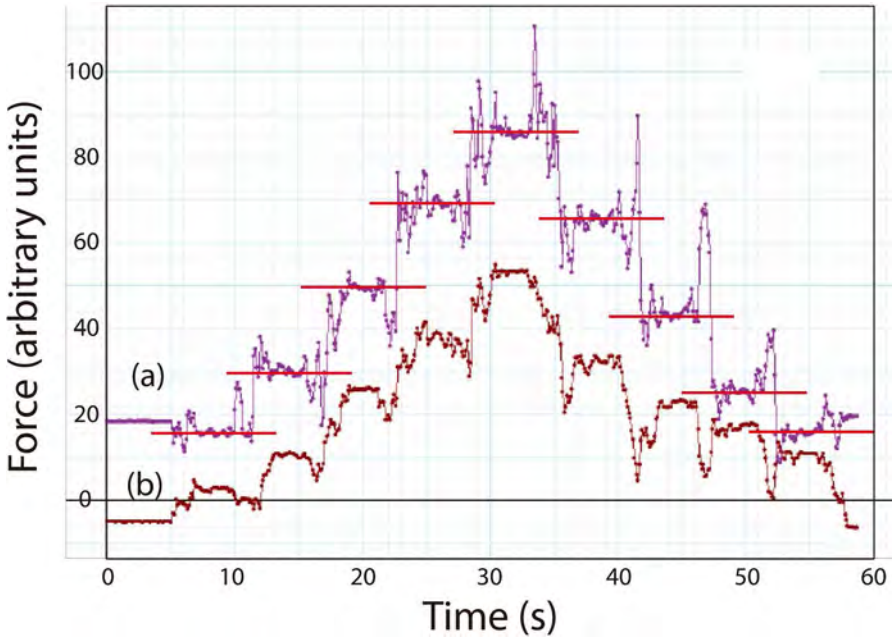

Figure 15. Normal (a) and parallel (b) forces at the wall as a function of time as a climber ascends, then descends, the first 5 rungs of a ladder. At each rung, the climber waits a few seconds until the condition of static equilibrium is achieved, as indicated by the horizontal red bars locating the mean equilibrium force (in arbitrary units) recorded at each rung.

matter in the safe use of a ladder is to determine how large a force the impulsive loading by a climber creates in comparison to the forces of static equilibrium.

One way to do this is to model the ladder as linear elastic structure governed by Hooke's law

$$P(t) = -ky(t) \tag{43}$$

in which k is the force constant and $y(t)$ is the deformation under the load $P(t)$. It is well known from the physics of oscillators [20] that the force constant k and the oscillation angular frequency ω are related by

$$k = M\omega^2 \tag{44}$$

where M is the mass of the object. Newton's second law, in the absence of dissipation of mechanical energy, then takes the form

$$\frac{\mathrm{d}^2 y}{\mathrm{d}t^2} + \omega^2 y = \frac{P(t)}{M} \tag{45}$$

for which the general solution, derivable by means of Green's functions [20], is

$$y(t) = \frac{1}{M\omega}\int_0^t \sin\omega(t-t')P(t')\mathrm{d}t' \tag{46}$$

with initial conditions

$$y(0) = \left.\frac{\mathrm{d}y}{\mathrm{d}t}\right|_{t=0} = 0. \tag{47}$$

The impulse load $P(t)$ can be modeled as a pulse of amplitude P_0 and width τ by the difference of two Heaviside functions

$$P(t) = P_0\left[H(t) - H(t-\tau)\right]. \tag{48}$$

Substitution of Equation (48) into (46) leads to the solution

$$y(t) = \frac{P_0}{M\omega^2}\left[\cos\omega(t-\tau) - \cos\omega t\right] \tag{49}$$

from which one obtains by standard calculus the maximum deflection

$$y_{\max} = \frac{P_0}{M\omega^2}\sqrt{2(1-\cos\omega\tau)} \tag{50}$$

and therefore from Equations (43), (44) and (50) the maximum force of impact

$$P_{\max} = \left|M\omega^2 y_{\max}\right|_{\omega\tau=\pi} = 2P_0. \tag{51}$$

P_0 is interpretable as the time-averaged load or, equivalently, the load at static equilibrium—*i.e.* the weight of the climber in the context of a ladder.

To the extent that the conditions of the pulse model realistically apply to a ladder, Equation (51) indicates that a climber can generate a maximum impact load that is twice his weight. **Figure 16** shows a plot of the normal reaction at the ground (*i.e.* normal to a horizontal force platform) as a climber *rapidly* ascends and descends a ladder—in contrast to the slow ascent and descent of **Figure 15** (note that the time base in **Figure 16** is 1/3 that of **Figure 15**). The blue horizontal bars mark the approximate reactions at static equilibrium at each rung. Of

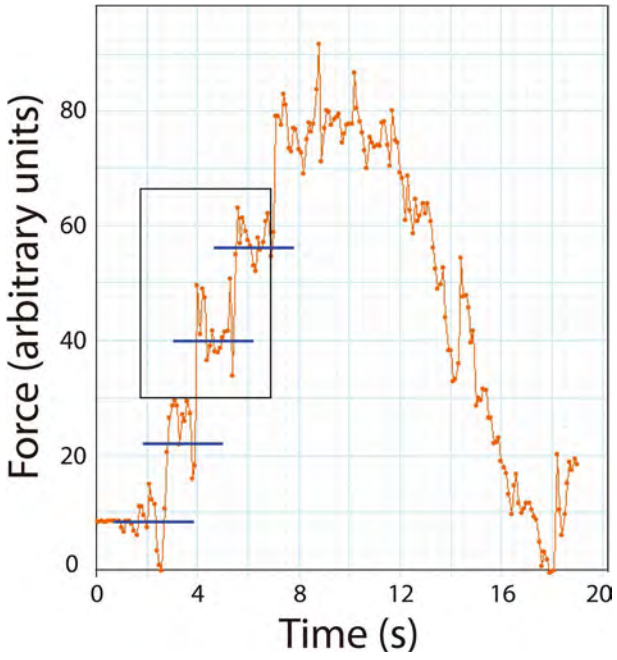

Figure 16. Normal force at the ground as a function of time as a climber ascends and descends rapidly. Horizontal blue bars locate the mean equilibrium force. Large fluctuations signify dynamic impact loads. The black rectangle encompasses the climber's transition from the third to fourth rung, thereby generating an impact load approximately one and half times his weight.

particular interest is the region within the black rectangle, which corresponds to the transition of the climber from rung 3 to rung 4 within a time interval Δt of about 0.2 s. Since the vertical separation between the rungs is $\Delta s = 30$ cm, the vertical acceleration a of the climber can be estimated from the kinematics of uniform acceleration [21] to be

$$a = \frac{2\Delta s}{(\Delta t)^2} \approx \frac{2 \times 0.3\,\mathrm{m}}{(0.2\,\mathrm{s})^2} = 15\,\mathrm{m \cdot s^{-2}} \tag{52}$$

or, relative to the acceleration of gravity $g = 9.81\,\mathrm{m \cdot s^{-2}}$,

$$\frac{a}{g} = \frac{P_{\mathrm{climber}}}{P_0} \approx \frac{15}{10} = 1.5\,. \tag{53}$$

Equation (53) is consistent with Equation (51) of the dynamical pulse model. Indeed, in a more comprehensive model, the dissipation of mechanical energy must be taken into account and would lead to a ratio $(P_{\max}/P_0) < 2$. Nevertheless, the import of Equation (51) is that the numerical difference between impact forces and forces at static equilibrium can be consequential for those who use ladders in their work or who are responsible for setting safety guidelines and regulations with respect to ladders.

5. Reaction Forces on a Single Wood Beam Inclined against a Wall

The single-beam models developed in Section 2 to describe the reaction forces

on a ladder inclined against a wall should, in principle, apply to an actual single beam inclined against a wall. The author is unaware of any previously reported experiment to measure these forces and determine which, if any, of the theoretical models best accounts for these forces. This section reports the results of such a test.

Measurements using one horizontal force platform at the base and one vertically mounted force platform at the top were made on a wood beam of mass 6.92 kg, length $L = 2.04$ m, width $w = 7.5$ cm, height $h = 8.5$ cm (symbols correspond to panel C of Figure 1) inclined against a wall at an angle of 57.7˚ to the ground. Starting at the center of the beam, round eyelets were screwed into the narrower side at intervals of 30 cm for a total of six eyelets. Loads were applied to the beam in units of 2 kg masses stacked on a 444 g weight hanger hooked to one of the eyelets. The eyelets, which served the equivalent function of rungs of the ladder, permitted load placements at fractional lengths of the beam

$$\begin{aligned}\beta &= \left(\frac{42}{204}, \frac{72}{204}, \frac{102}{204}, \frac{132}{204}, \frac{162}{204}, \frac{192}{204}\right) \\ &\approx (0.206, 0.353, 0.500, 0.647, 0.794)\end{aligned}$$

of which the first five eyelets were used in the experiment. Total loads (apart from the weight of the beam) ranged from about 4.4 N to 102.4 N.

Table 2 records the measurements of the four forces of reaction. With a single beam, in contrast to a ladder, it was possible to measure directly the parallel force at the wall because the beam contacted the center of the vertical force platform where the shear-sensitive strain gauge was located.

Figure 17 shows a comparison of the measured reactions with the predictions of the three theoretical models for four different loads. One sees again, as in the case of the ladder measurements, that Model 1 (dashdot line) does not fit any of the data. For a coefficient of friction at the wall $\mu = 0.35$, Models 2 and 3 give close predictions for the normal force at the ground (blue circles and curves) and the parallel force at the wall (maroon circles and curves), although the curve due to Model 3 (dashed line) passes through the data points (solid circles) and the curve due to Model 2 (solid line) does not. However, the parallel force at the ground (red circles and curves) and the normal force at the wall (green circles and curves) suffice to eliminate Model 2. The linear curve due to Model 3 (dashed line) very closely matches the measured points, whereas the curve due to Model 2 (solid line) has a marked curvature and passes well below the red solid circles. Only Model 3 accounts satisfactorily for all the data for a single value of the coefficient of friction.

This experiment lends strong support to the conclusion that the reaction forces on a single beam are described by the same theoretical model that describes the reaction forces on a fixed ladder, and that, as long as the base of either does not slip, the complementary relation needed to resolve the static indeterminateness of the problem is the force of friction at the wall.

Table 2. Experimental normal and parallel reactions on a single wood beam.

$\theta = 57.7^{\circ}$	LOAD (N)	43.55	63.15	82.75	102.35
REACTIONS (N)	EYELET				
Ground Normal R_1					
	1	100.3	118.8	137.7	156.6
	2	99.6	118.6	137.3	154.6
	3	100.0	119.2	134.1	150.9
	4	98.0	115.8	131.8	149.0
	5	99.0	113.8	131.9	148.3
Ground Parallel R_2					
	1	21.8	23.1	15.9	29.5
	2	25.8	31.0	35.3	38.5
	3	31.9	36.8	46.9	49.4
	4	34.6	40.4	45.6	53.1
	5	36.2	44.3	53.6	62.6
Wall Normal R_3					
	1	22.7	25.0	28.2	31.1
	2	27.5	32.8	38.0	42.1
	3	33.3	40.1	45.7	51.5
	4	36.7	45.8	53.5	62.2
	5	42.4	44.3	63.0	73.0
Wall Parallel R_4					
	1	9.0	9.7	10.6	10.9
	2	9.2	10.3	10.7	13.0
	3	9.1	9.7	13.5	16.2
	4	10.7	12.8	16.1	18.4
	5	10.4	14.3	15.9	18.7

6. Conclusions

The question of how to calculate the four forces of reaction on a ladder in static equilibrium against a wall has been an unresolved issue for many years. The core of the difficulty is that the problem is statically indeterminate and requires complementary relations beyond the equations of static equilibrium. Three fundamental types of models, differing in the assumptions with regard to supports at the ground and wall, were examined. The comprehensive theoretical analysis and experimental measurements of this paper showed unambiguously that the forces of reaction were best accounted for by the model employing a single complementary relation characterizing friction at the wall.

The force law for friction that resolved the static indeterminateness in the third model is a single-parameter empirical relation. This parameter, the coefficient

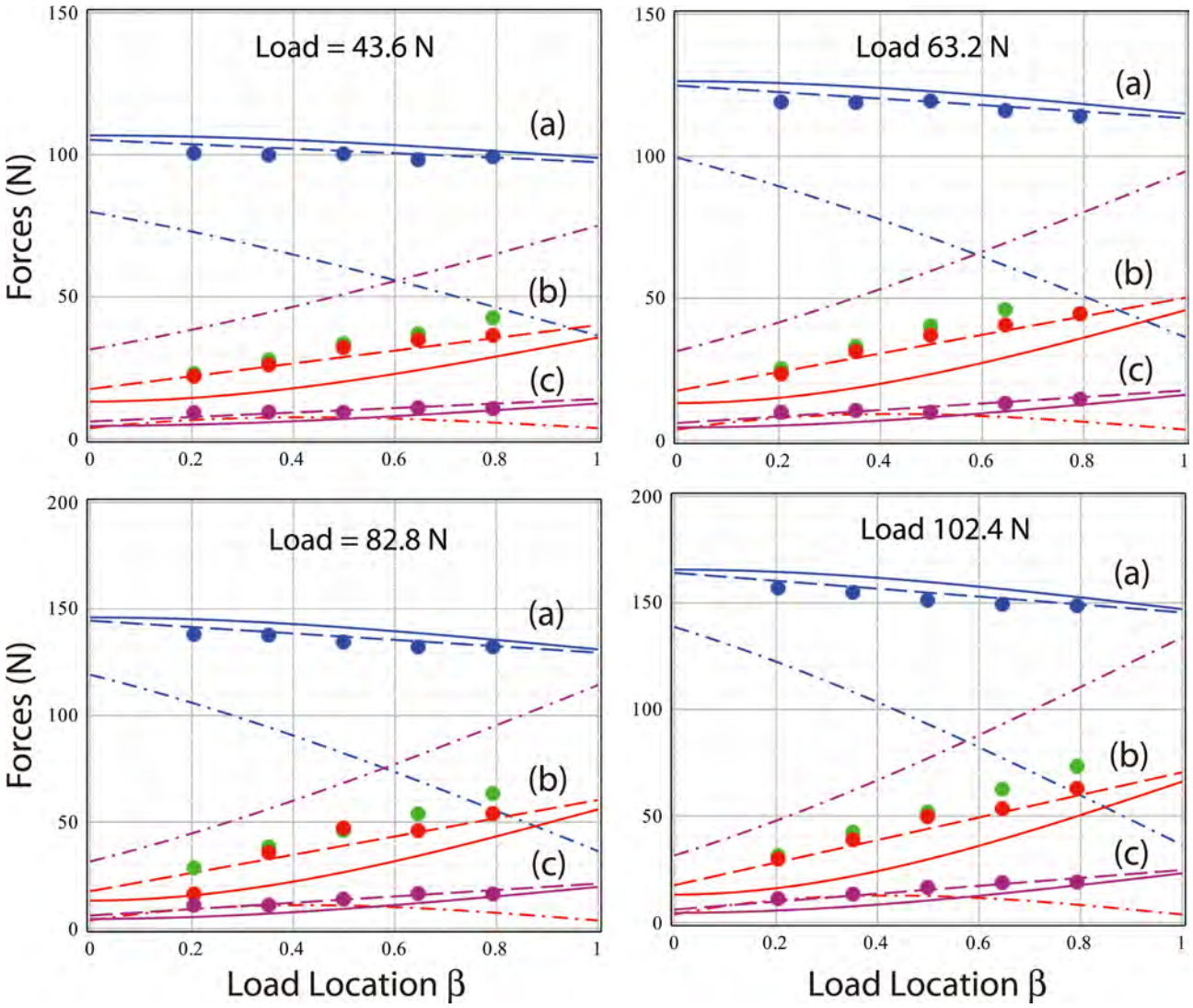

Figure 17. Reaction forces on a single wood beam for four different loads as a function of load location for an inclination angle of 57.7˚: (a) normal force at ground (blue), (b) parallel force at ground (red), (c) parallel force at wall (maroon). Measured points (solid circles) are superposed by predictions of Model 1 (dotdash), Model 2 (solid), Model 3 (dash). The green solid circles are experimental values of the normal force at the wall for which the theoretical curves are identical to those of (b). Parameters are beam weight 67.8 N, beam length 204 cm, and empirically found coefficient of friction 0.35.

of friction μ, was estimated from, and tightly constrained by, the experimental data. A critical test of the third model was, in fact, to show that a single value of this coefficient sufficed to yield the normal and parallel reactions at the ground and at the wall for all values and locations of the loads.

As part of the analyses reported here, the axial and transverse deformations of the single-beam ladder were calculated by means of Castigliano's theorem, and then confirmed by a full calculation of the deflection curve (elastica) of the beam. The analyses demonstrated that the deformation due to flexure is about two to three orders of magnitude larger than the deformation due to compression. Thus, any model that takes into account only axial compression, but neglects flexure, to resolve the static indeterminateness of reactions on an inclined beam is likely

to be inaccurate.

Measurements were also made of the impact loading on a ladder by the ascent and descent of a climber. In a typical ascent without hesitation, the impact loading was found to be about $1\frac{1}{2}$ times the climber's weight. This result is consistent with the predicted maximum value of 2 for the ratio of impact load to static load by a dynamic model of the ladder as a linear elastic medium subject to a pulse perturbation.

The successful description of the reaction forces on a ladder modeled as a single beam prompted the question of whether any of the three theoretical models satisfactorily accounted for the reaction forces on an actual single beam. Measurements analogous to those made on the ladder were also made on a wood beam of comparable length. The results showed that the same model that accounted for the reaction forces on the ladder also best predicted the reaction forces on the single wood beam. Whether this result is completely general, or whether a different outcome might arise for a beam of different composition, length, and/or cross section can only be determined by further experimentation.

A final point of importance concerns the inclusiveness of the three fundamental models. In other words, is there another independent way to analyze an Euler-Bernoulli (E-B) beam ladder that might produce better agreement with experiment than Model 3 of this paper? In the author's opinion, the answer is probably "no". The reason is that other models within the single E-B beam framework are either irrelevant, equivalent, or inconsistent.

For example, two models not analyzed in this paper include a ladder with simple (*i.e.* frictionless) support at the wall and a ladder with fixed support (*i.e.* infinite friction) at the wall. Neither model is relevant because the contact at the wall is neither frictionless nor immovable. (The models of this paper all assume non-slippage at the ground, for otherwise there would be no static equilibrium.)

Consider, however, a variation of Model 1. Model 1 resolved static indeterminateness by applying two boundary conditions to the wall support in the configuration of Panel B of **Figure 1**: no displacement axially (in the direction of force A_2) or transversely (in the direction of force B_2). Although this model was in marked disagreement with the experiment, a question might be raised as to whether the outcome could be different if the boundary conditions were applied to the wall support in the configuration of Panel A of **Figure 1**, which shows the usual orientation of a ladder. The modified boundary conditions would then be: no displacement vertically (in the direction of force R_4) or horizontally (in the direction of force R_3). To implement these boundary conditions, one would express the strain energy U in terms of R_3 and R_4 (by transforming A_2 and B_2), then set to zero the derivatives of U with respect to R_3 and R_4. This procedure, however, leads to exactly the same reactions as obtained in the original Model 1.

Another conceivable model might be to express U in terms of R_3 and R_4 but impose only *one* boundary condition at the wall, e.g. no displacement verti-

cally. The resulting equation, which couples the vertical and horizontal reactions at the wall, is then used together with Equation (31) which expresses zero torque in static equilibrium. This procedure is inconsistent, however, because the first equation leads to a rotational moment at the ground support, whereas the second equation describes the absence of such a moment. The resulting set of reactions depends on the length (L) and width (h) of the beam (in conflict with experimental results) and leads to large reaction forces that violate physical laws.

In conclusion, for any model of a ladder (or other physical structure) it is paramount that the equations of static equilibrium and the complementary relations be consistent and compatible with the boundary conditions.

Acknowledgements

E. Donovan, W. Emery, J. Hallquist, W. Scully, L. Sewanan, and W. Strange each helped take data at some point during the initial phase of this project. The author also thanks Trinity College for partial support through the research fund associated with the George A. Jarvis Chair of Physics.

Conflicts of Interest

The author declares no conflicts of interest regarding the publication of this paper.

References

[1] Ladders 101. https://www.americanladderinstitute.org/page/Ladders101

[2] Silverman, M.P. (2009) Final Report: Force of a Ladder on a Railing under Static and Dynamic Conditions. Case of Shattuck v. Wynfield, Hartford Superior Court, Hartford, CT.

[3] Knight, R.D. (2017) Physics for Scientists and Engineers: A Strategic Approach. 4th Edition, Pearson Education Inc., Boston, MA, 113.

[4] Mendelson, K.S. (1994) Statics of a Ladder Leaning against a Rough Wall. *American Journal of Physics*, **63**, 148-150. https://doi.org/10.1119/1.17972

[5] Gonzalez, A.G. and Gratton, J. (1996) Reaction Forces on a Ladder Leaning against a Rough Wall. *American Journal of Physics*, **64**, 1001-1005. https://doi.org/10.1119/1.18317

[6] Hakkinen, K.K., Pesonen, J. and Rajamaki, E. (1988) Experiments on Safety in the Use of Portable Ladders. *Journal of Occupational Accidents*, **10**, 1-19. https://doi.org/10.1016/0376-6349(88)90002-8

[7] Lee, Y.H. and Tung, E.K. (1992) Body and Ladder Mechanical Stresses Analysis in a Climbing Strike. In: Kumar, S., Ed., *Advances in Industrial Ergonomics and Safety IV*, Taylor and French, Montreal, 1007-1014.

[8] Chang, W.-R., Chang, C.-C., Matz, S. and Son, D.H. (2004) Friction Requirements for Different Climbing Conditions in Straight Ladder Ascending. *Safety Science*, **42**, 791-805. https://doi.org/10.1016/j.ssci.2004.02.002

[9] Silverman, M.P. and Farrah, J. (2018) Bending of a Tapered Rod: Modern Application and Experimental Test of Elastica Theory. *World Journal of Mechanics*, **8**, 272-300. https://doi.org/10.4236/wjm.2018.87022

[10] Hibbeler, R.C. (1997) Mechanics of Materials. 3rd Edition, Prentice Hall, Upper Saddle River, NJ, 582-583.

[11] Fowles, G.R. and Cassiday, G.L. (1993) Analytical Mechanics. 5th Edition, Harcourt Brace, New York, 54-55.

[12] Elastic Modulus of Aluminum. https://www.engineeringtoolbox.com/young-modulus-d_417.html

[13] Material Property Data. http://www.matweb.com/Search/MaterialGroupSearch.aspx?GroupID=316

[14] Elastic Modulus of Wood. https://www.engineersedge.com/lumber.htm

[15] Budynas, R.G. (1977) Advanced Strength and Applied Stress Analysis. McGraw-Hill, New York, 240-247.

[16] Matthews, J. and Walker, R.L. (1973) Mathematical Methods of Physics. W.A. Benjamin, Menlo Park, 107-109.

[17] Levien, R. (2008) The Elastica: A Mathematical History. Technical Report No. UCB/EECS 2008-103, Electrical Engineering and Computer Sciences University of California, Berkeley. http://www.eecs.berkeley.edu/Pubs/TechRpts/2008/EECS-2008-103.html

[18] Silverman, M.P. (2014) A Certain Uncertainty: Nature's Random Ways. Cambridge University Press, Cambridge, 45-83. https://doi.org/10.1017/CBO9781139507370

[19] Paz, M. (1985) Structural Dynamics: Theory & Computation. Van Nostrand Reinhold Co., New York, 63-65.

[20] Marion, J.B. and Thornton, S.T. (1988) Classical Dynamics of Particles and Systems. 3rd Edition, Harcourt Brace Jovanovich, New York, 98-135.

[21] Symon, K.R. (1971) Mechanics. 3rd Edition, Addison-Wesley, Reading, 11-13.

Appendix: Integration of the Heaviside Function

The Heaviside function defined in Equation (12) and repeated below

$$H\left(x-x_0\right)=\begin{cases}0 & x<x_0\\ 1 & x\geq x_0\end{cases} \tag{54}$$

provides an economic way to represent piecewise continuous functions, such as frequently occur in the mechanics of continuous media. In the representation of static forces, impact forces, rotational moments, and strain energy densities it is often necessary to integrate over expressions of the form $z^nH\left(z-a\right)$ where a is a non-negative constant and n is a non-negative integer. The general result is

$$\int_0^x z^nH\left(z-a\right)\mathrm{d}z=\left(\frac{x^{n+1}-a^{n+1}}{n+1}\right)H\left(x-a\right)\quad\left(n=0,1,2,\cdots\right). \tag{55}$$

A general proof, which will not be given here, can be constructed inductively from the examples below for $n=0,1$.

1) Case $n=0$:

$$\int_0^x H\left(z-a\right)\mathrm{d}z=\int_0^x H\left(z-a\right)\mathrm{d}\left(z-a\right)=\int_{-a}^{x-a}H\left(u\right)\mathrm{d}u=\left(x-a\right)H\left(x-a\right) \tag{56}$$

Steps: Transform the integration variable from z to $u=z-a$ and use the properties of $H\left(u\right)$ in Equation (54).

2) Case $n=1$:

$$\begin{aligned}\int_0^x zH\left(z-a\right)\mathrm{d}z&=\int_0^x\left(z-a\right)H\left(z-a\right)d\left(z-a\right)+a\int_0^x H\left(z-a\right)d\left(z-a\right)\\&=\int_{-a}^{x-a}uH\left(u\right)\mathrm{d}u+a\int_{-a}^{x-a}H\left(u\right)\mathrm{d}u\\&=\frac{\left(x-a\right)^2}{2}H\left(x-a\right)+a\left[\left(x-a\right)H\left(x-a\right)\right]\\&=\frac{x^2-a^2}{2}H\left(x-a\right)\end{aligned} \tag{57}$$

Steps:

- Line 1: Transform the integrand into a function of $u=z-a$ by appropriate subtraction and addition of terms.
- Line 2: Perform the first integral and import the result obtained in the case $n=0$ for the second integral.
- Lines 3 and 4: Expand and simplify the algebraic expressions to obtain the form of Equation (55).

World Journal of Mechanics, 2018, 8, 343-352
http://www.scirp.org/journal/wjm
ISSN Online: 2160-0503
ISSN Print: 2160-049X

Diagrammatic Approach for Investigating Two Dimensional Elastic Collisions in Momentum Space I: Newtonian Mechanics

Akihiro Ogura

Laboratory of Physics, Nihon University, Matsudo, Japan
Email: ogura.akihiro@nihon-u.ac.jp

How to cite this paper: Ogura, A. (2018) Diagrammatic Approach for Investigating Two Dimensional Elastic Collisions in Momentum Space I: Newtonian Mechanics. *World Journal of Mechanics*, **8**, 343-352.
https://doi.org/10.4236/wjm.2018.89025

Received: August 2, 2018
Accepted: August 28, 2018
Published: August 31, 2018

Abstract

We present the usefulness of the diagrammatic approach for analyzing two dimensional elastic collision in momentum space. In the mechanics course, we have two major purposes of studying the collision problems. One is that we have to obtain velocities of the two particles after the collision from initial velocities by using conservation laws of momentum and energy. The other is that we have to study two ways of looking collisions, *i.e.* laboratory system and center-of-mass system. For those two major purposes, we propose the diagrammatic technique. We draw two circles. One is for the center-of-mass system and the other is for the laboratory system. Drawing these two circles accomplish two major purposes. This diagrammatic technique can help us understand the collision problems quantitatively and qualitatively.

Keywords

Two Dimensional Elastic Collision, Momentum Space, Laboratory System, Center-of-Mass System, Newtonian Mechanics

1. Introduction

Collisions are of importance in physics. Especially for small world such as atoms or nuclei, scattering is the crucial technique to investigate their nature. Before studying the scattering theory of quantum mechanics, we had better to get familiar with collisions in classical mechanics.

We have two main themes for studying the collision problems [1] [2]. One is that we have to obtain velocities of the two particles after the collision from initial velocities by using conservation laws of momentum and energy. Since we have three equations from conservation law and four unknowns, one parameter

out of four should be fixed according to the given collision problems. The other is that we have to study two ways of looking collisions, *i.e.* laboratory system and center-of-mass system. We need to convert between the two systems.

In order to achieve those two themes, the diagrammatic technique gives the powerful tool. For the collisions in one dimension, the mass-momentum diagram with mass m along the vertical axis and momentum p represented on the horizontal axis is the useful technique [3]. We obtain the whole story of the collision in one dimension from the single (m, p)-diagram.

When we apply the mass-momentum diagram to the elastic collisions in two dimensions, three dimensional space (m, p_x, p_y) is needed. However, in this case, the projection onto the (p_x, p_y)-plane is sufficient [4]. For Newtonian mechanics [5], we draw a circle in the two dimensional momentum space and also draw arrows of the momentum of the colliding particles into the circle. This is a way of looking collisions from laboratory system. In this article, we add one more circle. This is from the point of view of the center-of-mass system. These two circles give all information for two dimensional elastic collision problems.

This paper is organized in the following way. In Section 2, we recall two dimensional elastic collisions with equations. In Section 3, we show the diagrammatic approach for two dimensional elastic collision in order. First, we draw a circle for the center-of-mass system. Then we add to draw one more circle to obtain the momentum after the collision in the laboratory system. In Section 4, we investigate the special case where the target particle is at rest before the collision. Section 5 is devoted to a conclusion.

2. Elastic Collision between Two Particles in Two Dimensions

Let us recall the treatise of the two dimensional elastic collision with equations for later use. Figure 1 shows the collisions from the point of view in laboratory and center-of-mass systems and also show the notation which we use in this article. The projectile A has mass m_A and velocity $\boldsymbol{v}_A$ and the target B has mass m_B and velocity $\boldsymbol{v}_B$ before the collision. The momenta are given by $\boldsymbol{p}_A = m_A\boldsymbol{v}_A$ and $\boldsymbol{p}_B = m_B\boldsymbol{v}_B$. They are known parameters or initial conditions of the collision. Usually, the velocities $\boldsymbol{v}_A$ and $\boldsymbol{v}_B$ are supposed to be in the

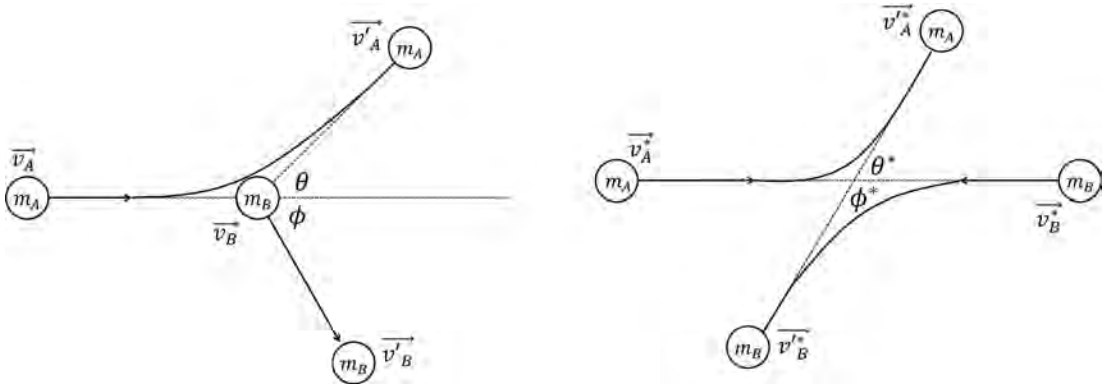

Figure 1. Left: Collisions in the laboratory system. Right:Collisions in the center-of-mass system.

same direction and are set along the *x*-axis in this article. The velocities after the collision are distinguished by the primes. And the asterisk is attached to the parameters in the center-of-mass system.

We have to obtain the four parameters $\left(v_A', v_B', \theta, \phi\right)$ after the collision in the laboratory system. However, we have only three equations, *i.e.* energy conservation and two components of momentum conservations. So, we have to fix one parameter out of four. We investigate the collision in the following way.

2.1. Velocities of the Center-of-Mass

We write down the conservation of momentum for two systems:

$$m_A \boldsymbol{v}_A + m_B \boldsymbol{v}_B = m_A \boldsymbol{v}_A' + m_B \boldsymbol{v}_B' \quad \text{for laboratory system,} \tag{1}$$

$$m_A \boldsymbol{v}_A^* + m_B \boldsymbol{v}_B^* = m_A \boldsymbol{v}_A'^* + m_B \boldsymbol{v}_B'^* = \boldsymbol{0} \quad \text{for center-of-mass system.} \tag{2}$$

Let $\boldsymbol{V}$ be the velocity of the center-of-mass. The relations between $\boldsymbol{V}$ and the velocities of the particles in two systems are as follows:

$$\boldsymbol{v}_A^* = \boldsymbol{v}_A - \boldsymbol{V}, \quad \boldsymbol{v}_B^* = \boldsymbol{v}_B - \boldsymbol{V}. \tag{3}$$

Substituting Equation (3) into Equation (2), we obtain

$$\boldsymbol{V} = \frac{m_A \boldsymbol{v}_A + m_B \boldsymbol{v}_B}{m_A + m_B} = \frac{\boldsymbol{p}_A + \boldsymbol{p}_B}{m_A + m_B}, \tag{4}$$

which remains the same before and after collision.

2.2. Velocities and Momenta before Collision in Center-of-Mass System

Substituting Equation (4) into Equation (3), we obtain the velocities in the center-of-mass system

$$\boldsymbol{v}_A^* = +\frac{m_B}{m_A + m_B}\left(\boldsymbol{v}_A - \boldsymbol{v}_B\right), \quad \boldsymbol{v}_B^* = -\frac{m_A}{m_A + m_B}\left(\boldsymbol{v}_A - \boldsymbol{v}_B\right), \tag{5}$$

and the momenta

$$\boldsymbol{p}_A^* = +\frac{m_A m_B}{m_A + m_B}\left(\boldsymbol{v}_A - \boldsymbol{v}_B\right), \quad \boldsymbol{p}_B^* = -\frac{m_A m_B}{m_A + m_B}\left(\boldsymbol{v}_A - \boldsymbol{v}_B\right). \tag{6}$$

We clearly see that these expressions of the momentum satisfy the relation in Equation (2). Note that $\frac{m_A m_B}{m_A + m_B}$ is a reduced mass and $\boldsymbol{v}_A - \boldsymbol{v}_B$ $\left(v_A > v_B\right)$ is a relative velocity before the collision.

2.3. Velocities and Momenta after Collision in Center-of-Mass System

We write energy conservations for two systems:

$$\frac{m_A}{2}\left(\boldsymbol{v}_A\right)^2 + \frac{m_B}{2}\left(\boldsymbol{v}_B\right)^2 = \frac{m_A}{2}\left(\boldsymbol{v}_A'\right)^2 + \frac{m_B}{2}\left(\boldsymbol{v}_B'\right)^2 \quad \text{for laboratory system,} \tag{7}$$

$$\frac{m_A}{2}\left(\boldsymbol{v}_A^*\right)^2 + \frac{m_B}{2}\left(\boldsymbol{v}_B^*\right)^2 = \frac{m_A}{2}\left(\boldsymbol{v}_A'^*\right)^2 + \frac{m_B}{2}\left(\boldsymbol{v}_B'^*\right)^2 \quad \text{for center-of-mass system.} \tag{8}$$

From the conservations of momentum in Equation (2), we obtain the following relations:

$$\boldsymbol{v}_B^* = -\frac{m_A}{m_B}\boldsymbol{v}_A^*, \quad \boldsymbol{v}_B'^* = -\frac{m_A}{m_B}\boldsymbol{v}_A'^*. \tag{9}$$

Substituting these relations into Equation (8), we obtain

$$v_A'^* = v_A^*, \quad v_B'^* = v_B^*. \tag{10}$$

This means that the velocities (and also momenta) of the two particles stay in magnitude before and after the collision in the center-of-mass system. Thus the collision simply rotates the velocities. However, the angle of the rotation cannot be determined from the conservations of momentum and energy because we have four unknowns and only three equations: the energy and the two components of momentum conservations. Namely, there is an infinite number of possible final states of outgoing particles in an elastic collision in two dimensions. Let $\boldsymbol{n}^*$ be a unit vector in the direction of the velocity $\boldsymbol{v}_A'^*$ of the projectile A after the collision in the center-of-mass system. The scattering angle θ^* of the right figure in **Figure 1** is related by $\boldsymbol{n}^* = \left(\cos\theta^*, \sin\theta^*\right)$. Accordingly, the velocities after the collision in the center-of-mass system are written by

$$\boldsymbol{v}_A'^* = +\frac{m_B}{m_A + m_B}\left|\boldsymbol{v}_A - \boldsymbol{v}_B\right|\boldsymbol{n}^*, \quad \boldsymbol{v}_B'^* = -\frac{m_A}{m_A + m_B}\left|\boldsymbol{v}_A - \boldsymbol{v}_B\right|\boldsymbol{n}^*, \tag{11}$$

and the momenta are given by

$$\boldsymbol{p}_A'^* = +\frac{m_A m_B}{m_A + m_B}\left|\boldsymbol{v}_A - \boldsymbol{v}_B\right|\boldsymbol{n}^*, \quad \boldsymbol{p}_B'^* = -\frac{m_A m_B}{m_A + m_B}\left|\boldsymbol{v}_A - \boldsymbol{v}_B\right|\boldsymbol{n}^*. \tag{12}$$

Again, these expressions of the momentum satisfy the relation in Equation (2).

2.4. Velocities and Momenta after Collision in Laboratory System

In order to return to the laboratory system, we must add Equation (11) to the velocity of the center-of-mass $\boldsymbol{V}$ in Equation (4). We obtain velocities after the collision in the laboratory system,

$$\boldsymbol{v}_A' = \boldsymbol{v}_A'^* + \boldsymbol{V}, \quad \boldsymbol{v}_B' = \boldsymbol{v}_B'^* + \boldsymbol{V}, \tag{13}$$

and momenta

$$\boldsymbol{p}_A' = \boldsymbol{p}_A'^* + m_A\boldsymbol{V} = +\frac{m_A m_B}{m_A + m_B}\left|\boldsymbol{v}_A - \boldsymbol{v}_B\right|\boldsymbol{n}^* + \frac{m_A}{m_A + m_B}\left(\boldsymbol{p}_A + \boldsymbol{p}_B\right), \tag{14}$$

$$\boldsymbol{p}_B' = \boldsymbol{p}_B'^* + m_B\boldsymbol{V} = -\frac{m_A m_B}{m_A + m_B}\left|\boldsymbol{v}_A - \boldsymbol{v}_B\right|\boldsymbol{n}^* + \frac{m_B}{m_A + m_B}\left(\boldsymbol{p}_A + \boldsymbol{p}_B\right). \tag{15}$$

Note that the sum of both sides clearly shows the momentum conservation $\boldsymbol{p}_A' + \boldsymbol{p}_B' = \boldsymbol{p}_A + \boldsymbol{p}_B$ of Equation (1) in the laboratory system.

Let $\boldsymbol{p}_A' = \left(p_{Ax}', p_{Ay}'\right)$ be the x, y-components of the momentum of the projectile A in Equation (14). We write down explicitly as follows:

$$p'_{Ax} = \frac{m_A m_B}{m_A + m_B}\left|\boldsymbol{v}_A - \boldsymbol{v}_B\right|\cos\theta^* + m_A V, \tag{16}$$

$$p'_{Ay} = \frac{m_A m_B}{m_A + m_B}\left|\boldsymbol{v}_A - \boldsymbol{v}_B\right|\sin\theta^*, \tag{17}$$

where we note that the velocity $\boldsymbol{V}$ has the x-component only due to Equation (4). From these equations and the relation $\cos^2\theta^* + \sin^2\theta^* = 1$, we obtain

$$\left(\frac{p'_{Ax} - m_A V}{\frac{m_A m_B}{m_A + m_B}\left|\boldsymbol{v}_A - \boldsymbol{v}_B\right|}\right)^2 + \left(\frac{p'_{Ay}}{\frac{m_A m_B}{m_A + m_B}\left|\boldsymbol{v}_A - \boldsymbol{v}_B\right|}\right)^2 = 1. \tag{18}$$

This indicates the circle in momentum space, centered at $(m_A V, 0)$ with its radius $p_A^* = p_B^* = \frac{m_A m_B}{m_A + m_B}\left|\boldsymbol{v}_A - \boldsymbol{v}_B\right|$. These quantities are uniquely determined by the initial condition of the collision.

Let us consider the case where the target particle is at rest before the collision. Setting $\boldsymbol{v}_B = \boldsymbol{0}$ in Equation (18), we obtain

$$\left(\frac{p'_{Ax} - \frac{m_A}{m_A + m_B}p_A}{\frac{m_B}{m_A + m_B}p_A}\right)^2 + \left(\frac{p'_{Ay}}{\frac{m_B}{m_A + m_B}p_A}\right)^2 = 1. \tag{19}$$

Moreover, the case of which two particles have equal mass $m_A = m_B$ becomes more simple:

$$\left(\frac{p'_{Ax} - \frac{p_A}{2}}{\frac{p_A}{2}}\right)^2 + \left(\frac{p'_{Ay}}{\frac{p_A}{2}}\right)^2 = 1. \tag{20}$$

These equations of a circle will appear in the next sections.

3. Diagrammatic Technique

In this section, we deduce all relations, which we recalled in the former section, from the diagram in two dimensional momentum space.

3.1. Center-of-Mass System

Firstly, we draw a circle whose radius is $p_A^* = p_B^*$ in Equation (6), as depicted in Figure 2. This dashed circle centered at O describes the collision in the center-of-mass system. We draw dashed arrows of the momenta before the collision from Equation (6)

$$\boldsymbol{OA} = \boldsymbol{p}_A^* = +\frac{m_A m_B}{m_A + m_B}\left(\boldsymbol{v}_A - \boldsymbol{v}_B\right), \quad \boldsymbol{OB} = \boldsymbol{p}_B^* = -\boldsymbol{p}_A^*, \tag{21}$$

and after the collision from Equation (12)

$$\boldsymbol{OC} = \boldsymbol{p}_A'^* = +\frac{m_A m_B}{m_A + m_B}\left|\boldsymbol{v}_A - \boldsymbol{v}_B\right|\boldsymbol{n}^*, \quad \boldsymbol{OD} = \boldsymbol{p}_B'^* = -\boldsymbol{p}_A'^*, \tag{22}$$

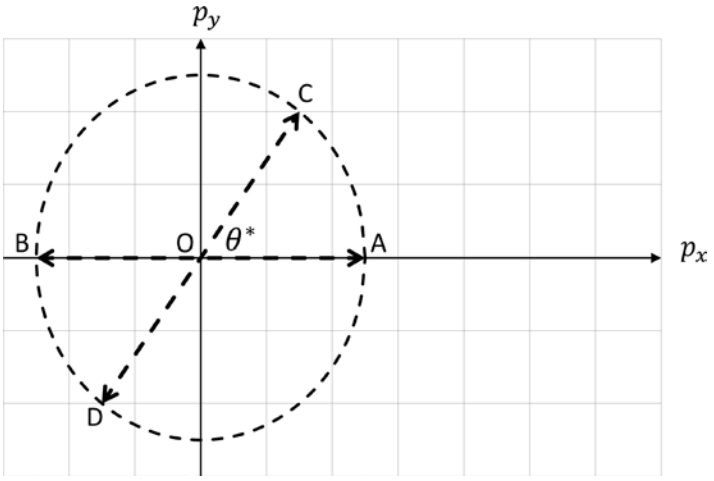

Figure 2. Collision in the center-of-mass system. The figure shows the case that the projectile A has mass $m_A = 3$ and velocity $v_A = \frac{8}{3}$ and the target B has mass $m_A = 4$ and velocity $v_B = -\frac{1}{4}$. The vectors $\boldsymbol{OA} = \boldsymbol{p}_A^* = (5,0) = -\boldsymbol{OB} = -\boldsymbol{p}_B^*$ are the momenta of incident particles before the collision. The vector $\boldsymbol{OC} = \boldsymbol{p}_A'^*$ and $\boldsymbol{OD} = \boldsymbol{p}_B'^*$ are the momentum of outgoing particles after collision. The angle $\angle COA = \theta^*$ cannot be determined by the conservation laws only. We fix it according to the given collision problem.

where $\boldsymbol{n}^* = (\cos\theta^*, \sin\theta^*)$ or $\theta^* = \angle COA$ is determined according to what we are asked in the collision problems. Since the scattering angle θ^* cannot be determined by the conservations of momentum and energy, the point C lies anywhere on this circle and the point D is opposite side against the point C on the circle.

3.2. Laboratory System

Next, as shown in **Figure 3**, we determine the point E on the p_x-axis so that $\boldsymbol{OE} = m_A\boldsymbol{V}$. We draw another circle centered at E whose radius is the same as the dashed circle centered at O. This circle centered at E is appeared in the book of Landau and Lifshitz [5], and its equation is written by Equation (18). This circle describes the laboratory system as explained below.

As shown in **Figure 3**, we draw a broken line from the point C in parallel to the p_x-axis until the broken line intersects with the circle centered at E. We call this point of intersection as F. Note that $\boldsymbol{OC} = \boldsymbol{EF}$ is always satisfied and it means $\angle COA = \angle FEA = \theta^*$. Then, the vector $\boldsymbol{OF} = \boldsymbol{p}_A'$ shows the momentum of the projectile A after the collision in the laboratory system. The tips of $\boldsymbol{OF} = \boldsymbol{p}_A'$ is always on the circle centered at E. The angle $\angle FOE = \theta$ is the scattered angle of the projectile A in the laboratory system. We note that the angle θ^* in **Figure 2** and the angle θ in **Figure 3** are related each other. Once the θ^* is given by the collision problems, the θ is determined according to the prescription stated above. And the converse is also true. When the θ is given in the collision problem, we write down the vector $\boldsymbol{OF} = \boldsymbol{p}_A'$ at first. Then, we

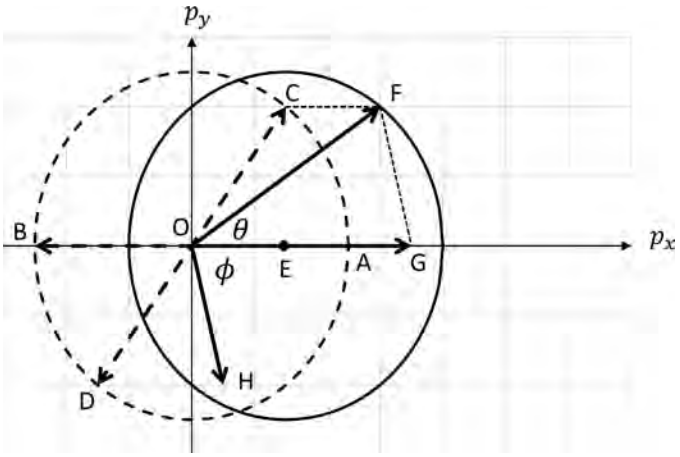

Figure 3. Circle centered at E describes the collision in the laboratory system. The initial condition in **Figure 2** shows that $OE = m_A V = 3$ and $EG = m_B V = 4$. The vectors $\boldsymbol{OF} = \boldsymbol{p}'_A$ and $\boldsymbol{OH} = \boldsymbol{p}'_B$ indicate the momenta of the projectile and the target after the collision in the laboratory system.

draw a broken line from the point F to C. The vector $\boldsymbol{OC} = \boldsymbol{p}'^*_A$ and the angle θ^* are the momentum and the scattered angle of the projectile A in the center-of-mass system.

Next, we determine the point G on the p_x-axis so that $\boldsymbol{EG} = m_B \boldsymbol{V}$. Then the vector $\boldsymbol{FG} = \boldsymbol{OH} = \boldsymbol{p}'_B$ shows the momentum of the target B after the collision. The angle $\angle GOH = \angle FGO = \phi$ is the scattered angle of the target B. The vector relation $\boldsymbol{OG} = \boldsymbol{OE} + \boldsymbol{EG} = \boldsymbol{OF} + \boldsymbol{OH}$ shows the momentum conservation $\boldsymbol{p}_A + \boldsymbol{p}_B = \boldsymbol{p}'_A + \boldsymbol{p}'_B$ before and after the collision.

In contrast with the equations in the previous section, what we need to do are the calculation of the radius of the circle and the lengths OE and EG. They are uniquely determined from the initial condition of the collision. We fix the angle θ or θ^* according to the given collision problems.

4. $v_B = 0$ Case

Let us consider the case where the target B is at rest $\boldsymbol{v}_B = \boldsymbol{0}$ before the collision. In that case, the point G definitely lies on the circle centered at E because of $|\boldsymbol{OC}| = |\boldsymbol{EF}| = |\boldsymbol{EG}|$, *i.e.* $p^*_A = p^*_B = m_B V$, which is understood by Equations ((4) and (15)). The circle centered at E is described by Equation (19) and is depicted in **Figure 4**. The vector $\boldsymbol{OG}$ is equal to the momentum $\boldsymbol{p}_A$ of the projectile A before the collision.

The point E lies inside or outside the dashed circle centered at O, according as $m_A < m_B$ and $m_A > m_B$. The corresponding diagrams are shown in **Figure 4** and **Figure 5**. It is evident from these figures that θ and ϕ can be expressed in terms of θ^* by

$$\tan\theta = \frac{EF\sin\theta^*}{OE + EF\cos\theta^*} = \frac{m_B V\sin\theta^*}{m_A V + m_B V\cos\theta^*} = \frac{\sin\theta^*}{\cos\theta^* + \dfrac{m_A}{m_B}}, \tag{23}$$

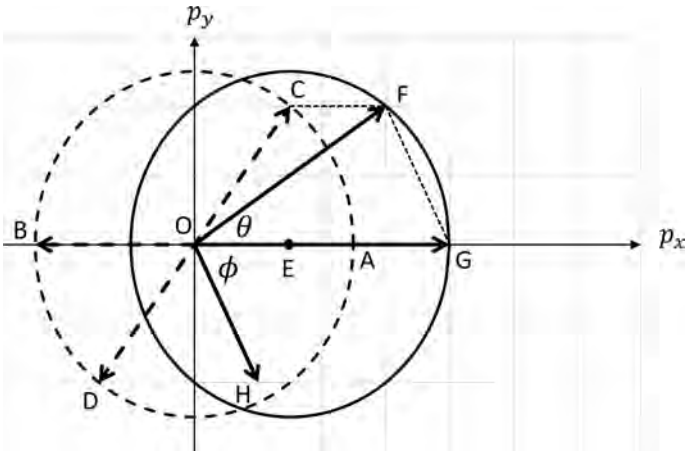

Figure 4. The initial conditions $m_A = 3$, $v_A = \frac{8}{3}$ and $m_B = 5$, $v_B = 0$ show $OC = EF = 5$ and $V = 1$. Then, $OE = m_A V = 3$ and $EG = m_B V = 5$.

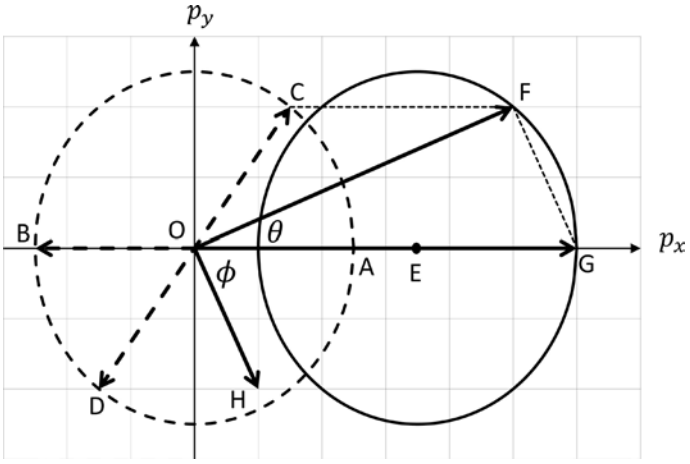

Figure 5. The initial conditions $m_A = 7$, $m_B = 5$, $v_A = \frac{12}{7}$ and $v_B = 0$ show $OC = EF = 5$ and $V = 1$. Then, $OE = m_A V = 7$ and $EG = m_B V = 5$.

$$\tan\phi = \frac{EF\sin\theta^*}{EG - EF\cos\theta^*} = \frac{\sin\theta^*}{1-\cos\theta^*} = \frac{\sin\phi^*}{1+\cos\phi^*}, \tag{24}$$

where we use the relation $\theta^* + \phi^* = \pi$. It is also evident that since the triangle ΔEFG is an isosceles triangle, we obtain $\phi = \frac{\pi - \theta^*}{2}$.

Applying the law of cosine to the triangle ΔOEF:
$OF^2 = OE^2 + EF^2 - 2\cdot OE\cdot EF\cos\left(\pi - \theta^*\right)$, we obtain

$$v_A' = \frac{v_A}{m_A + m_B}\sqrt{m_A^2 + m_B^2 + 2m_A m_B\cos\theta^*}. \tag{25}$$

The same application to the triangle ΔEFG gives

$$v_B' = \frac{2m_A v_A}{m_A + m_B}\sin\frac{\theta^*}{2}. \tag{26}$$

If $m_A > m_B$, however, the projectile A can be deflected only through an angle not exceeding $\theta_{\max} = \angle FOA$ from its original direction, as shown in Figure 6. This maximum value of $\theta_{\max}$ corresponds to the position F at which OF is a tangent to the circle centered at E. Evidently,

$$\sin\theta_{max} = \frac{EF}{OE} = \frac{EG}{OE} = \frac{m_B V}{m_A V} = \frac{m_B}{m_A}, \tag{27}$$

because $EF = EG$ are both the radius of the circle.

The case $m_A = m_B$ becomes quite simple as shown in Figure 7. The circle centered at E is described by Equation (20). The point E lies on the dashed circle centered at O, *i.e.* $OA = OE$. The p_y-axis is a tangent to the circle centered at E. It is evident from the figure that $\theta^* = 2\theta$. Further, Equations ((25) and (26)) become

$$v'_A = v_A \cos\frac{\theta^*}{2}, \quad v'_B = v_A \sin\frac{\theta^*}{2}. \tag{28}$$

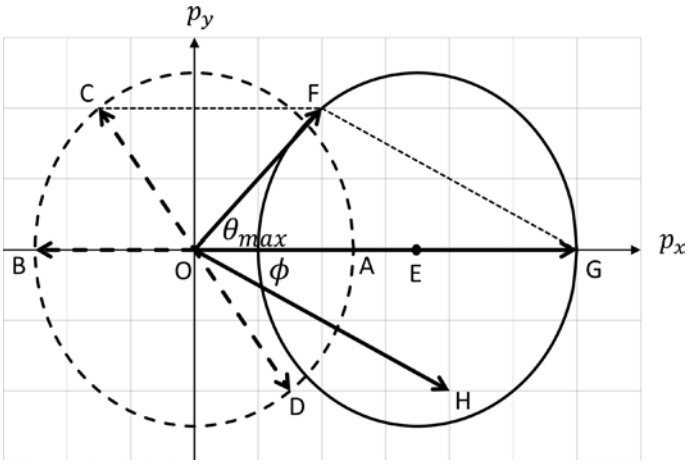

Figure 6. The initial condition is as the same with Figure 5. If $m_A > m_B$, the projectile A can be deflected only through an angle not exceeding $\theta_{\max} = \angle FOA$ from its original direction.

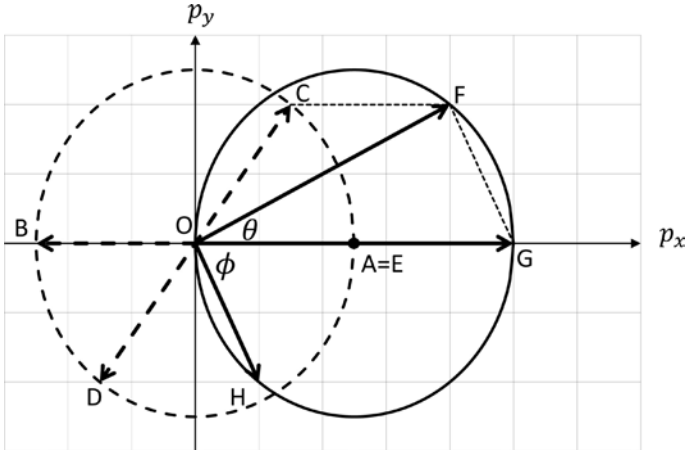

Figure 7. The initial conditions $m_A = m_B = 5$, $v_A = 2$ and $v_B = 0$ show $EF = 5$ and $V = 1$. Then, $m_A V = OE = 5 = m_B V = EG$.

After the collision, the outgoing particles move at right angles to each other, that is $\theta + \phi = \frac{\pi}{2}$.

5. Conclusion

We introduce two circles to analyze the two dimensional elastic collision in momentum space. One circle is for the center-of-mass system and the other is for the laboratory system. The relation between these two systems is clearly understood from these circles. Once we fix the scattered angle of projectile in one system, then we deduce all quantities, such as momenta and scattering angles of both particles in another system. The scattering problem in the special relativistic case is carried out in the next article.

Acknowledgements

The author thanks the anonymous reviewer for his helpful suggestions.

Conflicts of Interest

The authors declare no conflicts of interest regarding the publication of this paper.

References

[1] Giancoli, D.C. (1991) Physics, Principles with Applications. Prentice-Hall, Upper Saddle Rive.

[2] Young, H.D. and Freedman, R.A. (2008) University Physics. Pearson Addison Wesley, Boston.

[3] Ogura, A. (2017) Analyzing Collisions in Classical Mechanics Using Mass-Momentum Diagrams. *European Journal of Physics*, **38**, 055001. https://doi.org/10.1088/1361-6404/aa750b

[4] Bokor, N. (2011) Analysing Collisions Using Minkowski Diagrams in Momentum Space. *European Journal of Physics*, **32**, 773. https://doi.org/10.1088/0143-0807/32/3/013

[5] Landau, L.D. and Lifshitz, E.M. (1976) Mechanics. Butterworth-Heinenann, Oxford.

World Journal of Mechanics, 2018, 8, 353-361
http://www.scirp.org/journal/wjm
ISSN Online: 2160-0503
ISSN Print: 2160-049X

Diagrammatic Approach for Investigating Two Dimensional Elastic Collisions in Momentum Space II: Special Relativity

Akihiro Ogura

Laboratory of Physics, Nihon University, Matsudo, Japan
Email: ogura.akihiro@nihon-u.ac.jp

How to cite this paper: Ogura, A. (2018) Diagrammatic Approach for Investigating Two Dimensional Elastic Collisions in Momentum Space II: Special Relativity. *World Journal of Mechanics*, **8**, 353-361.
https://doi.org/10.4236/wjm.2018.89026

Received: August 2, 2018
Accepted: August 28, 2018
Published: August 31, 2018

Abstract

The diagrammatic approach to the collision problems in Newtonian mechanics is useful. We show in this article that the same technique can be applied to the case of the special relativity. The two circles play an important role in Newtonian mechanics, while in the special relativity, we need one circle and one ellipse. The circle shows the collision in the center-of-mass system. And the ellipse shows the collision in the laboratory system. These two figures give all information on two dimensional elastic collisions in the special relativity.

Keywords

Two Dimensional Elastic Collision, Momentum Space, Laboratory System, Center-of-Mass System, Special Relativity

1. Introduction

Collisions of the interacting particles have fundamental importance in physics. We often use the accelerated particles to investigate the substances. Cosmic ray which is often accelerated up to almost the speed of light collides with other particles in the air. For those particles which have high energy, special relativity has to be considered to investigate the collisions.

Diagrammatic technique gives the powerful tool to investigate the collision in Newtonian mechanics [1] [2] [3]. In this article, we apply it to the relativistic collision problems [4] [5]. The two circles played an important role in Newtonian mechanics, while in the special relativity one circle and one ellipse play a crucial role. When the speed of the projectile tends to small compared to the speed of light, the ellipse becomes a circle and the Newtonian case recover in

this limit [5].

This paper is organized in the following way. In Section 2, we recall two dimensional elastic collisions with equations. In Section 3, we show the diagrammatic approach for two dimensional elastic collision in order. First, we draw a circle for the center-of-mass system. Then we add to draw an ellipse to obtain the momentum after the collision in the laboratory system. In Section 4, we investigate the special case in which the two particles are identical. We also compare the cases that the projectile has different speed and we find that the low speed limit recovers the Newtonian case [3] [5]. Section 5 is devoted to a conclusion.

2. Elastic Collision between Two Particles in Two Dimensions

Let us take a look the two dimensional elastic collision for later use. **Figure 1** shows the collisions from the point of view in the laboratory and center-of-mass system and also show the notation which we use in this article. The projectile A has mass m_A and the velocity $\boldsymbol{v}_A$ and the target B has mass m_B and the velocity $\boldsymbol{v}_B$ before the collision. These quantities are known parameters or initial conditions in the laboratory system. The velocities after the collision are distinguished by the primes. And the asterisk is attached to the parameter in the center-of-mass system. In this article, we restrict ourselves that the target particle is at rest $\boldsymbol{v}_B = \boldsymbol{0}$ in the laboratory system before the collision.

The relation between the laboratory and center-of-mass systems is governed by the Lorentz transformation [6]. Let $\beta = V/c$ be the relative velocity between two systems and is given by

$$\beta = \frac{p_A}{E_A/c + m_B c}, \tag{1}$$

where c is the speed of light. The momentum p_A is defined by its velocity v_A as $p_A = m_A v_A \Big/ \sqrt{1-(v_A/c)^2}$ and the energy is given by $E_A/c = \sqrt{p_A^2 + (m_A c)^2}$. The γ-factor is obtained by

$$\gamma = \frac{1}{\sqrt{1-\beta^2}} = \frac{E_A/c + m_B c}{\sqrt{(m_A c)^2 + (m_B c)^2 + 2E_A m_B}}. \tag{2}$$

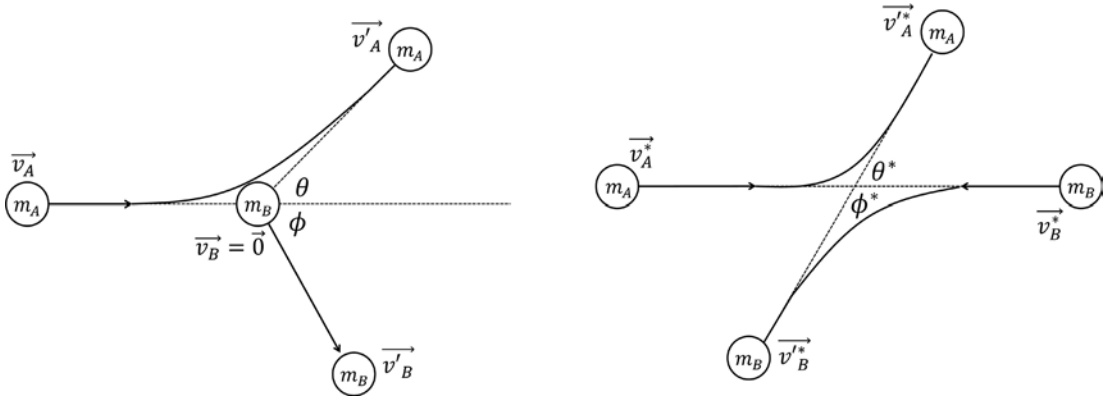

Figure 1. Left: Collisions in the laboratory system. Right: Collisions in the center-of-mass system.

From the Lorentz transformation, the momentum of the incident particles in the center-of-mass system is given by

$$p^* = p_A^* = p_B^* = \frac{p_A m_B c}{\sqrt{(m_A c)^2 + (m_B c)^2 + 2E_A m_B}}, \tag{3}$$

where note that the momenta in the center-of-mass system are the same in magnitude after the collision: $p^* = p_A'^* = p_B'^*$.

In the same way as the Newtonian mechanics [3], let $\boldsymbol{n}^* = (\cos\theta^*, \sin\theta^*)$ be the scattering angle of the projectile after the collision in the center-of-mass system. Since the angle θ^* is not determined by the conservations of energy and momentum, we fix it according to the collision problems. Let $\boldsymbol{p}_A' = (p_{Ax}', p_{Ay}')$ be the x, y-components of the momentum of the projectile in the laboratory system after the collision. The Lorentz transformation gives the relation between the laboratory system and center-of-mass system as follows:

$$p_{Ax}' = \beta\gamma E_A^*/c + \gamma p^* \cos\theta^*, \tag{4}$$

$$p_{Ay}' = p^* \sin\theta^*, \tag{5}$$

where $E_A^*/c = \sqrt{(p^*)^2 + (m_A c)^2} = E_A'^*/c$. From these equations and the relation $\cos^2\theta^* + \sin^2\theta^* = 1$, we obtain

$$\left(\frac{p_{Ax}' - \beta\gamma E_A^*/c}{\gamma p^*}\right)^2 + \left(\frac{p_{Ay}'}{p^*}\right)^2 = 1. \tag{6}$$

This equation indicates the ellipse [4] whose parameters

$$\text{minor semiaxis} \quad p^* = \frac{p_A m_B c}{\sqrt{(m_A c)^2 + (m_B c)^2 + 2E_A m_B}}, \tag{7}$$

$$\text{major semiaxis} \quad \gamma p^* = \beta\gamma E_B^*/c = \frac{p_A\{(m_B c)^2 + E_A m_B\}}{(m_A c)^2 + (m_B c)^2 + 2E_A m_B}, \tag{8}$$

$$\text{eccentricity} \quad \beta\gamma p^* = \frac{p_A^2 m_B c}{(m_A c)^2 + (m_B c)^2 + 2E_A m_B}, \tag{9}$$

$$\text{midpoint of foci} \quad \beta\gamma E_A^*/c = \frac{p_A\{(m_A c)^2 + E_A m_B\}}{(m_A c)^2 + (m_B c)^2 + 2E_A m_B}, \tag{10}$$

are uniquely determined by the initial conditions of the collision. The energy of the target in the center-of-mass system is defined by $E_B^*/c = \sqrt{(p^*)^2 + (m_B c)^2} = E_B'^*/c$, which is the same in magnitude before and after the collision.

3. Diagrammatic Technique

In this section, we deduce all relations, which we recalled in the former section, from the diagrammatic technique.

Firstly, we draw a dashed circle whose radius is $p_A^* = p_B^* = p^*$ in Equation (3), as depicted in **Figure 2**. The dashed circle shows the collision in the

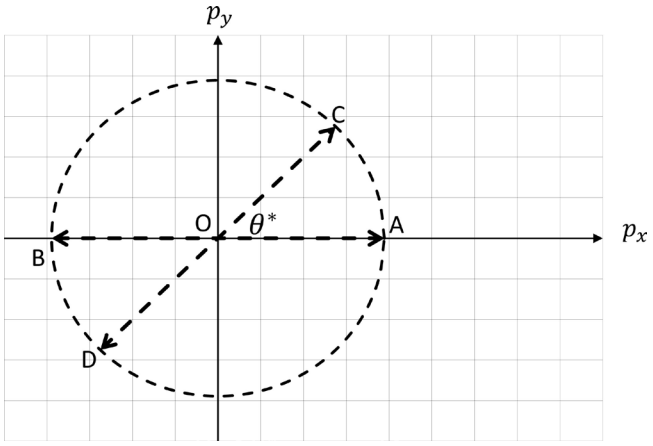

Figure 2. Collision in the center-of-mass system. The figure shows that the masses $m_A c = 4$ and $m_B c = 6$ and the velocity $v_A = 0.9c$ denote $p^* = 3.892$. The vectors $\boldsymbol{OA} = \boldsymbol{p}_A^*$ and $\boldsymbol{OB} = \boldsymbol{p}_B^*$ are the momenta of incident particles before the collision. The vectors $\boldsymbol{OC} = \boldsymbol{p}_A'^*$ and $\boldsymbol{OD} = \boldsymbol{p}_B'^*$ are the momenta of outgoing particles after the collision. The angle $\angle COA = \theta^*$ is not determined by the conservation laws only. We fix it according to the given collision problems.

center-of-mass system. Now, we draw arrows of momenta into the circle. The momenta before the collision are supposed to be along the *x*-axis

$$\boldsymbol{OA} = \boldsymbol{p}_A^*, \quad \boldsymbol{OB} = \boldsymbol{p}_B^* = -\boldsymbol{p}_A^*. \tag{11}$$

After the collision, the momenta stay the same in magnitude, but change the direction

$$\boldsymbol{OC} = \boldsymbol{p}_A'^*, \quad \boldsymbol{OD} = \boldsymbol{p}_B'^* = -\boldsymbol{p}_A'^*. \tag{12}$$

Since the scattering angle $\theta^* = \angle COA$ cannot be determined by the conservations of momentum and energy, the point C lies anywhere on the circle and the point D is opposite side against the point C. It is determined according to what we are asked in the collision problems.

Next, as shown in **Figure 3**, we draw an ellipse according to Equation (6) with the parameters from Equations (7) to (10). The point E is the midpoint of the foci E' and E''. This ellipse signifies $OE = \beta\gamma E_A^*/c$ and $EG = \beta\gamma E_B^*/c$, and we find from Equations (8) and (10) that

$$OG = p_A = \beta\gamma E_A^*/c + \beta\gamma E_B^*/c = OE + EG \tag{13}$$

is the momentum of the projectile in the laboratory system before the collision.

Next, as depicted in **Figure 4**, we draw a broken line from the point C in parallel to the p_x-axis until the broken line intersects with the ellipse. We call this point of intersection as F. Then, the vector $\boldsymbol{OF} = \boldsymbol{p}_A'$ becomes the momentum of the projectile A after the collision. The angle $\angle FOG = \theta$ is the scattered angle of the particle A in the laboratory system. We note that the angel θ^* in **Figure 2** and the angle θ in **Figure 4** are related each other. Once the θ^* is fixed by the given collision problems, the θ is determined according to the prescription stated above. And the converse is also true. If the collision problem

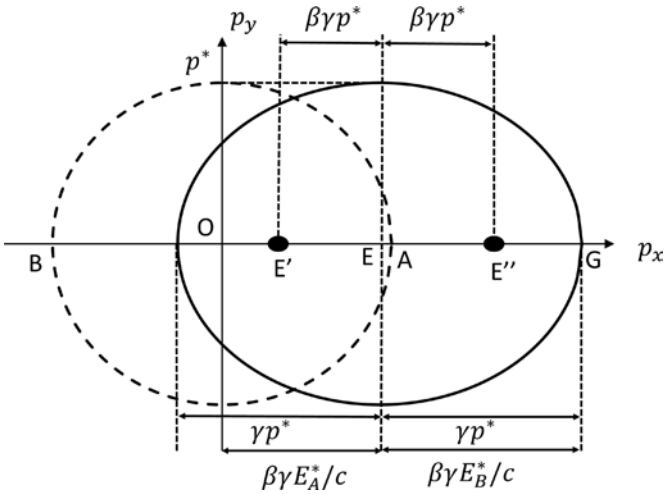

Figure 3. The ellipse Equation (6) can be drawn according as the parameters from Equations (7) to (10). The solid circle E' and E" on the p_x-axis are the foci of this ellipse. The point E is the midpoint of the foci.

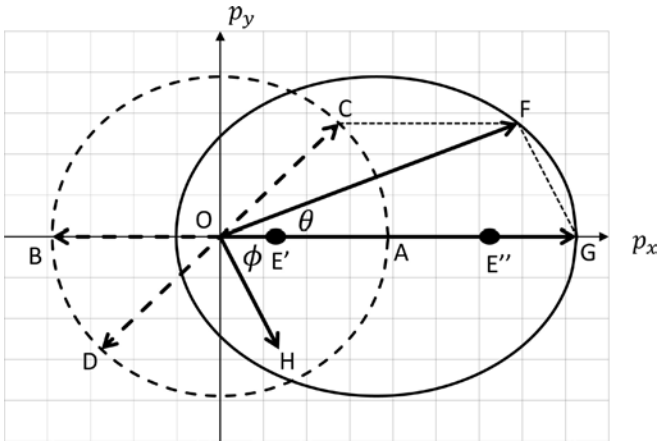

Figure 4. The ellipse implies the collision in the laboratory system in case of the incident velocity $v_A = 0.9c$. The initial condition is as the same with **Figure 2**. The solid circles on the p_x-axis denote the foci of the ellipse whose coordinates are $p_x = 6.144$ and 1.096. And the eccentricity is 2.524. The vectors $\boldsymbol{OF} = \boldsymbol{p}'_A$ and $\boldsymbol{OH} = \boldsymbol{FG} = \boldsymbol{p}'_B$ show the momenta of the projectile and the target after the collision.

gives the angle θ in the laboratory system, we first draw the vector $\boldsymbol{OF} = \boldsymbol{p}'_A$ in the ellipse. Then, we trace from F to C along the broken line. The vector $\boldsymbol{OC} = \boldsymbol{p}'^*_A$ shows the momentum of the projectile A in the center-of-mass system. And the angle $\angle COA = \theta^*$ is the scattered angle of this system.

Next, the vector $\boldsymbol{FG} = \boldsymbol{OH} = \boldsymbol{p}'_B$ shows the momentum of the target B in the laboratory system after the collision. The angle $\angle FGO = \angle GOH = \phi$ is the scattered angle of the target B. The vector $\boldsymbol{OG} = \boldsymbol{OE} + \boldsymbol{EG} = \boldsymbol{OF} + \boldsymbol{OH}$ shows the momentum conservation law $\boldsymbol{p}_A = \boldsymbol{p}'_A + \boldsymbol{p}'_B$ of the collision.

The ellipse has or has not intersections with p_y-axis, according as $m_A < m_B$ or $m_A > m_B$. It is found from the magnitude of γp^* and $\beta\gamma E_A^*/c$ in Equations (8) and (10). The corresponding diagrams are shown in **Figure 4** and

Figure 5. As we see from Figure 4 that if $m_A < m_B$, the projectile A can have any direction after the collision. However, in case of $m_A > m_B$ in Figure 5, the projectile A can be deflected only through an angle not exceeding $\theta_{\max}$ from its original direction. This case is shown in Figure 6. The maximum value of $\theta_{\max}$ is determined by the position F at which OF is a tangent to the ellipse.

4. Identical Particles and Newtonian Limit

The case $m_A = m_B = m$ becomes quite simple as shown in Figure 7. The parameters of the ellipse are as follows:

$$\text{minor semiaxis} \quad p^* = \frac{mcp_A}{\sqrt{2mc\left(E_A/c + mc\right)}}, \tag{14}$$

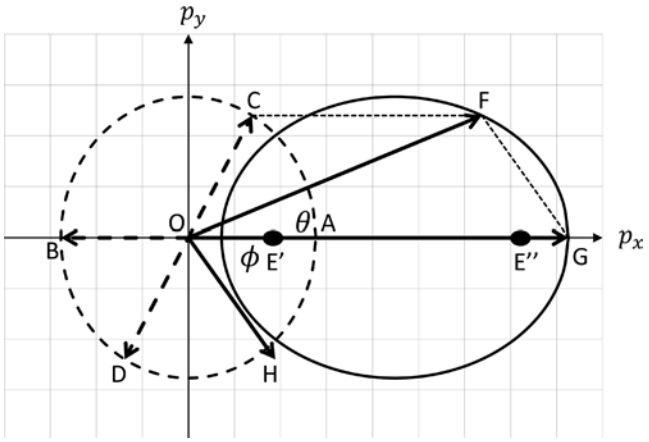

Figure 5. If $m_A > m_B$, the ellipse does not have intersections with the p_y-axis. The figure shows that the masses $m_A c = 4$ and $m_B c = 3$ and the velocity $v_A = 0.9c$ denote $p^* = 2.769$. The solid circles on the p_x-axis denote the foci of the ellipse whose coordinates are $p_x = 7.047$ and 1.935. And the eccentricity is 2.556.

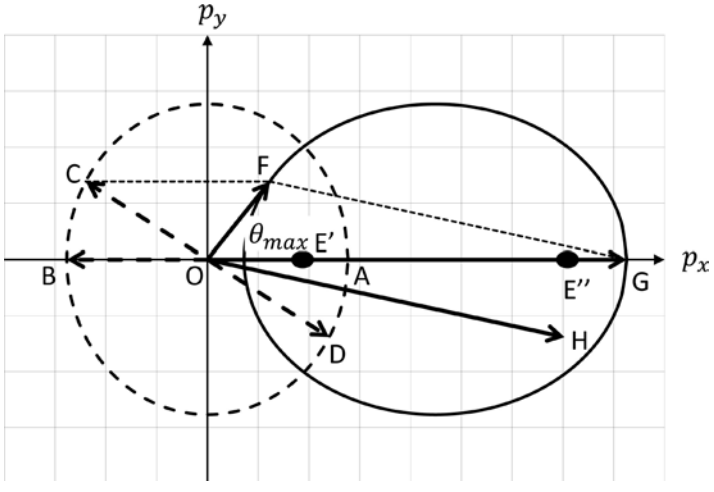

Figure 6. The initial condition is as the same with Figure 5. If $m_A > m_B$, the projectile A can be deflected only through an angle not exceeding $\theta_{\max} = \angle FOG$ from its original direction. The line segment OF is a tangent of the ellipse.

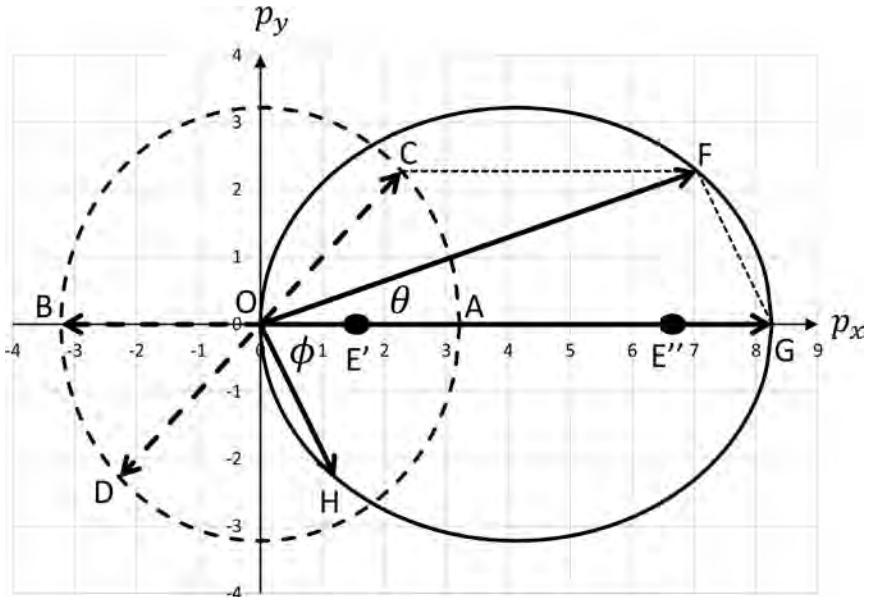

Figure 7. The incident particles have the same mass $m_A c = m_B c = mc = 4$. The p_y-axis is a tangent of the ellipse. The projectile with velocity $v_A = 0.9c$ collides with the target which is at rest. The solid circles on the p_x-axis denote the foci of the ellipse whose coordinates are $p_x = 1.541$ and 6.718. And the eccentricity is 2.588.

$$\text{major semiaxis} \quad \gamma p^* = \beta\gamma E_B^*/c = \frac{p_A}{2}, \tag{15}$$

$$\text{eccentricity} \quad \beta\gamma p^* = \frac{E_A/c - mc}{2}, \tag{16}$$

$$\text{midpoint of foci} \quad \beta\gamma E_A^*/c = \frac{p_A}{2}. \tag{17}$$

In this case, since $\gamma p^* = \beta\gamma E_A^*/c$, the p_y-axis becomes a tangent to the ellipse and the tip of the vector $\boldsymbol{OH} = \boldsymbol{p}_B'$ is also on the ellipse.

The cases of which the initial speed of the projectile A has $v_A = 0.6c$ and $v_A = 0.1c$ are shown in **Figure 8** and **Figure 9**. Here, we note that as we see from Equations (14)-(17), the different speed of the incident particle gives the different ellipse in magnitude. As the speed of the incident particle decreases, the eccentricity of the ellipse decreases and the ellipse begins to resemble a circle [3] [5]. It is found that if we take the limit with $c \to \infty$, the parameters in Equations (7)-(10) become

$$\text{minor semiaxis} \quad p^* \to \frac{m_B}{m_A + m_B} p_A, \tag{18}$$

$$\text{major semiaxis} \quad \gamma p^* = \beta\gamma E_B^*/c \to \frac{m_B}{m_A + m_B} p_A, \tag{19}$$

$$\text{eccentricity} \quad \beta\gamma p^* \to 0, \tag{20}$$

$$\text{midpoint of foci} \quad \beta\gamma E_A^*/c \to \frac{m_A}{m_A + m_B} p_A. \tag{21}$$

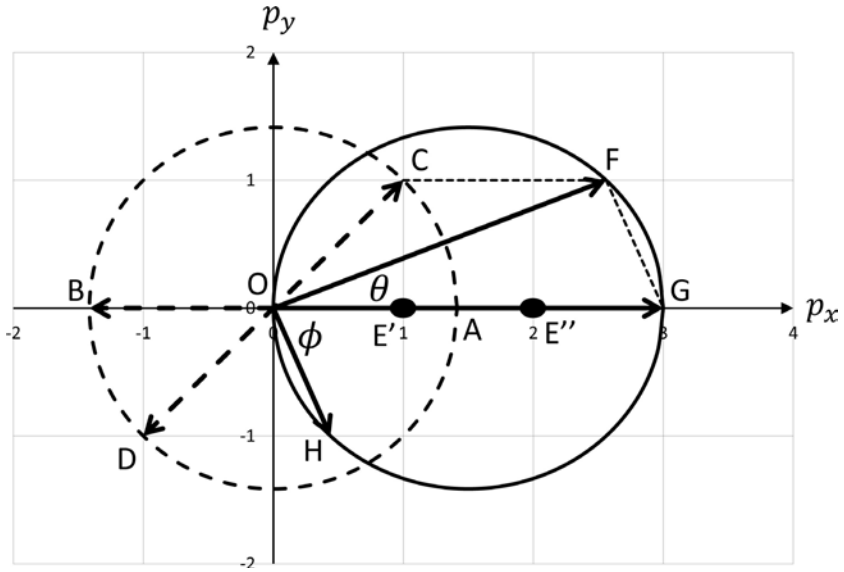

Figure 8. The incident particles have the same mass $m_A c = m_B c = 4$. The projectile A has the velocity $v_A = 0.6c$ and the target is at rest. The solid circles on the p_x-axis denote the foci of the ellipse whose coordinates are $p_x = 1$ and 2. And the eccentricity is 0.5.

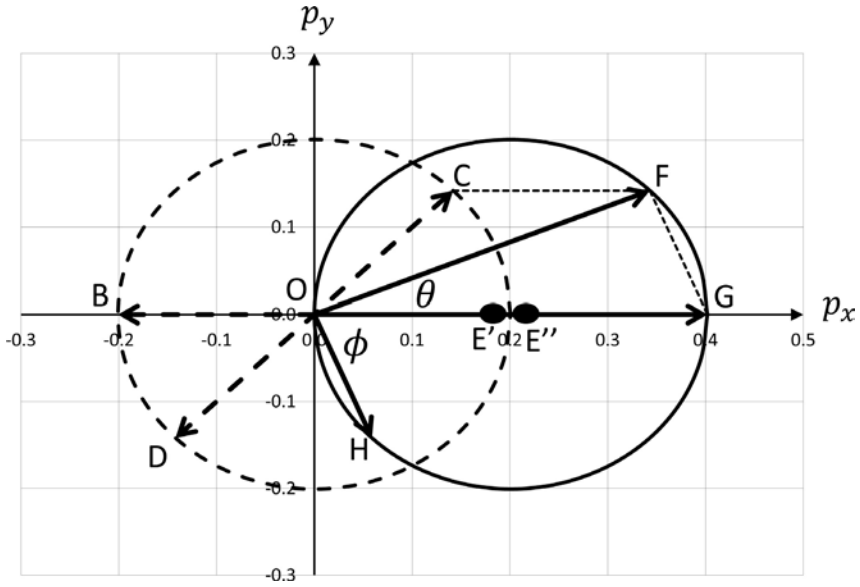

Figure 9. The incident particles have the same mass $m_A c = m_B c = 4$. The projectile A has the velocity $v_A = 0.1c$ and the target is at rest. The solid circles on the p_x-axis denote the foci of the ellipse whose coordinates are $p_x = 0.191$ and 0.211. And the eccentricity is 0.010.

The semiaxes become the same length and the eccentricity tends to zero. The case of the Newtonian collision problems [3] [5] is recovered in this limit.

5. Conclusion

We derive the diagrammatic presentation of the two dimensional elastic collision problem in the special relativity. We draw the circle for the center-of-mass

system and the ellipse for the laboratory system. Those circle and ellipse show the whole story of the two dimensional elastic collisions. When we use the graph paper for drawing those figures, we are able to measure the length of momentum vectors and the scattered angle by using the ruler and the protractor. This diagrammatic technique can help us understand collision problems qualitatively and quantitatively.

Acknowledgements

The author thanks the anonymous reviewer for his helpful suggestions.

Conflicts of Interest

The authors declare no conflicts of interest regarding the publication of this paper.

References

[1] Landau, L.D. and Lifshitz, E.M. (1976) Mechanics. Butterworth-Heinenann, Oxford.

[2] Ogura, A. (2017) Analyzing Collisions in Classical Mechanics Using Mass-Momentum Diagrams. *European Journal of Physics*, **38**, 055001. https://doi.org/10.1088/1361-6404/aa750b

[3] Ogura A. (2018) Diagrammatic Approach for Investigating Two Dimensional Elastic Collisions in Momentum Space I: Newtonian Mechanics. *World Journal of Mechanics*, **8**.

[4] Landau, L.D. and Lifshitz, E.M. (1976) The Classical Theory of Fields. Butterworth-Heinenann, Oxford.

[5] Bokor, N. (2011) Analysing Collisions Using Minkowski Diagrams in Momentum Space. *European Journal of Physics*, **32**, 773. https://doi.org/10.1088/0143-0807/32/3/013

[6] Goldstein, H., Poole, C. and Safko, J. (2002) Classical MECHANICS. Addison Wesley, Boston.

World Journal of Mechanics, 2018, 8, 362-377
http://www.scirp.org/journal/wjm
ISSN Online: 2160-0503
ISSN Print: 2160-049X

Transient MHD Couette Flow in a Rotating Environment Permeated by an Inclined Magnetic Field by Means of a Traveling Magnetic Field Subject to a Forced Oscillation

Swapan Kumar Ghosh

Department of Mathematics, Narajole Raj College, Narajole, West Bengal, India
Email: g_swapan2002@yahoo.com

How to cite this paper: Ghosh, S.K. (2018) Transient MHD Couette Flow in a Rotating Environment Permeated by an Inclined Magnetic Field by Means of a Traveling Magnetic Field Subject to a Forced Oscillation. *World Journal of Mechanics*, **8**, 362-377.
https://doi.org/10.4236/wjm.2018.89027

Received: August 17, 2018
Accepted: September 15, 2018
Published: September 18, 2018

Abstract

The present investigation reveals to a magnetohydrodynamic (MHD) start up flow of a rotating environment permeated by a traveling magnetic field with reference to a periodic driving force to explore the behaviour of a magnetic field at the resonant level. In a time varying electromagnetic field of sinusoidal in nature subject to $\nabla \cdot J \neq 0$, an oscillating current flow emerges the backbone of a radio emission in which the emission of hot electron gyrates in a magnetic field in the presence of a radiofrequency accelerator. The expedition of a radiofrequency field determines X-emission to expedite radiofrequency voltage under the influence of A.C circuit subject to $\nabla \cdot J \neq 0$. An oscillating current flow deals with an excitation frequency in such a way that phase angle rotates with angular frequency, the magnetic field grows towards the resonant level when the phase angle $\omega\tau = \pi/2$ is compatible with $\omega > 0$. In turn, plasma induced laser radiation is influenced by an oscillator with a decisive importance to an excitation frequency in the presence of a magnetic mirror so that maximum reflection occurs as the magnetic field increase in strength abruptly to exhibit resonance fluorescence. A synchronized laser photon light in transmitted from the Sun subject to $\omega\tau = \pi/2$.

Keywords

MHD Start Up Flow, Forced Oscillation, Stagnation, Radio Emission, X-Emission, Resonance Fluorescence, Laser Radiation

1. Introduction

In recent year, MHD Couette flow in a rotating system has received wide atten-

tion in literature. A literature survey reveals to the study of Ghosh [1] with a view to analyze the effects of Hall current on MHD Couette flow in a rotating system with arbitrary magnetic field. Guria *et al.* [2] studied an unsteady MHD Couette flow in a rotating system. Several studies have been made by the researchers with different conditions and configurations. Mention may be made on their works of Pai [3], Mondal *et al.* [4], Mondal and Mandal [5], Katagiri [6], Muhuri [7], Ghosh and Pop [8], Ghosh [9], Sengupta and Ray [10], Singh [11], Singh and Sharma [12]. Nevertheless, an MHD flow in a rotating system subject to a forced oscillation has been studied by Ghosh [13] and Ghosh *et al.* [14]. The aim of present investigation is to deal with the configuration of the Sun in the presence of a radiofrequency accelerator. Sun is an MHD in the presence of a radiofrequency accelerator permeated by a magnetic mirror. The configuration of the Sun leads to vacuum in the presence of radiofrequency accelerator so that frictional layer at the boundary suddenly sets into motion leading to a start up flow. It reveals that in space, pressure is far below normal atmospheric pressure and the flow is oscillating in nature with reference to a driving force. A magnetic mirror with the Sun represents a controlled thermonuclear fusion reaction to expedite an MHD of the Sun. In this situation, a magnetic mirror is the representation of an inclined magnetic field. Since forced oscillation is taken into account, a physical system is acted upon by an external periodic driving force in which the resulting amplitude of oscillation of the system becomes large when the frequency of the driving force approaches a natural frequency of oscillation of the system. In turn, internal energy is converted into kinetic energy during convection process and a maximum dissipation of energy is liberated from the Sun with large amplitude when kinetic energy is transformed into heat. The growing magnetic field at the resonance level leads to a driving force in the presence of a magnetic mirror. Although a radiofrequncy accelator generates a radio wave propogation into the atmosphere to expedite oceanic circulation with reference to a magnetic mirror at the resonant level. An expedition of a radio wave in a vacuum emerges the exploration of atmospheric science which is visible in the Earth's atmosphere. This situation reveals that light wave is transmitted in the form of a radio wave with a decisive importance to a controlled thermonuclear fusion reaction of the Sun. To increase radiofrequency voltage, the emission of hot electron gyrates in a magnetic field to exhibit radio emission with a synchronization of X-emission so that magnetic field oscillates in a vacuum. In turn, X-emission determines an irregular fluctuation of a magnetic field in a vacuum. Sun is a MHD with a decisive importance to a magnetic mirror where plasma fusion takes place in a magnetic field at the resonant level with reference to a controlled thermonuclear fusion reaction. An oscillator takes place of a driving force in the presence of a magnetic mirror with the Sun exerts its influence of a plasma induced laser radiation so that the system rotates with angular frequency with the growing of a magnetic field towards the resonant level and the angular frequency is determined by the phase angle

subject to a periodic driving force. The situation reveals that the magnetic field increases in strength abruptly in the presence of a magnetic mirror and the reflection occurs with an abrupt increase in magnetic field to exhibit resonance fluorescence when phase angle is π/2. This indicates that a synchronized photon light is transmitted from the Sun. A radiofrequency accelerator with the Sun corresponds to the differential rotation of the Sun; an irregular fluctuation of hot electron is liberated from the Sun with an increase in differential rotation subject to a cyclonic turbulence so that magnetic field changes its direction abruptly from the central region. Since forced oscillation is taken into account, the differential rotation of the Sun subject to a periodic driving force maintains a similar rotation of the Earth that may cause an effect of solar eclipse.

The aim of present investigation is to study of an MHD start up flow when the frictional layer is suddenly sets into motion. Since the flow is induced by a forced oscillation its motion is subjected to an external periodic driving force which oscillates harmonically with time. MHD start up flow in a rotating environment is influenced by an inclined magnetic field with the positive direction of the axis of rotation. Since the motion is sinusoidal in nature, there arise a fluctuation at every point on the flow field with reference to $\nabla \cdot J \neq 0$ due to the existance of a displacement current. An A.C circuit is furnished under electrical relay analogy to expedite an inclined magnetic field that leads to a radiofrequency voltage and the magnetic field grows towards the resonant level. A strong ionizing radiation inside the solar atmosphere becomes predominant.

2. Formulation of the Problem and Its Solutions

A transient hydromagnetic (MHD) start up flow of a viscous incompressible electrically conducting fluid confined between parallel plates lying at a distance "d" apart, rotating with an uniform angular velocity Ω about an axis perpendicular to their planes in the presence of an inclined magnetic field with the positive directionof the axis of rotation with reference to a forced oscillation permeated by an oscillator, is studied. To choose the cartesian co-ordinate system in such a way that the upper plate is moving with an uniform velocity U relative to the rotating frame of reference while the lower plate is kept fixed so that x and z axis lying on the lower plate and y-axis is perpendicular to it. Since the plates are infinite along x and z direction, all physical quantities will be functions of y and τ only.

The following justifications are compatible with the fundamental equations of magnetohydrodynamics

$$\begin{aligned} &q = \left(u', 0, w'\right);\ \ B = \left(B_x' + B_0 \sin\theta, B_0 \cos\theta, B_z'\right) \\ &E = \left(E_x, E_y, E_z\right);\ \ J = \left(J_x, J_y, J_z\right) \end{aligned} \tag{1}$$

where q, B, E and J are respectively the velocity vector, magnetic field vector, electric field vector and the current density vector.

The MHD momentum equation in a rotating frame of reference reads

$$\frac{\partial q}{\partial t}+(q\cdot\nabla)q+2\Omega\hat{k}\times q=\nu\nabla^2 q+\frac{1}{\rho}J\times B \tag{2}$$

The equation of continuity becomes

$$\nabla\cdot q=0 \tag{3}$$

The Ohm's law for a moving conductor

$$J=\sigma\left[E+q\times B\right] \tag{4}$$

The Maxwell's equations are

$$\begin{aligned}&\nabla\times B=\mu_e J\\&\nabla\times E=-\frac{\partial B}{\partial t}\\&\nabla\cdot B=0\\&\nabla\cdot J\neq 0\end{aligned} \tag{5}$$

where, σ, ν, ρ, μ_e, Ω and $\hat{k}$ are, respectively, the electrical conductivity, kinematic coefficient of viscosity, fluid density, magnetic permeability, angular velocity and a unit-vector along y-axis. B_0 is the magnetic flux density and θ is the angle of inclination of a magnetic field with the positive direction of the axis of rotation.

In general, the electric current flowing in the fluid distorts the applied magnetic field. Since the frictional layer at the boundary is suddenly sets into motion to produce thermally ionized air which is the best of poor electrical conductor, it is permissible to neglect the induced magnetic field as compared to applied one (Pai [3]). Thus the magnetic field vector can be taken as $B=\left(B_0\sin\theta, B_0\cos\theta, 0\right)$. Since no external electric field is applied, the polarization voltage is negligible. Therefore, it is reasonably assumed as $E = 0$ (Meyer [15]).

Under the justification (1) the MHD momentum equations in a rotating frame of reference subject to a component form together with the Ohm's law for a moving conductor (4) in relation with the Maxwell's Equation (5) can be written in the following form

$$\frac{\partial u'}{\partial t}+2\Omega w'=\nu\frac{\partial^2 u'}{\partial y^2}-\frac{\sigma B_0^2}{\rho}u'\cos^2\theta \tag{6}$$

$$\frac{\partial w'}{\partial t}-2\Omega u'=\nu\frac{\partial^2 w'}{\partial y^2}-\frac{\sigma B_0^2}{\rho}w' \tag{7}$$

The boundary conditions are

$$\begin{aligned}&u'=w'=0 \text{ for } t\le 0, 0\le y\le d,\\&u'=w'=0 \text{ at } y=0, t>0,\\&u'=U, w'=0 \text{ at } y=d, t>0.\end{aligned} \tag{8}$$

Equations ((6) and (7)) can be written in a dimensionless form such as

$$\frac{\partial^2 u}{\partial\eta^2}-\frac{\partial u}{\partial\tau}-M^2 u\cos^2\theta=2K^2 w, \tag{9}$$

$$\frac{\partial^2 w}{\partial \eta^2} - \frac{\partial w}{\partial \tau} - M^2 w = -2K^2 u \tag{10}$$

where $\eta = \frac{y}{d}$, $u = \frac{u'}{U}$, $w = \frac{w'}{U}$, $t = \frac{d^2\tau}{\nu}$,

$M = B_0 L(\sigma/\rho\nu)^{1/2}$ is the Hartmann number and (11)

$K^2 = \frac{\Omega d^2}{\nu}$ is the rotation parameter which is the reciprocal of Ekman number.

The corresponding boundary conditions are

$$\begin{aligned} &u = w = 0 \text{ for } \tau \le 0 \text{ and } 0 \le \eta \le 1, \\ &u = 0, w = 0 \text{ at } \eta = 0, \tau > 0, \\ &u = F(\tau), w = 0 \text{ at } \eta = 1, \tau > 0 \end{aligned} \tag{12}$$

Since forced oscillation is taken into account, it is reasonably assumed

$$\begin{aligned} u(\eta,\tau) &= u_0(\eta)\cos\omega\tau \\ w(\eta,\tau) &= w_0(\eta)\cos\omega\tau \end{aligned} \tag{13}$$

The corresponding boundary conditions

$$\begin{aligned} &u = 0, w = 0 \text{ at } \eta = 0, \tau > 0, \\ &u = \cos\omega\tau, w = 0 \text{ at } \eta = 1, \tau > 0. \end{aligned} \tag{14}$$

Equations ((9) and (10)) are in agreement with $\nabla \cdot J \neq 0$ subject to $J = (J_x, J_y, J_z)$. This study leads to a displacement current effect due to an external periodic driving force subject to a forced oscillation in the presence of an inclined magnetic field with regard to $\nabla \cdot J \neq 0$. When a displacement current is taken into account, it is possible to consider even those situations which involve non-steady current *i.e.* situation where $\nabla \cdot J \neq 0$. A.C circuit furnish a special case of time varying electromagnetic phenomenon, where all the variations are sinusoidal in character. The action of such circuits with capacitors as circuit elements can be understood on the basis of the displacement current. Indeed, in a time varying electromagnetic field of sinusoidal in nature subject to $\nabla \cdot J \neq 0$, an inclined magnetic field is the representation of a traveling magnetic field.

Using (13), the Equations ((9) and (10)) can be solved subject to the boundary conditions (14) and solutions for the velocity distributions can be written in the following form.

$$\begin{aligned} u(\eta,\tau) = \Bigg[&\frac{M^2\sin^2\theta + iG^2}{2iG^2}\frac{\sinh(\alpha - i\beta)\eta}{\sinh(\alpha - i\beta)} \\ &- \frac{M^2\sin^2\theta - iG^2}{2iG^2}\frac{\sinh(\alpha + i\beta)\eta}{\sinh(\alpha + i\beta)}\Bigg]\cos\omega\tau \end{aligned} \tag{15}$$

$$w(\eta,\tau) = \frac{M^4\sin^4\theta + G^4}{8iK^2G^2}\left[\frac{\sinh(\alpha - i\beta)\eta}{\sinh(\alpha - i\beta)} - \frac{\sinh(\alpha + i\beta)\eta}{\sinh(\alpha + i\beta)}\right]\cos\omega\tau \tag{16}$$

where

$$\alpha,\beta=\frac{1}{2}\left\{\left[\left\{\left(1+\cos^2\theta\right)M^2-2\omega\tan\omega\tau\right\}^2+G^4\right]^{1/2}\pm\left\{\left(1+\cos^2\theta\right)M^2-2\omega\tan\omega\tau\right\}\right\}^{1/2} \tag{17}$$

and

$$G^2=\left(16K^4-M^4\sin^4\theta-4\omega^2\tan^2\omega\tau-4\omega^2\right)^{1/2} \tag{18}$$

Expressions (17) and (18) are in agreement with Ghosh [13].

The condition(18) can be expressed in the following form

$$\left(16K^4-M^4\sin^4\theta-4\omega^2\tan^2\omega\tau-4\omega^2\right)\begin{cases}>\\=0\\<\end{cases}\quad\text{according as}\quad G^4\begin{cases}>\\=0\\<\end{cases}$$

There arises three conditions in such a way that

$\omega>\frac{1}{2}\cos\omega\tau\left(16K^4-M^4\sin^4\theta\right)^{1/2}$, $\omega<\frac{1}{2}\cos\omega\tau\left(16K^4-M^4\sin^4\theta\right)^{1/2}$ and $\omega=\frac{1}{2}\cos\omega\tau\left(16K^4-M^4\sin^4\theta\right)^{1/2}$

In relevance to the condition $\omega>\frac{1}{2}\cos\omega\tau\left(16K^4-M^4\sin^4\theta\right)^{1/2}$ it is stated that a resonant response occurs with reference to a driving force with a decisive importance to the phase angle $\omega\tau=\pi/2$ to prove resonance when the excitation frequency $\omega>0$. Therefore, phase angle rotates with angular frequency of oscillation to build up a rapid oscillation of a charged particle and its amplification is very high when $\omega\tau=\pi/2$. In this situation, magnetic field grows towards the resonance level so that reflection occurs due to the presence of a magnetic mirror as the magnetic field increases in strength abruptly. This indicates that laser radiation is so intense due to the presence of a magnetic mirror at the resonant level. A radiofrequency accelarator with the Sun in the presence of a magnetic mirror leads to a controlled thermonuclear fusion reaction to produce plasma induced laser radiation due to a driving force subject to an oscillator at the resonant level to prove resonance fluorescence when $\omega\tau=\pi/2$ and a radio wave propagation from the Sun is visible in the sky (see Figure 1).

In a realistic situation, a radiofrequency accelerator with the Sun emerges the frictional layer at the boundary to set into motion so that space pressure is much below the atmospheric pressure as the air breaks down. In such a case the Sun is exposed to a vacuum and X-rays are liberated from the Sun. A synchroton radiation is transmitted from the Sun in a vacuum as the emission of hot electrons gyrating in a magnetic field to determine radio emission. A magnetic mirror with the Sun is the representation of an inclined magnetic field. A strong ionizing radiation inside the solar atmosphere to deal with plasma induced laser radiation at the resonant level.

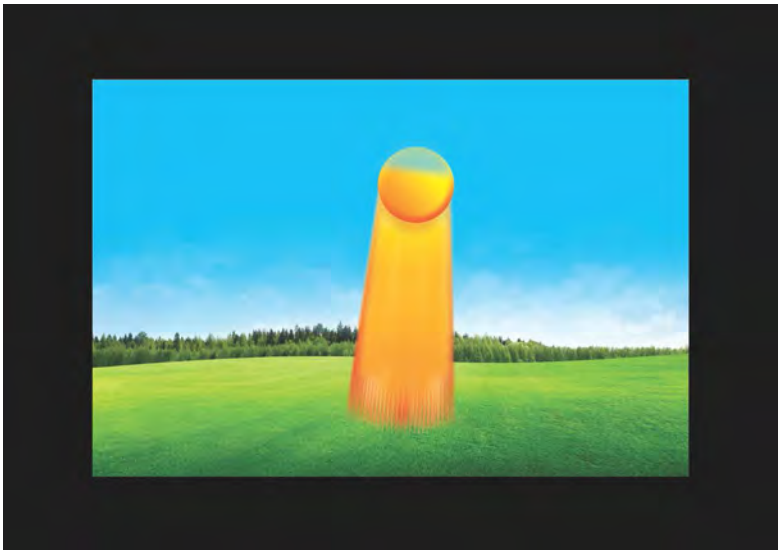

Figure 1. Plasma induced laser radiation shows resonance fluorescence to provide synchronized photon light in the presence of a radiofrequency accelerator under the influence of a magnetic mirror with reference to an oscillator in the context of dynamo mechanism of the Sun. Such a behavior of the Sun was visible in the sky with radio wave propagation in the year of 5th November, 2006.

In compliance with the condition, $\omega < \frac{1}{2}\cos\omega\tau\left(16K^4 - M^4\sin^4\theta\right)^{1/2}$ it is rigorously stated that no resonant response occurs when the phase angle $\omega\tau = \pi/2$ in accordance with the excitation frequency $\omega < 0$.

As referred to a condition $\omega = \frac{1}{2}\cos\omega\tau\left(16K^4 - M^4\sin^4\theta\right)^{1/2}$ there arise stagnation when the phase angle $\omega\tau = \pi/2$ is compatible with the excitation frequency $\omega = 0$. Since phase angle rotates with angular frequency of oscillation, there exists a stagnation so that the velocity will be zero if the excitation frequency is switched off. On the other hand, in the absence of phase angle *i.e.* $\omega\tau = 0$, the condition leads to an inertial frequency $\omega = \frac{1}{2}\left(16K^4 - M^4\sin^4\theta\right)^{1/2}$ in a rotating environment. This justification comes to a conclusion that the Sun is an activation of resonance in the presence of a driving force subject to the resonant condition $\omega > \frac{1}{2}\cos\omega\tau\left(16K^4 - M^4\sin^4\theta\right)^{1/2}$.

The solutions (15) and (16) together with (17) and (18) turn into the general form of a transient MHD start up flow in the presence of an inclined magnetic field if the phase angle is absent $\omega\tau = 0$ and the solutions (15) and (16) reduce to

$$u(\eta,\tau) = \left[\frac{M^2\sin^2\theta + iG^2}{2iG^2}\frac{\sinh(\alpha - i\beta)\eta}{\sinh(\alpha - i\beta)} - \frac{M^2\sin^2\theta - iG^2}{2iG^2}\frac{\sinh(\alpha + i\beta)\eta}{\sinh(\alpha + i\beta)}\right] \quad (19)$$

$$w(\eta,\tau) = \frac{M^4\sin^4\theta + G^4}{8iK^2G^2}\left[\frac{\sinh(\alpha - i\beta)\eta}{\sinh(\alpha - i\beta)} - \frac{\sinh(\alpha + i\beta)\eta}{\sinh(\alpha + i\beta)}\right] \quad (20)$$

where

$$\alpha,\beta=\frac{1}{2}\left[\left\{\left(1+\cos^2\theta\right)^2M^4+G^4\right\}^{1/2}\pm\left(1+\cos^2\theta\right)M^2\right]^{1/2} \tag{21}$$

and

$$G^2=\left(16K^4-M^4\sin^4\theta-4\omega^2\right)^{1/2} \tag{22}$$

Since phase angle rotates with angular frequency of oscillation, the presence of phase angle comes to a justification in two ways viz, $\omega>\frac{1}{2}\cos\omega\tau\left(16K^4-M^4\sin^4\theta\right)^{1/2}$ and $\omega<\frac{1}{2}\cos\omega\tau\left(16K^4-M^4\sin^4\theta\right)^{1/2}$. The former condition leads to a resonant response with reference to a dynamo mechanism of the system. The later is valid with the maintenance of a magnetic field and the resonant response do not occur. The inertial frequency of a rorating environment does exist when $\omega=\frac{1}{2}\left(16K^4-M^4\sin^4\theta\right)^{1/2}$.

In taken into account of the solutions (15) and (16) together with (17) and (18) it is stated that since the system rotates with phase angle; if the excitation frequency ω is switched off then then phase angle $\omega\tau$ is zero and the solutions reduce to a steady state MHD flow in a rotating environment subject to $u(\eta)$ and $w(\eta)$ for (19) and (20) where

$$\alpha,\beta=\frac{1}{2}\left[\left\{\left(1+\cos^2\theta\right)^2M^4+G^4\right\}^{1/2}\pm\left(1+\cos^2\theta\right)M^2\right]^{1/2}$$

and

$$G^2=\left(16K^4-M^4\sin^4\theta\right)^{1/2} \tag{23}$$

The condition (23) represents a dynamo context of a rotating environment.

3. Shear Stress at the Moving Plate $\eta = 1$

$$\left.\frac{\mathrm{d}u}{\mathrm{d}\eta}\right|_{\eta=1}=\left[\frac{M^2\sin^2\theta+iG^2}{2iG^2}\frac{(\alpha-i\beta)\cosh(\alpha-i\beta)}{\sinh(\alpha-i\beta)}-\frac{M^2\sin^2\theta-iG^2}{2iG^2}\frac{(\alpha+i\beta)\cosh(\alpha+i\beta)}{\sinh(\alpha+i\beta)}\right]\cos\omega\tau \tag{24}$$

$$\left.\frac{\mathrm{d}w}{\mathrm{d}\eta}\right|_{\eta=1}=\frac{M^4\sin^4\theta+G^4}{8iK^2G^2}\left[\frac{(\alpha-i\beta)\cosh(\alpha-i\beta)}{\sinh(\alpha-i\beta)}-\frac{(\alpha+i\beta)\cosh(\alpha+i\beta)}{\sinh(\alpha+i\beta)}\right]\cos\omega\tau \tag{25}$$

4. Discussion of Results

To study of an MHD Start up flow in a rotating system under the influence of a forced oscillation with reference to an inclined magnetic field; a periodic driving force generates an excitation frequency to exhibit resonance subject to $\nabla\cdot J\neq 0$.

This situation reveals that Ghosh inertal frequency coincides with free natural frequency of oscillation so that oscillation builds up rapidly with a driving force in which the resulting amplitude of oscillation of the system becomes large. Since phase angle rotates with angular frequency, the excitation frequency $\omega > \frac{1}{2}\cos\omega\tau\left(16K^4 - M^4\sin^4\theta\right)^{1/2}$ leads to resonance as the forcing wave to excites natural frequency in compliance with the phase angle $\omega\tau = \frac{\pi}{2}$ with a decisive importance to $\omega > 0$. A.C circuit furnishes with a non-steady current flow subject to $\nabla \cdot J \neq 0$ due to a periodic driving force and the growing of a magnetic field at the resonant level in which the emission of hot electron gyrates in a magnetic field to determine radio emission. A charged particle experiences an alternating current flow of sinusoidal in nature with reference to $\nabla \cdot J \neq 0$ that gives rise to radiofrequency voltage under A.C circuit. To increase radiofrequency voltage, the emission of hot electron exerts its influence of X-emission due to irregular fluctuation of a magnetic field in a vacuum. In a time varying electromagnetic field subject to $\nabla \cdot J \neq 0$, an MHD flow is influenced by a traveling magnetic field under the influence of a periodic driving force in the presence of an oscillator. A radiofrequency accelator with the Sun is inspired by a magnetic mirror in the presence of an oscillator. In this context, a controlled thermonuclear fusion reaction at the resonant level so that plasma fusion interacts with the supercritical state as the maximum dissipation of energy is liberated from the Sun with large amplitude when the kinetic energy is transformed into heat and the maximum reflection occurs as the strength of the magnetic field increases its strength abruptly to exhibit plasma induced laser radiation with the propagation of radio wave in the atmosphere.

The graphical discussion in relevance to a physical interpretation has been made with arbitrary values of θ, $\omega\tau$ and ω taking M^2 is fixed in **Figures 2-5**. **Figure 2** reveals that the velocity is exerted by the flow field to increase with an increase the angle of inclination of a magnetic field θ. This happens in the case of a traveling magnetic field in a time varying electrmagnetic field to distort magnetic lines of force due to the presence of Lorentz force with reference to a dynamo machanism of the system. Since the system rotates with angular frequency the velocity is closely resemblance to a resonance when the angle of inclination of a magnetic field $\theta = \pi/2$. In a time varying electromagnetic field, the magnetic field grows towards the resonant level. In relating to the previous literature, the foundation of the behaviour of an inclined magnetic field in a rotating system does not scope to appear the concept of increasing the angle of inclination of a magnetic field θ. This concept lies on its behaviour of a magnetic field subject to $\nabla \cdot J \neq 0$ at resonance. It is evident from **Figure 3** that the velocity increases in the main flow (u) with an increase in magnetic force (M^2) while the velocity decreases in the cross flow (W) with an increase inmagnrtic force (M^2). This situation happens in the case of a main flow (u) to exerts its influence of an angle of inclination of a magnetic field $\theta = \pi/2$ where the

Lorentz force is an active influence to distort the magnetic lines of force in the presence of a periodic driving force. In a time varying electromagnetic field, the magnetic field grows subjected to a plasma fusion on heating of plasma in a controlled region at the resonant level when $\theta = \pi/2$. Thus magnetic pumping in a time varying electromagnetic field becomes predominant. Since the velocity decreases in the cross flow(w), a destabilizing influence on the behaviour of a magnetic pressure leads to fall the velocity due to the presence of Lorentz force when $\theta = \pi/2$. In general, Lorentz force destabilize the flow situation with an increase in magnetic force. In a radiofrequency field subject to a oscillating current flow in the presence of a forced oscillation, A.C circuit furnishes to

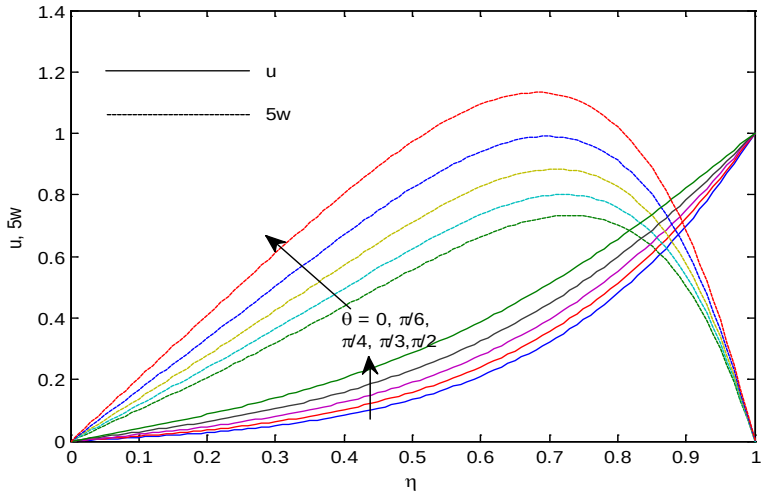

Figure 2. u and w for different values of $\theta = 0, \frac{\pi}{6}, \frac{\pi}{4}, \frac{\pi}{3}$ and $\frac{\pi}{2}$ with $M^2 = 10, K^2 = 5, \omega = 0.2$ and $\omega\tau = 0$.

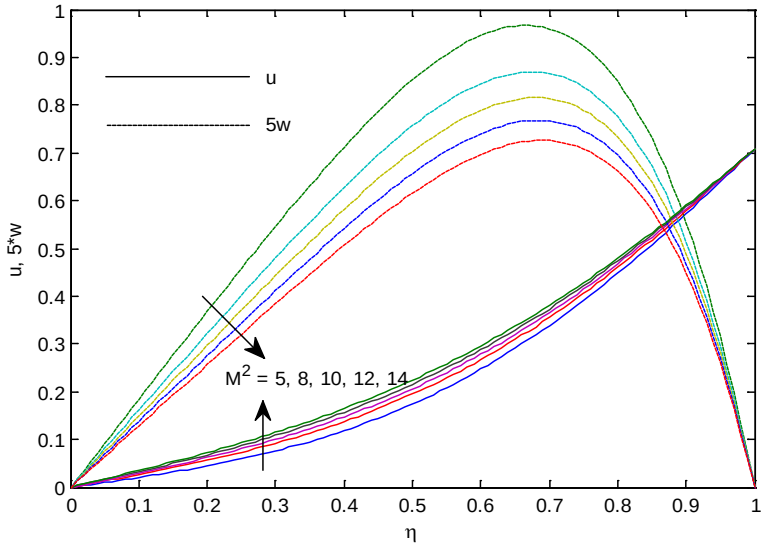

Figure 3. u and w for different values of $M^2 = 5, 8, 10, 12$ and 14 with $K^2 = 5, \omega = 0.2, \omega\tau = \frac{\pi}{4}$ and $\theta = \frac{\pi}{2}$.

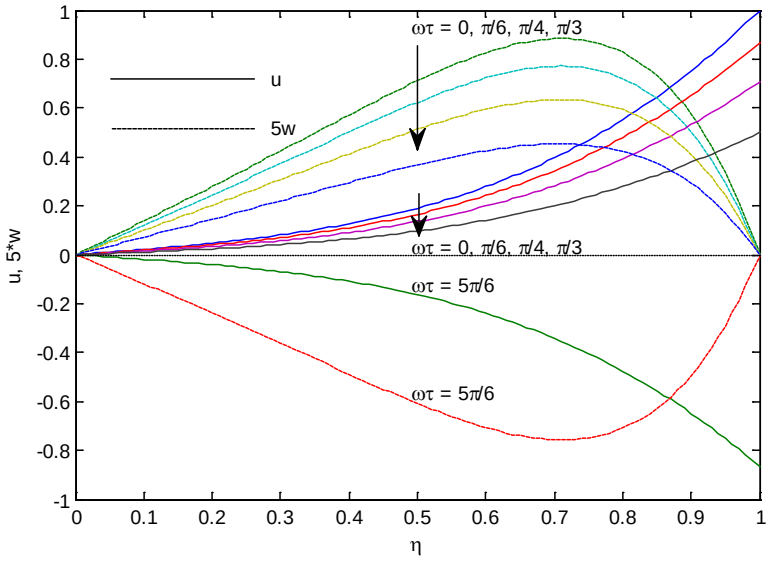

Figure 4. u and w for different values of $\omega\tau = 0, \frac{\pi}{6}, \frac{\pi}{4}, \frac{\pi}{3}$ and $\frac{5\pi}{6}$ with $M^2 = 10, K^2 = 5, \omega = 0.2$ and $\theta = \frac{\pi}{4}$.

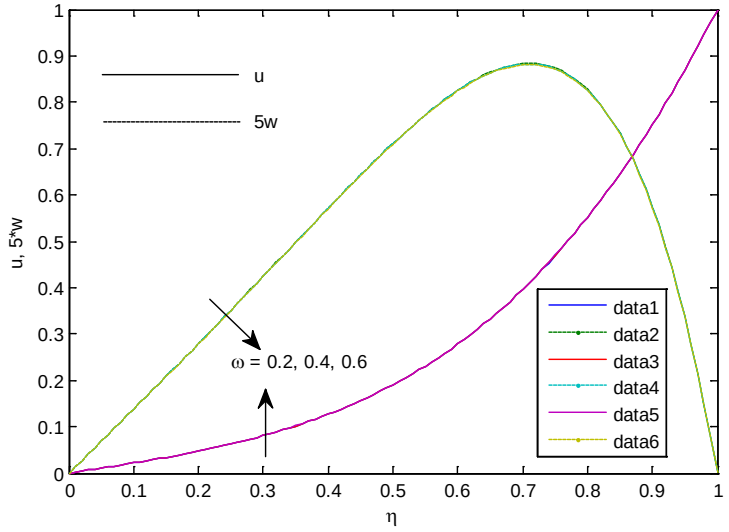

Figure 5. u and w for different values of $\omega = 0.2, 0.4$ and 0.6 with $M^2 = 10, K^2 = 5, \omega\tau = 0$ and $\theta = \frac{\pi}{4}$.

produce radiofrequency voltage with reference to $\nabla \cdot J \neq 0$ that emerges the backbone of a time varying electromagnetic field to exhibit X-emission in a vacuum. This situation reveals that magnetic pressure increases as the magnetic field grows towards the resonant level due to an irregular fluctuation of a magnetic field. In turn, in a time varying electromagnetic field, these arises fluctuation at every point on the flow field. **Figure 4** shows that the velocities due to main flow(u) and cross flow(w) decreases in the range $0 \le \omega\tau \le \frac{5\pi}{12}$ with

an increase in phase angle $\omega\tau$. Since frictional layer at the boundary is suddenly sets into motion so that air breaks down in a vacuum due to the absence of a pressure gradient. The flow field becomes relevant to the reduction of velocities in the main and cross flows. Although the MHD flow is subjected to a periodic driving force in the absence of a pressure gradient; irregular fluctuation of a velocity field builds up rapidly with a driving force when the phase angle $\omega\tau = \pi/2$. In a time varying electromagnetic field of a sinusoidal in nature subject to $\nabla \cdot J \neq 0$, the excitation frequency $\omega > \frac{1}{2}\cos\omega\tau\left(16K^4 - M^4\sin^4\theta\right)^{1/2}$ leads to resonance so that irregular fluctuation builds up rapidly with a driving force at large amplitude when $\omega\tau = \pi/2$. Since forcing wave excites natural frequency the phase angle $\omega\tau = \pi/2$ is compatible with $\omega > 0$. In such a situation, the phase angle $\omega\tau$ rotates with angular frequency ω, the time varying electromagnetic field determines a dynamo context of the Sun. It reveals that in a turbulent regime, a controlled thermonuclear fusion reaction of the Sun becomes significant over a large amplitude subject to a maximum dissipation of energy when the kinetic energy is transformed into heat. This situation implicates the theory of a supercritical state in the presence of a magnetic mirror at the resonant level so that maximum refection occurs with the growing of a magnetic field to exhibit laser radiation as the magnetic field increases in strength abruptly. Indeed an oscillator takes place of a driving force in the presence of a magnetic mirror is subjected to a laser radiation in a time varying electromagnetic field to exert its influence of resonance fluorescence when the phase angle $\omega\tau = \pi/2$. A synchronized photon light (laser pulse radiation) is transmitted from the Sun with radio wave propagation at shorter wave length. A physical occurrence communicates with the excitation frequency in such a way that irregular changes of galaxies inspired by the Sun due to a differential rotation of the system as the rotation of the Sun maintains a similar rotation of the Earth so that the Sun enters with different galaxies to change of its wave length. It is interesting for the readers that the solar system becomes a steady state in nature if the excitation frequency ω is switched off so that thermonuclear reaction of the Sun becomes stop. Eventually, the Sun is an exposure of an MHD in the presence of an inclined magnetic field in compliance with resonance subject to a dynamo context of the Sun. **Figure 5** demonstrates that the velocity (u) due to main flow increases with an increase in driving frequency ω whereas the velocity (w) due to cross flow decreases with an increase in driving frequency ω. In a time varying electromagnetic field of a sinusoidal character subject to $\nabla \cdot J \neq 0$, the MHD flow exerted by the driving force to increase the velocity (u) in a radiofrequency field to expedite radiofrequency voltage. In a velocity(w) due to cross flow attains to decrease the velocity to extract radiofrequency voltage in a usual manner as directed by the driving frequency ω.

An illustration takes place of a frictional shear stress to represent a physical interpretation on **Tables 1-4** with an arbitrary value of M^2, θ and $\omega\tau$. The

influence of a frictional shear stress plays a major role at the boundary of the solar region when the frictional layer at the boundary is suddenly sets into motion. Table 1 shows that the frictional shear stress in the main flow (u) direction increases in magnitude with the increase in magnetic pressure (M^2) while it decreases in magnitude with an increase in the angle of inclination (θ).

Table 1. Frictional shear stress at the moving boundary for $K^2 = 5, \omega = 0.2$ and $\omega\tau = 0$ due to main flow direction (u).

θ \ M^2	10	12	14	16	18
0	3.48092	3.72052	3.95283	4.17731	4.39396
π/6	3.13413	3.32258	3.50862	3.69093	3.86880
π/4	2.75359	2.88036	3.00984	3.14014	3.26997
π/3	2.32825	2.37645	2.43167	2.49213	2.55639
π/2	1.84083	1.77992	1.72484	1.67471	1.62881

Table 2. Frictional shear stress at the moving boundary for $K^2 = 5$, $\theta = \pi/4$ and $\omega = 0.2$ due to main flow direction (u).

$\omega\tau$ \ M^2	10	12	14	16	18
0	2.75359	2.88036	3.00984	3.14014	3.26997
π/6	2.36981	2.47957	2.59181	2.70483	2.81751
π/4	1.92561	2.01520	2.10688	2.19926	2.29139
π/3	1.34990	1.41319	1.47806	1.54350	1.60879

Table 3. Frictional shear stress at the moving boundary for $K^2 = 5$, $\omega = 0.2$ and $\omega\tau = 0$ due to cross flow direction (w).

θ \ M^2	10	12	14	16	18
0	−1.44135	−1.34654	−1.26628	−1.19759	−1.13816
π/6	−1.51182	−1.41843	−1.33823	−1.26878	−1.20814
π/4	−1.59681	−1.50722	−1.42879	−1.35979	−1.29872
π/3	−1.70268	−1.62177	−1.54924	−1.48399	−1.42509
π/2	−1.84046	−1.77956	−1.72449	−1.67437	−1.62848

Table 4. Frictional shear stress at the moving boundary for $K^2 = 5$, $\theta = \pi/4$, $\omega = 0.2$ due to cross flow direction (w).

$\omega\tau$ \ M^2	10	12	14	16	18
0	−1.59681	−1.50772	−1.42879	−1.35979	−1.29872
π/6	−1.38911	−1.31071	−1.24210	−1.18176	−1.12838
π/4	−1.13757	−1.07308	−1.01667	−0.96706	−0.92320
π/3	−1.80819	−0.76202	−0.72165	−0.68617	−0.65481

Since viscosity initiates thermal energy in a moving layer the internal energy is converted into a kinetic energy of the system; the magnetic pressure exerted by the main flow direction with reference to a driving frequency to increase viscous shear stress at the moving boundary. The effect of viscous shear stress at the moving layer decreases with increase in θ (angle of inclination of a magnetc field) for a fixed value of a magnetic pressure (M^2). This happens in the case of a viscous shear where the distortion of a magnetic lines force increase the velocity so that the frictional shear stress decreases at the moving boundary. Table 2 reveals that the frictional shear stress at moving layer due to main flow (u) direction increases in magnitude with an increase in magnetic pressure (M^2) for a fixed value of phase angle ($\omega\tau$) whereas it decreases in magnitude with an increase in phase angle ($\omega\tau$) for a fixed value of a magnetic pressure (M^2). Since phase angle rotates with angular frequency, the driving frequency accelerates the viscous shear at the moving layer to increase shear stress at the boundary whereas the viscous shear distabilizes at the moving layer in accordance with phase angle ($\omega\tau$). Table 3 indicates that the frictional shear stress at the moving boundary due to cross flow (w) direction decreases in magnitude with an increase in magnetic pressure (M^2) while it increases in magnitude with an increase in the angle of inclination of a magnetic field (θ). Since rotation induces cross flow, the velocity gradient at the moving boundary opposes the viscous stress to decrease in magnitude with an increase in magnetic pressure whereas the effect of velocity gradient leads to increase the frictional shear stress at the moving boundary in accordance with the angle of inclination of magnetic field (θ). Table 4 demonstrates that the frictional shear stress due to a cross flow (w) direction decreases in magnitude with an increase in either the magnetic pressure (M^2) or the phase angle ($\omega\tau$). It finds the situation in which the velocity gradient at the moving boundary opposes the effect of frictional shear stress in the cross flow (w) direction. Indeed, the effect of viscous shear stress provides a frictional resistance at the moving boundary to execute thermal resistance. Since the frictional layer at the boundary is suddenly sets into motion the internal energy is converted inton a kinetic energy of the system during convection process and the maximum dissipation of energy is liberated into smallest eddies with large amplitude when the kinetic energy is transformed into heat. This implies to a fact that the convective part of the surface of the Sun leads to a controlled thermonuclear fusion reaction in the presence of a magnetic mirror.

5. Conclusion

The purpose of present investigation is to deal with an MHD start up flow in a rotating environment with a decisive importance to a driving force in the presence of an inclined magnetic field by means of a traveling magnetic field. In a time varying electromagnetic field of a sinusoidal in nature subject to $\nabla \cdot J \neq 0$, the MHD flow is associated with a driving force in such a way that the emission of a hot electron is gyrating in a magnetic field to represent radio emission. Since

the MHD flow exerted by a driving force, the phase angle rotates with angular frequency to exerts its influence of an excitation frequency so that forcing wave excites natural frequency to implicate a resonance when the phase angle $\omega\tau = \pi/2$ as the phase angle $\omega\tau$ is compatible with $\omega > 0$. In turn, magnetic field grows towards the resonant level. Plasma fusion interacts with the supercritical state in the presence of a magnetic mirror with reference to a controlled thermonuclear fusion reaction of the Sun. An oscillator takes place of a driving force to execute plasma induced laser radiation in the presence of a magnetic mirror in which reflection occurs as the strength of the magnetic field increases in strength abruptly to exhibit resonance fluorescence when $\omega\tau = \pi/2$. This situation reveals that a synchronized photon light (laser pulse radiation) is emitted from the Sun.

Conflicts of Interest

The author declares no conflicts of interest regarding the publication of this paper.

References

[1] Ghosh, S.K. (2002) Effects of Hall Current on MHD Couette Flow in a Rotating Environment with Arbitrary Magnetic Field. *Czechoslovak Journal of Physics*, **52**, 51-63. https://doi.org/10.1023/A:1013913730086

[2] Guria, M., Jana, R.N. and Ghosh, S.K. (2006) Unsteady Couette Flow in a Rotating System. *The International Journal of Non-Linear Mechanics*, **41**, 838-843. https://doi.org/10.1016/j.ijnonlinmec.2006.04.010

[3] Pai, S.I. (1962) Magnetohydrodynamics and Plasma Dynamics. Springer-Verlag, Vienna. https://doi.org/10.1007/978-3-7091-8083-9

[4] Mondal, G., Mandal, K.K. and Choudhury, G. (1982) Hall Effects on MHD Plasma Couette Flow in a Rotating System. *Journal of the Physical Society of Japan*, **51** 382-389.

[5] Mondal, G. and Mandal, K.K. (1983) Effect of Hall Current on MHD Couette Flow between Thick Arbitrarily Conducting Plate in a Rotating System. *Journal of the Physical Society of Japan*, **52**, 470-477. https://doi.org/10.1143/JPSJ.52.470

[6] Katagiri, M. (1962) Flow Formation in Couette Motion in Magnetohydrodynamics. *Journal of the Physical Society of Japan*, **17**, 393-396. https://doi.org/10.1143/JPSJ.17.393

[7] Muhuri, P.K. (1963) Flow Formation in Couette Motion in Magnetohydrodynamics with Suction. *Journal of the Physical Society of Japan*, **18**, 1671-1675. https://doi.org/10.1143/JPSJ.18.1671

[8] Ghosh, S.K. and Pop, I. (2004) Hall Effect on MHD Plasma Couette Flow in a Rotating Environment. *International Journal of Applied Mechanics and Engineering*, **9**, 293-305.

[9] Ghosh, S.K. (1993) Unsteady Hydromagnetic Flow in a Rotating Channel with Oscillating Pressure Gradient. *Journal of the Physical Society of Japan*, **62**, 3893-3903. https://doi.org/10.1143/JPSJ.62.3893

[10] Sengupta, R. and Ray, T.K. (1990) Oscillatory Couette Flow of a Viscoelastic Electrically Conducting Fluid through a Porous Medium within a Parallel Plate Channel

in Presence of a Transverse Magnetic Field in a Rotating System. *Archieves of Mechanics*, **42**, 717-721.

[11] Singh, K.D. (2000) An Oscillatory Hydromagnetic Couette Flow in a Rotating System. *Zeitschrift fur Angewandte Mathematik und Mechanik* (*ZAMM*), **80**, 429-432. https://doi.org/10.1002/1521-4001(200006)80:6<429::AID-ZAMM429>3.0.CO;2-1

[12] Singh, K.D. and Sharma, R. (2001) MHD Three-Dimensional Couette Flow with Transpiration Cooling. *Zeitschrift fur Angewandte Mathematik und Mechanik* (*ZAMM*), **81**, 651-720.

[13] Ghosh, S.K. (2001) A Note on Unsteady Hydromagnetic Flow in a Rotating Channel Permeated by an Inclined Magnetic Field in the Presence of an Oscillator. *Czechoslovak Journal of Physics*, **51**, 799-804. https://doi.org/10.1023/A:1011622416362

[14] Ghosh, S.K., Beg, O.A., Zueco, J. and Prasad, V.R. (2010) Transient Hydromagnetic Flow in a Rotating Channel Permeated by an Inclined Magnetic Field with Magnetic Induction and Maxwell Displacement Current Effects. *Zeitschrift fur Angewandte Mathematik und Physik* (*ZAMP*) **61**, 147-169. https://doi.org/10.1007/s00033-009-0006-2

[15] Meyer, R.C. (1958) On Reducing Aerodynamic Heat Transfer Rates by Magnetohydrodynamic Techniques. *Journal of the Aerospace Sciences*, **25**, 561-566. https://doi.org/10.2514/8.7781

World Journal of Mechanics, 2018, 8, 378-386
http://www.scirp.org/journal/wjm
ISSN Online: 2160-0503
ISSN Print: 2160-049X

Theoretical Analysis and Experimental Verification of Crack Initiation Characteristics of Compression-Shear Plane Crack with Hydraulic Pressure

Yajuan Xie, Song Yu, Bangxiang Li, Ziyao Xu, Weishen Zhu

School of Civil Engineering, Shandong University, Jinan, China
Email: XXQ1715@163.com

How to cite this paper: Xie, Y.J., Yu, S., Li, B.X., Xu, Z.Y. and Zhu, W.S. (2018) Theoretical Analysis and Experimental Verification of Crack Initiation Characteristics of Compression-Shear Plane Crack with Hydraulic Pressure. *World Journal of Mechanics*, **8**, 378-386.
https://doi.org/10.4236/wjm.2018.89028

Received: August 30, 2018
Accepted: September 26, 2018
Published: September 29, 2018

Abstract

In this paper, the crack initiation characteristics of compression-shear plane crack with hydraulic pressure were studied by using theoretical analysis and experimental verification methods. The formula derivation process of stress intensity factor of crack tip and open-type crack initiation angle and initiation strength was expounded in detail. Cement mortar specimens prefabricated with open-type crack were made for biaxial compression test. The results show that the mode I stress intensity factor is inversely proportional to the dip angle of pre-exciting crack, water pressure and crack width. The fracture toughness is most easily achieved when the dip angle of pre-exciting crack is 60˚. The mode II stress intensity factor is symmetrically distributed with the dip angle and independent of the water pressure and crack width. For open-type crack, the crack initiation angle decreases with the increase of the dip angle of pre-exciting crack, water pressure and crack width; the crack initiation strength is inversely proportional to the water pressure and proportional to the lateral pressure. The research results can provide ideas for the study of crack initiation under the coupling of ground stress and osmotic pressure in tunnel engineering.

Keywords

Compression-Shear Plane Crack, Stress Intensity Factor, Experimental Verification, Crack Initiation Characteristics

1. Introduction

As we all know, there are a lot of fissures in the rock mass, and the existence of

fissures will reduce the mechanical properties of rock mass. In geotechnical engineering, the complex stress state of the coupling of ground stress and osmotic pressure promotes the expansion of the fissure, and the engineering failure caused by the crack expansion in rock is of common occurrence. In recent years, the crack initiation and expansion of the pre-existing fissure with hydraulic pressure has attracted the attention of researchers, and it is an important research direction and interesting in rock mechanics research. Liu S *et al.* [1] studied the fracture characteristics of fractured rock mass under different confining pressures and seepage water pressures based on Realistic Failure Process Analysis-Seepage. And derived the initial crack strength and the effect of seepage water pressure and confining pressure on the crack propagation of fractured rock mass. Kanaun [2] studied the evolution of the crack boundaries in the process of fluid injection, time dependence of pressure distributions and crack openings. Zhang D F *et al.* [3] took 2-D sidelong crack propagation as an example, giving out crack propagation steps by using the modified crack propagation criterion. Zhao Y L *et al.* [4] [5] have studied the crack initiation law of frictional crack under seepage pressure. They developed a damage fracture mechanics model of rock cracks under jointed action of compressive-shear stress field and seepage field. The evolution equations of additional stress intensity factor at the branch crack cusp were obtained considering rock bridge damage. And the mathematical model of seepage-fracture coupling of rock masses cracks propagation was established. XB LI *et al.* [6] studied the mechanical model of fracture and damage and the evolution equation of stress intensity factor at crack tip under the action of compression-shear field and seepage field, and proposed the crack initiation criterion by using the stress intensity factor.

In this paper, the crack initiation characteristics of pre-exciting plane crack with hydraulic pressure were studied. Based on the theoretical analysis, the variation of the stress intensity factor at the crack tip with the dip angle, water pressure and crack width was discussed. The variation of crack initiation angle with the dip angle of crack, water pressure and crack width was verified by experiment. And the variation of crack initiation strength with water pressure and lateral pressure was also verified.

2. Theoretical Analysis of the Initiation Characteristics of Pre-Exciting Plane Crack with Hydraulic Pressure

2.1. The Mode I Stress Intensity Factor (SIF) of Open-Type Crack

The compression-shear mixed crack model with hydraulic pressure is shown in Figure 1. σ_1 and σ_3 are far field compression stress and $\sigma_3 = \lambda\sigma_1$ $(0 \le \lambda \le 1)$; α is the angle between the crack and the σ_3 direction; p is the internal water pressure of the crack; the crack tip is reduced to two curvature radii of ρ semicircle; the crack length is $2a$ and θ is the crack initiation angle.

According to the fracture mechanics, stress concentration exists at crack tip. Before the crack closure, it is generally judged whether it is cracked by the

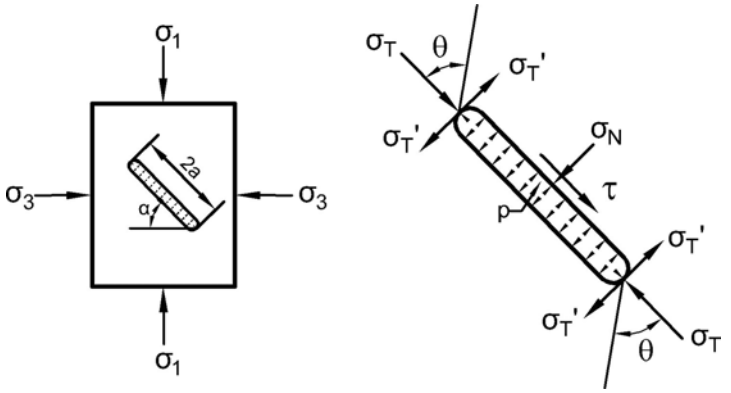

Figure 1. Model of open-type crack with seepage pressure.

stress distribution at the edge of the crack tip. The stress component of any section can be obtained by the unit body balance equation as the far field stress (σ_1, σ_3) is known [7].

Surface stress of crack surface:

$$\sigma_N = \frac{1}{2}\left[\left(\sigma_1+\sigma_3\right)+\left(\sigma_1-\sigma_3\right)\cos\left(2\alpha\right)\right]-p\,. \tag{1}$$

$$\sigma_T = \frac{1}{2}\left[\left(\sigma_1+\sigma_3\right)-\left(\sigma_1-\sigma_3\right)\cos\left(2\alpha\right)\right]-p\,. \tag{2}$$

$$\tau = \frac{1}{2}\left(\sigma_1-\sigma_3\right)\sin\left(2\alpha\right). \tag{3}$$

σ_N is the normal stress perpendicular to the crack surface; τ is the shear stress on the crack surface, and σ_T is the vertical direction stress at the crack tip. According to the fracture mechanics [8], the mode I stress intensity factor produced by the normal compression stress σ_N on the fissure surface is:

$$K_I^N = -\sigma_N\sqrt{\pi a} = -\left\{\frac{1}{2}\left[\left(\sigma_1+\sigma_3\right)+\left(\sigma_1-\sigma_3\right)\cos\left(2\alpha\right)\right]-p\right\}\sqrt{\pi a}\,. \tag{4}$$

σ_T has a tension effect on the edge of the crack, the maximum tensile stress appears in the crack tip and the size is equal to σ_T [9], as shown in **Figure 1**. Then the mode I stress intensity factor produced by the maximum tensile stress σ_T' at the crack tip is:

$$K_{\mathrm{I}}^T = \sigma_T\sqrt{\rho/a}\sqrt{\pi a} = \left\{\frac{1}{2}\left[\left(\sigma_1+\sigma_3\right)-\left(\sigma_1-\sigma_3\right)\cos\left(2\alpha\right)\right]-p\right\}\sqrt{\rho/a}\sqrt{\pi a}\,. \tag{5}$$

According to the superposition principle of linear elastic fracture mechanics, the mode I stress intensity factor of crack is: $K_{\mathrm{I}} = K_{\mathrm{I}}^T + K_{\mathrm{I}}^N$

It can be seen that the initiation and expansion of compression-shear mode I cracks depend on the normal stress of two vertical directions, the radius of curvature of crack tip and the circumference angle. The normal compressive stress σ_N inhibits the expansion of compression-shear fracture, and σ_T promotes the expansion. The seepage water pressure p has a promotion effect on the initiation and expansion of compression-shear fracture.

2.2. The Mode II Stress Intensity Factor of Open-Type Crack

The mode II fracture of I-II mixed mode crack under uniform shear stress is independent of the internal osmotic pressure of the crack. The analytic solution for the mode II crack stress intensity factor of composite crack is given [6]:

$$K_{\mathrm{II}} = -\tau\sqrt{\pi a} = -\frac{1}{2}\sqrt{\pi a}\left(\sigma_1 - \sigma_3\right)\sin\left(2\alpha\right). \tag{6}$$

2.3. Crack Initiation Characteristics with Hydraulic Pressure

2.3.1. Crack Initiation Angle of Open-Type Crack with Hydraulic Pressure

I-II type mixed mode fracture occurs under compression-shear condition. The maximum hoop stress theory is generally used in rock mechanics to study the crack initiation angle [10]. According to the fracture mechanics, the expression of stress component that only retains the singular term of crack tip in polar coordinate system is:

$$\begin{cases} \sigma_{rr} = \dfrac{1}{2\sqrt{2\pi r}}\left[K_{\mathrm{I}}(3-\cos\theta)\cdot\cos\dfrac{\theta}{2} + K_{\mathrm{II}}\left(3\cos\theta - 1\right)\cdot\sin\dfrac{\theta}{2}\right] \\ \sigma_{\theta\theta} = \dfrac{1}{2\sqrt{2\pi r}}\cos\dfrac{\theta}{2}\left[K_{\mathrm{I}}\left(1+\cos\theta\right) - 3K_{\mathrm{II}}\sin\theta\right] \\ \tau_{r\theta} = \dfrac{1}{2\sqrt{2\pi r}}\cos\dfrac{\theta}{2}\left[K_{\mathrm{I}}\sin\theta + K_{\mathrm{II}}\left(3\cos\theta - 1\right)\right] \end{cases} \tag{7}$$

The maximum hoop stress theory holds that the crack will initiate along the θ direction corresponding to the maximum value of $\sigma_{\theta\theta}$. According to the advanced mathematics, the maximum value of $\sigma_{\theta\theta}$ need satisfy the following conditions:

$$\partial\sigma_{\theta\theta}/\partial\theta = 0,\ \partial^2\sigma_{\theta\theta}/\partial^2\theta < 0. \tag{8}$$

By substitution of Equation (7) into Equation (8):

$$\begin{aligned} \frac{\partial\sigma_{\theta\theta}}{\partial\theta} &= -\frac{1}{\sqrt{2\pi r}}\cdot\frac{3}{2}\cos\frac{\theta}{2}\left[K_{\mathrm{I}}\sin\theta + K_{\mathrm{II}}\left(3\cos\theta - 1\right)\right] = 0 \\ \frac{\partial^2\sigma_{\theta\theta}}{\partial^2\theta} &= \frac{3}{8\sqrt{2\pi r}}K_{\mathrm{I}}\left(\sin\frac{\theta}{2}\sin\theta - 2\cos\frac{\theta}{2}\cos\theta\right) \\ &\quad + \frac{3}{8\sqrt{2\pi r}}K_{\mathrm{II}}\left(3\cos\theta + 6\cos\frac{\theta}{2}\sin\theta - 1\right) < 0 \end{aligned} \tag{9}$$

It can be obtained by formula (9) that $\cos\dfrac{\theta}{2} = 0$ or $K_{\mathrm{I}}\sin\theta + K_{\mathrm{II}}\left(3\cos\theta - 1\right) = 0$. If $\cos\dfrac{\theta}{2} = 0$, the solution is $\theta = \pm\pi$ which means that the cracking surface coincides with the original crack surface. That's meaningless. Therefore, the solution of crack initiation angle is the root of $K_{\mathrm{I}}\sin\theta + K_{\mathrm{II}}\left(3\cos\theta - 1\right) = 0$.

2.3.2. Crack Initiation Strength of Open-Type Crack with Hydraulic Pressure

In this paper, the following compress shear fracture criterion of rock, which is

proposed in the literature [11] [12] [13], is used to study the I-II type mixed mode crack initiation strength under compression-shear condition.

$$\lambda_{12}K_{\mathrm{I}}+\left|K_{\mathrm{II}}\right|=\bar{K}_{\mathrm{IIC}}. \tag{10}$$

λ_{12} is the compression-shear coefficient, which is related to the material properties. $\bar{K}_{\mathrm{IIC}}$ is the shear fracture toughness under compression.

The initiation strength of open-type crack with hydraulic pressure is obtained by substituting the Equations ((4)-(6) into (10)) [6]:

$$\sigma_1'=\frac{2\bar{K}_{\mathrm{IIC}}/\sqrt{\pi a}+A\sigma_3-2p\lambda_{12}\left(1-\sqrt{\rho/a}\right)}{B}$$

$$A=\sin(2\alpha)+\lambda_{12}\left[1-\sqrt{\rho/a}-\left(1+\sqrt{\rho/a}\right)\cos(2\alpha)\right]$$

$$B=\sin(2\alpha)-\lambda_{12}\left[1-\sqrt{\rho/a}+\left(1+\sqrt{\rho/a}\right)\cos(2\alpha)\right]$$

3. Comparative Analysis of Experimental and Theoretical Results of Compression-Shear Plane Crack Initiation and Expansion with Hydraulic Pressure

The cement mortar specimens prefabricated with open-type through crack were fabricated. Specimen width $2b$ = 70 mm, height $2h$ = 140 mm, thickness $2t$ = 40 mm. There is an oblique crack with a length of $2a$ = 12 mm in the middle of the specimen. Material parameter e = 22.09 gpa, υ = 0.142, internal friction angle $\varphi=50^{\circ}$. The compression-shear fracture parameters of the material have been measured by the method presented in the literature [12].

$K_{\mathrm{IIC}}=0.582\ \mathrm{MPa}\cdot\mathrm{m}^{1/2}$, $\lambda_{12}=0.92$. In the experiment, the crack is sealed by clamping the seal ring and the tempered glass with a clamp.

3.1. Effect of the Dip Angle of Pre-Exciting Crack on Stress Intensity Factor and Crack Initiation Angle

In the experiment, the vertical pressure, lateral pressure, water pressure and crack thickness were controlled as follows: $\sigma_1=20$ MPa, $\sigma_3=0$ MPa, $p=1$ MPa, $\rho=1.5$ mm. The dip angle of pre-exciting crack was changed and set the dip angle to 15˚, 30˚, 45˚, 60˚, 75˚. The analytical solution of stress intensity factor and crack initiation angle was calculated by substituting the experimental parameters into the above derivation formulas. The results are as follows (**Table 1**).

It is intuitive to see the variation of the stress intensity factor and the crack initiation angle with the dip angle of pre-exciting crack. The mode I stress intensity factor decreases with the increase of the dip angle, and the minimum value is obtained when the dip angle is 60 degrees. The mode II stress intensity factor is symmetrically distributed with the dip angle of pre-exciting crack, and the maximum value is obtained when the dip angle is 45 degrees.

As shown in **Figure 2**, it was observed in the experiment that the crack initiation angle decreases with the increase of the dip angle of pre-exciting crack which is consistent with the theoretical derivation.

3.2. Effect of Water Pressure on Stress Intensity Factor and Crack Initiation Angle

In the experiment, the dip angle of pre-exciting crack was controlled to $\beta = 45^{\circ}$. The water pressure was changed and set the water pressure to 0 MPa, 0.5 MPa, 1 MPa. The analytical solution of stress intensity factor and crack initiation angle was calculated by substituting the experimental parameters into the above derivation formulas. The results are as follows:

It can be seen from the table (Table 2) that the mode I stress intensity factor decreases with the increase of water pressure. And mode II stress intensity factor is independent of water pressure. The crack initiation angle decreases with the increase of water pressure.

Table 1. The results of SIF and initial angle with different pre-exciting crack dip angles.

The calculation results	Different dip angles of pre-exciting crack(˚)				
	15	30	45	60	75
τ	5	8.66	10	8.66	5
σ_N	17.66	14	9	4	0.34
σ_T	0.34	4	9	14	17.66
K_{I}	−2.40	−1.65	−0.62	0.41	1.17
K_{II}	−0.69	−1.19	−1.37	−1.19	−0.69
θ	126.6	97.2	79.3	64.1	43.7

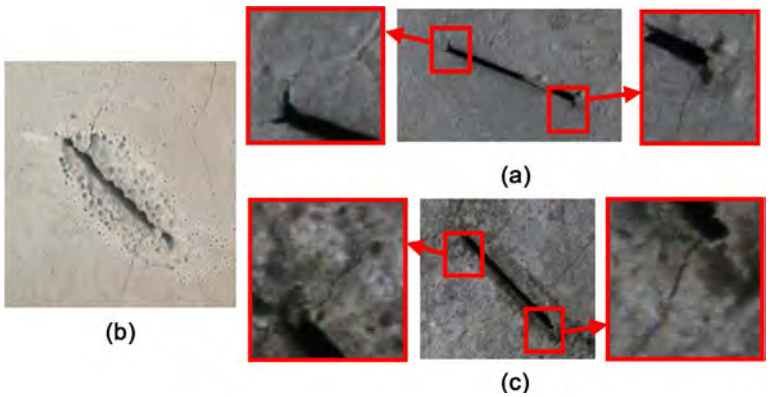

Figure 2. Crack initiation with different pre-exciting crack dip angle. Crack initiation at the dip angle of 30˚; Crack initiation at the dip angle of 45˚; Crack initiation at the dip angle of 60˚.

Table 2. The results of SIF and initial angle with different seepage pressure.

The calculation results	Different seepage pressure(MPa)		
	0	0.5	1
K_{I}	−0.69	−0.65	−0.62
K_{II}	−1.37	−1.37	−1.37
θ	80.34	79.77	79.33

3.3. Effect of Crack Width s on Stress Intensity Factor and Crack Initiation Angle

In the experiment, the dip angle of pre-exciting crack and water pressure were controlled as follows: The crack width was changed and set the crack width to 1 mm, 1.5 mm, and 2 mm. The analytical solution of stress intensity factor and crack initiation angle was calculated by substituting the experimental parameters into the above derivation formulas. The results are as follows:

It can be seen from the table (Table 3) that the mode I stress intensity factor decreases with the increase of crack width. And mode II stress intensity factor is independent of crack width. The crack initiation angle decreases with the increase of crack width.

3.4. The Experimental Verification of Pre-Exciting Plane Crack Initiation Strength with Hydraulic Pressure

In the experiment, the crack initiation strength was recorded when the lateral pressure was controlled to $\sigma_3 = 0$ MPa and set the water pressure to $p = 0$ MPa, 0.5 MPa and 1 MPa; the crack initiation strength was also recorded when the water pressure was controlled to $p = 0$ MPa and set the lateral pressure to $\sigma_3 = 0\text{ MPa}, 1\text{ MPa}, 5\text{ MPa}, 10\text{ MPa}$.

The analytical solution of crack initiation strength was calculated by substituting the experimental parameters into the above derivation formulas. By comparing the analytical values with the experimental values, we can see the variation of crack initiation strength with the water pressure and lateral pressure. The results are as follows:

It can be seen from the tables (Table 4 and Table 5) that the crack initiation

Table 3. The results of SIF and initial angle with different crack widths.

The calculation results	Different crack widths (mm)		
	1	1.5	2
K_{I}	−0.73	−0.62	−0.52
K_{II}	−1.37	−1.37	−1.37
θ	80.91	79.33	77.89

Table 4. Crack initiation strength with different seepage pressure.

The values of crack initiation strength	Different seepage pressure (MPa)		
	0	0.5	1
Analytical values	−0.69	−0.65	−0.62
Experimental values	−1.37	−1.37	−1.37

Table 5. Crack initiation strength with different lateral pressure.

The values of crack initiation strength	Different lateral pressure (MPa)			
	0	1	5	10
Analytical values	14.0	16.7	27.51	41.03
Experimental values	15.3	17.0	29.0	42.2

strength decreases with the increase of water pressure and increases with the increase of lateral pressure. The experimental results were consistent with the theoretical results.

4. Conclusions

In this paper, the stress intensity factor (SIF), crack initiation angle and crack initiation strength of open-type crack with hydraulic pressure were derived. The variation of the stress intensity factor at the crack tip with the dip angle, water pressure and crack width was discussed. The crack initiation strength formula of compression-shear open-type crack with hydraulic pressure was verified by comparing the experimental and theoretical results.

The following conclusions are got:

1) For the stress intensity factor of pre-exciting open-type crack with hydraulic pressure, the mode I stress intensity factor decreases with the increase of pre-exciting crack dip angle, and the minimum value is obtained when the dip angle is 60 degrees, which means that the fracture toughness is most easily achieved when the dip angle is 60˚. The water pressure and crack width are inversely proportional to mode I stress intensity factor and promote the expansion of pre-exciting crack. The mode II stress intensity factor is symmetrically distributed with pre-exciting crack dip angle, and the maximum value is obtained when the dip angle is 45˚. The mode II stress intensity factor is independent of the water pressure and the crack width.

2) For the crack initiation angle of pre-exciting open-type cracks with hydraulic pressure, it is proportional to pre-exciting crack dip angle, water pressure and crack width. The theoretical derivation of the variation of the crack initiation angle is consistent with the trend of crack initiation angle was observed during the experiment.

3) The relationship between crack initiation strength and water pressure and lateral pressure was discussed. The crack initiation strength is inversely proportional to the water pressure and proportional to the lateral pressure.

Acknowledgements

We thank Prof. YU for his great help. This paper is supported by the National Natural Science Foundation Project (51579140).

Conflicts of Interest

The authors declare no conflicts of interest regarding the publication of this paper.

References

[1] Liu, S., Li, W., Wang, Q., *et al.* (2017) Numerical Simulation on Crack Propagation of Rock Mass with a Single Crack under Seepage Water Pressure. *Advances in Mechanical Engineering*, **9**, 10. https://doi.org/10.1177/1687814017732896

[2] Kanaun, S. (2017) Hydraulic Fracture Crack Propagation in an Elastic Medium with Varying Fracture Toughness. *International Journal of Engineering Science*, **120**, 15-30. https://doi.org/10.1016/j.ijengsci.2017.06.009

[3] Zhang, D.F. and Li, S.-C. (2009) The Modified Tensile Stress Crack Propagation Criterion and Influence of Cranny Hydraulic Pressure on Crack Propagation. *Chinese Journal of Computational Mechanics*, **26**, 114-119.

[4] Zhao, Y.L., Cao, P., Wen, Y.D., *et al.* (2008) Damage Fracture Failure Mechanism of Compressive-Shear Rock Cracks under Seepage Pressure. *Journal of Central South University*, **39**, 838-844.

[5] Zhao, Y.L., Peng, Q.Y., Wen, W., *et al.* (2014) Seepage-Fracture Coupling Mechanism of Rock Masses Cracking Propagation under High Hydraulic Pressure and Numerical Verification. *Rock & Soil Mechanics*, **35**, 556-564.

[6] Li, X.B., He, X.Q. and Chen, H.J. (2012) Study on Crack Initiation Behavior of Rock-Like Materials under Permeation Hydraulic Pressure. *Chinese Journal of Rock Mechanics and Engineering*, **31**, 1317-1324.

[7] Gere, J.M. and Timoshenko, S.P. (1997) Mechanics of Material. PWS Press, Boston.

[8] Whittaker, B.N., Singh, R.N. and Sun, G. (1992) Rock Fracture Mechanics Principles, Design and Applications. Elsevier, Amsterdam.

[9] Muskhelishvili, N.I. (1953) Some Basic Problems of the Mathematical Theory of Elasticity. *Mathematical Gazette*, **48**, 351.

[10] Erdogan, F. and Sih, G.C. (1963) On the Crack Extension in Plates under Plane Loading and Transverse Shear. *Journal of Basic Engineering*, **85**, 527. https://doi.org/10.1115/1.3656899

[11] Zhou, Q.L. and Liu, G.F. (1982) Compressive Shear Fracture of Brittle Material. *Journal of Hydraulic Engineering*, **1982**, 65-71.

[12] Zhou, Q.L. (1979) Discussion on the Calculation of Concrete Gravity Dam and Bedding Cementing Surface by Fracture Mechanics Method. *Hydrogeology and Engineering Geology*, **1979**, 27-37.

[13] Zhou, Q.L. (1987) Compress Shear Fracture Criterion of Rock and Its Application. *Chinese Journal of Geotechnical Engineering*, **9**, 33-37.

Scientific Research Publishing

World Journal of Mechanics, 2018, 8, 387-415
http://www.scirp.org/journal/wjm
ISSN Online: 2160-0503
ISSN Print: 2160-049X

Delusions in Theoretical Hydrodynamics

Alexander Ivanchin

Orpheus Ltd, Tomsk, Russia
Email: al.g.ivanchin@gmail.com

How to cite this paper: Ivanchin, A. (2018) Delusions in Theoretical Hydrodynamics. *World Journal of Mechanics*, **8**, 387-415.
https://doi.org/10.4236/wjm.2018.89029

Received: August 27, 2018
Accepted: September 26, 2018
Published: September 29, 2018

Abstract

Theoretical hydrodynamics may lead one into serious delusions. This article is focused on three of them. First, using flowing around a sphere as an example it is shown that the known potential solutions of the flow-around problems are not unique and there exist nonpotential solutions. A nonpotential solution has been obtained for flowing around a sphere. A general solution of the problem of flowing around an arbitrary surface has been obtained in the quadrature form. To single out a physically realisable solution among a great number of others, it is necessary to add supplementary conditions to the known boundary ones, in particular, to find a solution with the minimum total energy. The hypothesis explaining the reason for stalled flows by viscosity is erroneous. When considering a flow-around problem one should use stalled and broken solutions of the continuity equation along with the continuous ones. If the minimum total energy is achieved by the continuous solution, it is a continuous flow that will be implemented. If it is achieved by the broken solution, a stalled flow will be realised. Second, the hydrodynamics of a flow is considered exclusively at each point of it. Differential equations are used to describe the flows that are written for a randomly small volume of a flow, *i.e.*, for a point. The integral characteristics of a flow and its inertial properties are neglected in the consideration, which results in the misunderstanding of the mechanism of the formation of a vortex. The reason for the formation of vortices is related to viscosity, which is a mistake. The formation of vortices is the result of the inhomogeneity of the acceleration field and the inertial properties of a flow. Third, the fictitious values of viscous stresses are used in hydrodynamics. As a matter of fact, viscosity is the momentum diffusion and it should be described by the diffusion equation included into the Euler system of equations for a viscous fluid. The momentum diffusion leads to the necessity of including the volume momentum sources produced by diffusion into the continuity equation and excluding the viscosity forces from the equation of motion. The problem of a viscous fluid flowing around a thin plate has been solved analytically, the velocity profiles satisfying the experiment have been obtained. The superfluidity of helium is not its property. It is

the interaction of helium with a streamlined surface that is responsible for the mechanism of superfluidity. At low temperatures when the quantum properties are most pronounced the momentum transfer from the helium atoms to the streamlined wall becomes impossible, since the value of the energy transferred in the collision of a helium atom with that of the wall is smaller than the permitted quantum of energy. This mechanism takes place in the case of a flow in capillaries. Under a hydrodynamic flow-around superfluidity does not manifest due to the occurrence of stalled flows. The hypothesis of the disappearance of the viscous stresses at low temperatures is erroneous. The viscous stresses cannot disappear since they do not exist in nature. The theory of representing superfluidity as a phase transition accompanied by the formation of the combined viscous and nonviscous phases is a mistake.

Keywords

Nonpotential Flow Around, Nonuniqueness of Flow around a Sphere, Flow around Arbitrary Bodies, Eddy Formation, Viscous Flow, Diffusion and Viscosity, Viscous Flow along a Plate

1. Introduction

In theoretical hydrodynamics there exist serious delusions, both mathematical and physical ones, which lead to erroneous conclusions and misunderstanding in the physics of the flow.

The Euler system of the differential equations of the mechanics of fluid consists of the continuity equation, the momentum-conservation equation or the so-called equation of motion, the energy equation and that of thermodynamic relations [1]. At present the continuity equation is the starting one for steady-state flows. When solving it one derives the field of velocities to define the pressure from the equation of motion.

It is considered that if the potential solution of the continuity equation is found, which is thought to be unique without proof, then the problem has been solved. This is a delusion. In addition to the potential solution, the continuity equation has some nonpotential solutions, which leads to a revision of the knowledge about the physics of the flow of fluids. To obtain a physically realizable solution, it is necessary to add supplementary conditions, e.g. the minimum energy condition, to the boundary and initial ones that are used at present. Other variants are also possible.

The second delusion is that only differential characteristics of a flow are taken into account, the conservation laws are written for a point, whereas the integral characteristics, such as the moment of inertia, are ignored. As a result, the mechanism of the formation of vortices is ignored in the consideration.

The third delusion is the mechanism of viscosity. It is believed that under a viscous flow there appear shear stresses. This theory, in spite of its rather long

history of development, encounters insuperable difficulties in the solution of simple problems, e.g. calculation of a flow near the tip of a flat plate. The reason for this is the wrong, in the physical sense, statement of the problem. From the point of view of molecular physics, there are no viscous shear stresses. It is especially evident in the case of a gas.

The non-uniqueness of the solution of the problem of flow about of a contour is considered in Section 2 and obtain its general solution in quadrature form. Section 3 deals with the formation of vortices in stalled flow. In Section 4, viscosity is considered from the position of momentum diffusion.

2. Flowing around a Sphere

The convolution of two functions [2] $f_1(x,y,z)$ and $f_2(x,y,z)$ is denoted by $*$ and determined in this way

$$f_1 \overset{S}{*} f_2 = \iint\limits_{x_1,y_1,z_1 \in S} f_1(x_1,y_1,z_1)\, f_2(x-x_1, y-y_1, z-z_1)\,\mathrm{d}x_1\mathrm{d}y_1\mathrm{d}z_1 \tag{1}$$

The symbol S above the sign of convolution $*$ stands for a set with respect to which integration is performed. Let $z = Z(x,y)$ be the equation of the surface S, then (1) looks like

$$f_1 \overset{S}{*} f_2 = \iint\limits_{x_1,y_1 \in S} f_1(x_1,y_1,Z(x_1,y_1))\, f_2(x-x_1, y-y_1, z-Z(x_1,y_1))\,\mathrm{d}x_1\mathrm{d}y_1 \tag{2}$$

Continuity equation. The continuity equation for a steady-state flow is written as [1]

$$\nabla \mathrm{I} = q(\mathrm{r}) \tag{3}$$

Here I is the vector of the momentum density at a point in the flow,

$$\mathrm{I} = \rho \mathrm{V} \tag{4}$$

V is the velocity at this point, ρ is the fluid density, $q(\mathrm{r})$ is the power of the momentum density sources, $\mathrm{r} = \{x,y,z\}$ is the radius-vector, $r = \sqrt{x^2+y^2+z^2}$ is its length. The nabla

$$\nabla = \left\{ \frac{\partial}{\partial x}, \frac{\partial}{\partial y}, \frac{\partial}{\partial z} \right\} \tag{5}$$

is the differential gradient operator. The vector is denoted by the bold type, its modulus by the usual one.

If the medium is noncompressible, $\rho = \mathrm{const}$, then the continuity Equation (3) is written as [1]

$$\nabla \mathrm{V} = \frac{q(\mathrm{r})}{\rho} \tag{6}$$

The Equations ((3) and (6)), in fact, coincide, with only the right side differing by the presence of the constant coefficient, which for linear equations is not essential.

For a compressible gas it is necessary to use thermodynamic relations. The

dependence between the density ρ and the pressure p for the adiabatic process is as follows [3]

$$\frac{p}{p_0}=\left(\frac{\rho}{\rho_0}\right)^k \tag{7}$$

The enthalpy for the adiabatic process is written as

$$H=\frac{k}{k-1}\frac{p_0}{\rho_0}\left[\left(\frac{p}{p_0}\right)^{\frac{k-1}{k}}-1\right] \tag{8}$$

Here c_p, c_v are the thermal capacities at a constant pressure and a constant volume, $k=c_p/c_v$.

The Bernoulli potential is

$$B=H+\frac{I^2}{2\rho}=\frac{k}{k-1}\frac{p_0}{\rho_0}\left[\left(\frac{p}{p_0}\right)^{\frac{k-1}{k}}-1\right]+\frac{I^2}{2\rho_0}\left(\frac{p_0}{p}\right)^{\frac{1}{k}} \tag{9}$$

Having derived the momentum by (3) it is possible to define the velocity field from (9).

Equation of motion. The equation of motion of a fluid when no volume forces or viscosity exist is the following [1]

$$\frac{\partial I_i}{\partial t}+\frac{I_j}{\rho}\frac{\partial I_i}{\partial x_j}=-\frac{1}{\rho}\frac{\partial p}{\partial x_i} \tag{10}$$

Summation is made with respect to the recurrent indices from 1 to 3. Otherwise (10) is written as

$$\nabla\left(\frac{V^2}{2}\right)+(\nabla\times\mathrm{V})\times\mathrm{V}=\nabla\left(\frac{V^2}{2}\right)+\boldsymbol{\Omega}\times\mathrm{V}=-\frac{1}{\rho}\nabla p \tag{11}$$

Here the symbol $\nabla\times$ stands for the differential rotor operation,

$$\boldsymbol{\Omega}=\nabla\times\mathrm{V} \tag{12}$$

is the angular velocity. The value of

$$\rho\boldsymbol{\Omega}\times\mathrm{V} \tag{13}$$

is the density of the Coriolis force. It is worth noting that the Coriolis force is a force rather than the moment of force, it cannot induce the rotation of a fluid. In the general case, according to (11), the velocity is a nonpotential vector. The pressure is a potential, since the force produced by it is the gradient of the pressure.

For an incompressible fluid (11) is written as

$$\nabla\left(\frac{V^2}{2}+\frac{p}{\rho}\right)+\boldsymbol{\Omega}\times\mathrm{V}=0 \tag{14}$$

For the potential field $\mathrm{V}=\nabla\Psi$, where Ψ is the velocity potential, then

$$\boldsymbol{\Omega}=\nabla\times\mathrm{V}=\nabla\times\nabla\Psi\equiv 0 \tag{15}$$

and from (14) it is possible to derive the Bernoulli relation

$$\frac{\rho V^2}{2} - \frac{\rho V_0^2}{2} = -(p - p_0) \tag{16}$$

The lower index 0 denotes the parameters whose value is known at some point of the flow. It should be noted that (16) is true only for the potential fields of the momentum and an incompressible fluid.

There are two ways of mathematical description of the motion of a fluid. In the Langrange method an elementary particle of the mass is taken and the equation of motion is written for it. Its coordinates are varied in time.

In the Euler method, it is not a material particle that is taken but a fixed volume with a fluid flowing through its surface, and the balance of the forces is considered in this volume. Using the Langrange method it is very simple to show the difference between the potential and nonpotential flow. For the arbitrary element of the mass, according to (12), the angular velocity (15) of its motion in the potential flow is zero, it does not rotate and keeps its orientation even when following a curved trajectory as shown in Figure 1. In the nonpotential flow the angular velocity (12) is not zero and the element of the mass changes its orientation during motion as shown in Figure 2.

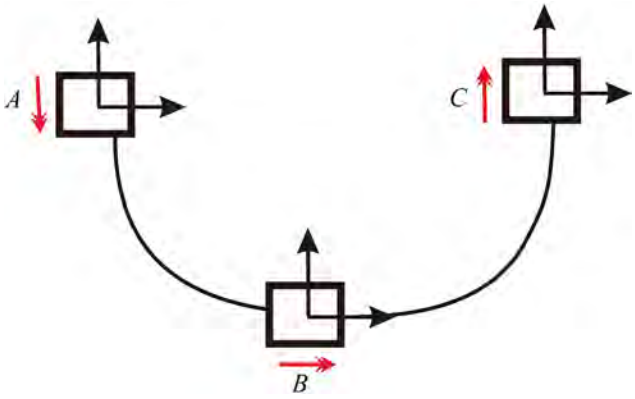

Figure 1. Potential flow. The material particles keep their orientation at points *A*, *B*, *C* in spite of the fact that the direction of the motion shown by the red arrows changes by 180˚.

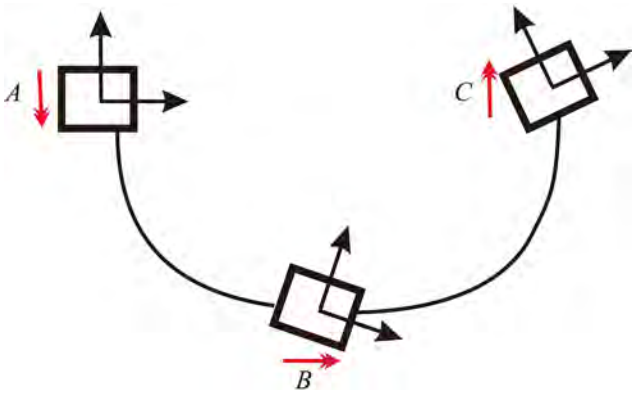

Figure 2. Nonpotential flow. The material particles turn changing their orientation in the flow at points *A*, *B*, *C*. The red arrows show the direction of the motion of the particles.

2.1. A Point Source

The point source is assigned as

$$q(\mathrm{r}) = \mu\delta(\mathrm{r}) \tag{17}$$

Here μ is the power of the momentum source. The Equation (3) is written as

$$\nabla \cdot \mathrm{I} = \mu\delta(\mathrm{r}) \tag{18}$$

As shown in [4] this equation has two solutions. The first is the well-known potential one

$$\mathrm{I} = \nabla\Phi = \frac{\mu}{4\pi}\frac{\mathrm{r}}{r^3} = \frac{\mu}{4\pi}\left\langle \frac{1}{r^2}, 0, 0 \right\rangle \tag{19}$$

In the present article the Cartesian components are written in the braces. The broken brackets denote that the vector is written in the spherical coordinates with the following sequence of the components: the radial r, the zenith ϑ, the azimuth φ. Substituting $\nabla\Phi$ from (19) into (18) one derives the Poisson differential equation for the potential Φ:

$$\Delta\Phi = \frac{\mu}{4\pi}\delta(r) \tag{20}$$

The solution (20) called a potential is

$$\Phi(r) = -\frac{\mu}{4\pi r} = -\frac{\mu}{4\pi\sqrt{x^2 + y^2 + z^2}} \tag{21}$$

It is the fundamental solution of the Poisson equation.

The vector (19) is the fundamental solution of the Equation (18). The potential vector field produced by the sources $\mathrm{q}(\mathrm{r})$ will be the convolution of (19)

$$q_i(\mathrm{r}) * \mathrm{I} = q_i(\mathrm{r}) * \frac{\mu}{4\pi}\frac{\mathrm{r}}{r^3} \tag{22}$$

The convolution of (22) is performed component by component.

The flow of the vector I through a closed sphere with the center at the origin of coordinates is

$$\int_0^{2\varphi} \mathrm{d}\varphi \int_0^{\pi} I_r r^2 \sin\vartheta \mathrm{d}\varphi = \mu \tag{23}$$

It does not depend on the radius of the integration sphere.

As shown in [4], the solution (19) is not unique. There is a vector called neutron

$$\mathrm{N} = \xi\frac{2z^2 - x^2 - y^2}{r^2}\frac{\mathrm{r}}{r^3} = \frac{\xi}{2r^2}\langle 1 + 3\cos 2\vartheta, 0, 0\rangle \tag{24}$$

such that the vector

$$\mathrm{I} + \mathrm{N} = \frac{\mu}{4\pi}\frac{\mathrm{r}}{r^3} + \xi\frac{2z^2 - x^2 - y^2}{r^2}\frac{\mathrm{r}}{r^3} = \frac{\mu}{4\pi r^2}\langle 1, 0, 0\rangle + \frac{\xi}{2r^2}\langle 1 + 3\cos 2\vartheta, 0, 0\rangle \tag{25}$$

is the solution of (18), which is checked by the substitution of (25) into (18). Here ξ is an arbitrary number, by the terminology [4]—a neutron charge. The vector (25) is nonpotential. The flow N through the sphere with the centre at the origin of the coordinates is

$$\int_0^{2\varphi} \mathrm{d}\varphi \int_0^{\pi} N_r r^2 \sin\vartheta \mathrm{d}\varphi = 0 \tag{26}$$

The addition of N to I does not affect the flow value. At $r \to \infty$ both solutions (19), (24) decrease as $1/r^2$.

The vector (25) is the fundamental solution of nonpotential flows. For the sources $\mathrm{q}(\mathrm{r})$ the field of velocities produced by them will be the convolution

$$q_i(\mathrm{r}) * (\mathrm{I} + \mathrm{N}) \tag{27}$$

similar to (22).

Delta-function. The general form of the δ-function is [2]

$$\delta = \sum_{n=0}^{\infty} \delta^{(n)} \tag{28}$$

Here $\delta^{(n)}$ is the derivative of order n of the δ-function, it is presented as

$$\delta^{(n)} = \sum_{m_x, m_y, m_z}^{m_x+m_y+m_z=n} \lambda_{m_x m_y m_z} \frac{\partial^n \delta}{\partial x^{m_x} \partial y^{m_y} \partial z^{m_z}} \tag{29}$$

Here $\lambda_{m_x m_y m_z}$ are the arbitrary constants, the nth derivative of the δ-function is the linear combination of all its mixed derivatives of the order n.

The presentation of the δ-function in the form (28) should be taken into account in the solution of the Equation (18). A complete solution is obtained by the addition of the linear combination of all derivatives of (25) to the solution (25). The vector (25) tends to zero as $1/r^2$ at $r \to \infty$, its first derivative as $1/r^3$ and so on.

The derivative δ-function of order n is a multipole of order n. Inclusion into the consideration of the nth derivatives in (28) means the addition of the multipoles of the nth order to the solution (25).

The potential source dipole. The homogeneous flow with a constant momentum density oriented parallel to the z-axis and directed from $+\infty$ to $-\infty$ is written as

$$\mathrm{w} = -\{0, 0, w\} = \langle -w\cos\vartheta, w\sin\vartheta, 0 \rangle \tag{30}$$

The field of the dipole source with the z-axis as the axis of symmetry is obtained by differentiating (19) with respect to z and the replacement of μ by the dipole moment $\dot{\mu}$

$$\dot{\mathrm{I}} = \frac{\partial \mathrm{I}}{\partial z} = \frac{\dot{\mu}}{4\pi r^5} \{3xz, 3yz, 2z^2 - x^2 - y^2\} = \frac{\dot{\mu}}{4\pi r^3} \langle 2\cos\vartheta, \sin\vartheta, 0 \rangle \tag{31}$$

The dipoles and their moments are designated by one upper point and the quadrupoles by two points.

Adding (30) and (31) and equating the radial component of the sum to zero at

$r = R$ one derives the known relation [1]

$$\dot{\mu} = 2\pi w R^3 \tag{32}$$

As a result one obtains the potential velocity field in flowing around a sphere

$$\mathrm{w} + \dot{\mathrm{I}} = w\left\langle \left(\frac{R^3}{r^3} - 1\right)\cos\vartheta, \left(1 + \frac{R^3}{2r^3}\right)\sin\vartheta, 0 \right\rangle \tag{33}$$

The neutron vector dipole. The neutron vector dipole (24) with the *z*-axis as the axis of symmetry is written in the spherical coordinates as

$$\dot{\mathrm{N}} = \frac{\partial \mathrm{N}}{\partial z} = \frac{\dot{\xi}}{r^3}\left\langle -8\cos\vartheta\left(3\cos 2\vartheta - 1\right), \sin\vartheta - 3\sin 3\vartheta, 0\right\rangle \tag{34}$$

The quadrupole potential source. Differentiating with respect to z (31) one derives the potential component quadrupole in the form

$$\begin{aligned} \ddot{\mathrm{I}} &= -\frac{3\ddot{\mu}}{4\pi r^7}\left\{x\left(x^2 + y^2 - 4z^2\right), y\left(x^2 + y^2 - 4z^2\right), z\left(3x_2 + 3y_2 - 2z^2\right)\right\} \\ &= \frac{\ddot{\mu}}{r^4}\left\langle 1 + 3\cos 2\vartheta, 2\sin 2\vartheta, 0\right\rangle \end{aligned} \tag{35}$$

Here $\ddot{\mu}$ is the source quadrupole moment. The vector flow (35) through a sphere is

$$\int_0^{2\varphi} \mathrm{d}\varphi \int_0^{\pi} \ddot{I}_r r^2 \sin\vartheta \mathrm{d}\varphi = 0 \tag{36}$$

The sum of the radial components (24) and (35) on the sphere is

$$N_r + \ddot{I}_r = \left(\xi + \frac{2\ddot{\mu}}{R^2}\right)\frac{1 + 3\cos 2\vartheta}{2R^2} = 0 \tag{37}$$

at

$$\frac{2\ddot{\mu}}{R^2} = -\xi \tag{38}$$

which taking into account (26) and (36) means that the vector

$$\mathrm{w} + \dot{\mathrm{I}} + \lambda_1\left(\mathrm{N} + \ddot{\mathrm{I}}\right) \tag{39}$$

is the solution of the continuity Equation (18) at the arbitrary parameter λ_1, *i.e.* the known solution of the problem of flowing around a sphere (33) is not unique. The field (39) decreases at infinity as $1/r^2$ due to the neutron component (24), whereas the potential field (31) decreases as $1/r^3$.

The energetics of the flow around a sphere. The value of

$$\dot{\mathrm{I}} + \lambda_1\left(\mathrm{N} + \ddot{\mathrm{I}}\right) \tag{40}$$

is the inherent field of a streamlined sphere. The kinetic energy of the field momentum (40) K is

$$K = K_1 + K_2 + K_3 \tag{41}$$

Here

$$K_1 = \iiint_V \left(\dot{\mathrm{I}} \cdot \dot{\mathrm{I}}\right) \mathrm{d}V = \frac{\pi^2}{4} R w^2 \tag{42}$$

$$K_2 = \lambda_1^2 \iiint_V \left(\left(\mathrm{N} + \ddot{\mathrm{I}}\right) \cdot \left(\mathrm{N} + \ddot{\mathrm{I}}\right)\right) \mathrm{d}V = \frac{148\pi^2 \ddot{\mu}}{105 R^7} \tag{43}$$

Integration is performed with respect to the external part of the surface of the sphere. The values of K_1 and K_2 are the self-energies of the potential and the neutron components, respectively. The value of $\ddot{\mu}$ is arbitrary.

$$K_3 = 2\lambda_1 \iiint_V \left(\dot{\mathrm{I}} \cdot \left(\mathrm{N} + \ddot{\mathrm{I}}\right)\right) \mathrm{d}V = 0 \tag{44}$$

is the interaction energy of the potential and the neutron components.

The potential energy should be added to the kinetic energy (41) to get the total energy. The pressure p acts as the potential energy density for an incompressible fluid, whereas enthalpy for a compressible one. The pressure p can be derived from the equation of motion (14), substituting there the velocity (40) one obtains a complex differential equation. There is no point in solving it, since it is impossible to produce continuous flowing around a sphere.

2.2. Solution of the Problem of Flowing through the Sources on the Surface

Let us illustrate the solution of the problem of flowing using the example of flowing around a sphere with the radius R with the centre at the origin of the coordinates

$$z = \sqrt{R^2 - x^2 - y^2} \tag{45}$$

The modulus of the normal of the external flow to its surface, according to (30), is

$$w_n = w \cos \vartheta \tag{46}$$

Let a sphere be the source of the density of the momentum having only the radial component which at $r \to R - 0$ is equal to w_n, and at $r \to R + 0$ is equal to $-w_n$. In passing through the surface of the sphere the momentum density undergoes an abrupt change equal to $-2w_n$. It means that the surface of the sphere S is the carrier of the delta-function of the simple layer [2], and in (3) the function of the source in the spherical coordinates is

$$q\left(\mathrm{r}\right) = -w_n \delta_S \tag{47}$$

In the spherical coordinates only the radial component has the source on the sphere, the direction of the normal to the surface coincides with the coordinate line, therefore, the source (47) is a scalar. In the general case of an arbitrary surface it will be a vector. The flow of the vector w_n through the area element $\mathrm{d}S$ will be $w \cos \vartheta \mathrm{d}S$, its contribution to the potential at the point r will be

$$w \frac{\cos \vartheta_1}{\left|\mathrm{r} - \mathrm{r}_1\right|} \mathrm{d}S = \frac{w R^2 \cos \vartheta_1 \sin \vartheta_1}{\sqrt{r^2 - 2\gamma r R + R^2}} \mathrm{d}\vartheta_1 \mathrm{d}\varphi_1 = \frac{w R \varrho \cos \vartheta_1 \sin \vartheta_1}{\sqrt{1 - 2\gamma \varrho + \varrho^2}} \mathrm{d}\vartheta_1 \mathrm{d}\varphi_1 \tag{48}$$

The lower index 1 means that the given value refers to the sphere S, the radial component of the area element is $\mathrm{d}S = R^2 \sin\vartheta_1 \mathrm{d}\vartheta_1 \mathrm{d}\varphi_1$. The problem is axially symmetric relative to the z-axis, therefore, it is possible to assume $\varphi = 0$ without a loss of generality. The velocity potential is

$$\begin{aligned}\Phi &= -\nu \frac{wR\varrho}{4\pi} \int_0^{2\pi} \mathrm{d}\varphi_1 \int_0^{\pi} \frac{\sin\vartheta_1 \cos\vartheta_1}{\sqrt{1-2\gamma\varrho+\varrho^2}} \mathrm{d}\vartheta_1 \\ &= -\nu \frac{wR\varrho}{4\pi} \int_0^{2\pi} \mathrm{d}\varphi_1 \int_0^{\pi} \sin\vartheta_1 \cos\vartheta_1 \sum_{n=0}^{\infty} P_n(\gamma) \varrho^n \mathrm{d}\vartheta_1 \\ &= -\nu \frac{w}{3} \frac{R^2}{r^2} \cos\vartheta\end{aligned} \tag{49}$$

Here it is designated

$$\varrho = R/r \tag{50}$$

$$\gamma = \cos\vartheta \cos\vartheta_1 + \cos\varphi_1 \sin\vartheta \sin\vartheta_1 \tag{51}$$

ν is an arbitrary parameter. The expansion in terms of the Legendre polynomials is used

$$\frac{1}{\sqrt{1-2\gamma\varrho+\varrho^2}} = \sum_{n=0}^{\infty} P_n(\gamma) \varrho^n \tag{52}$$

One can show that

$$\int_0^{\pi} \mathrm{d}\vartheta_1 \int_0^{2\pi} P_n(\gamma) \sin\vartheta_1 \cos\vartheta_1 \mathrm{d}\varphi_1 = \frac{4\pi}{3} \begin{cases} \cos\vartheta, & n = 1 \\ 0, & n \neq 1 \end{cases} \tag{53}$$

The Legendre polynomial is expressed in this way [5]:

$$P_n(\gamma) = \frac{1}{2^n} \sum_{m=0}^{n_0} \frac{(-1)^m (2n-2m)!}{m!(n-m)!(n-2m)!} \gamma^{n-2m} \tag{54}$$

Here n_0 is equal to $n/2$ with even n and to $(n-1)/2$ in the case of odd n.

Differentiating (49) with respect to r and assuming $r = R$ one derives the value of the normal component on the surface of a sphere

$$w_n = \frac{2\nu w}{3R} \cos\vartheta \tag{55}$$

At $\nu = 3R/2$ the value of the normal component of the flow velocity on the surface of a sphere is equal to (46), *i.e.* the solution of the problem of flowing around a sphere.

The potential field of velocities is the convolution (19) with a function of a source (47):

$$-\nu w_n \delta_S \overset{S}{*} \frac{\mathrm{r}}{r^3} \tag{56}$$

The field

$$\left(-\nu w_n \delta_S \overset{S}{*} \frac{\mathrm{r}}{r^3} \right) + \mathrm{w} \tag{57}$$

has the normal component of the velocity of the flow on the surface of the

streamlined body equal to zero.

A complete solution of the problem of the continuous flow around a sphere is written in the form

$$w_n \delta_S \overset{S}{*} \left(\dot{\mathrm{I}} + \lambda_1 \left(\ddot{\mathrm{I}} + \mathrm{N} \right) \right) + \mathrm{w} \tag{58}$$

where the vectors $\dot{\mathrm{I}}, \ddot{\mathrm{I}}, \mathrm{N}$ are given by the relations (31), (35), (24). The vector

$$w_n \delta_S \overset{S}{*} \left(\mathrm{N} + \ddot{\mathrm{I}} \right) \tag{59}$$

on the surface of a sphere will have a zero radial component of the velocity.

If one takes the arbitrary closed surface S as the S in (58), then the function of the source will be a vector value in the form

$$\mathrm{q}(\mathrm{r}) = \mathrm{w}_n \delta_S \tag{60}$$

and (58) will be written as

$$\mathrm{w}_n \delta_S \overset{S}{*} \left(\dot{\mathrm{I}} + \lambda_1 \left(\ddot{\mathrm{I}} + \mathrm{N} \right) \right) + \mathrm{w} \tag{61}$$

The function (61) is the solution of the Equation (3) and it is a general solution of the problem of flowing by a steady flow around an arbitrary surface S in the quadrature form and not only around a sphere. According to (28), for a complete solution one should add the multipoles to (61).

To single out a solution that could be physically realisable, it is necessary to add some additional conditions to the boundary ones, e.g. the requirement for the minimum of the total energy of the system. There can be also other conditions.

There is an opinion that the continuous solution of the continuity equation in the problems of flowing when there are no viscous stresses will be a solution that is physically realisable. Broken and stalled flows are ignored in the consideration without explanation. However, stalled flows can have a total energy less than continuous ones, and they are physically realisable. It takes place under flowing round a sphere, and the noncontinuous solution with the formation of vortices is implemented. Nowadays the occurrence of stalled flows is explained by the effect of viscous stresses, which is impossible. Below in section 4 it is shown that viscous stresses do not exist in nature.

3. Inertial Effects

Vortices in a flow occur under stalled flow when a low-density zone is formed behind a streamlined body, which is clearly seen in flowing around an orthogonal plate (**Figure 3**).

The contribution of viscosity into the flow energetics is small because viscosity is essential only at the sides of the plate A and B with a small length. This contribution is much less than the kinetic energy of the vortices formed behind a streamlined plate. The vortex diameter is comparable with its length rather than with its thickness which is much less than the vortex diameter. Therefore, it is

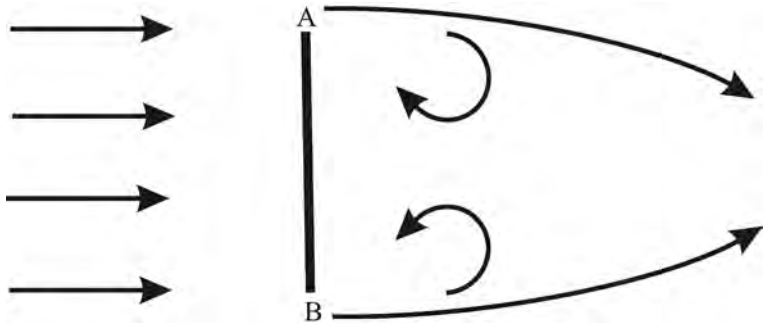

Figure 3. Shown is a thin plate located perpendicular to the running flow. The thickness of its slides at points A and B is much less than the diameter of the vortices occurring behind the plate.

impossible to correlate the formation of vortices with viscosity.

The appearance of the angular velocity (12) is related to the nonpotential character of the flow. However, it changes in the flow from point to point, it is impossible to single out regions rotating as a whole like a solid with the angular velocity similar for all of its points [6]. By the term "vortex" we will understand a fluid domain rotating in such a way that at each point of the domain the angular velocity is approximately the same.

The principal question is which moments of force produce vortices. Pressure cannot produce them in principle, since its force is the pressure gradient, which is a potential value and its work along a closed contour is always zero. If there are no external forces, only the forces produced by the pressure act in a fluid.

Let us consider a fluid ring in a flow with the radius r and the thickness dr. The element of the ring mass in the cylindrical coordinates is

$$\rho r \mathrm{d}r \mathrm{d}\varphi \tag{62}$$

Its moment of inertia is

$$\int_0^{2\pi} \rho r^2 \mathrm{d}r \mathrm{d}\varphi = 2\pi\rho r^2 \mathrm{d}r \tag{63}$$

Let the volume force that in the cylindrical coordinates has only one azimuth component with the density βr (β is the proportionality coefficient) act on a fluid (**Figure 4**). Due to this force, the element of mass (62) is affected by the moment

$$\beta\rho r^2 \mathrm{d}r \mathrm{d}\varphi \tag{64}$$

Integrating this expression with respect to φ from 0 to π, one derives the moment of force acting on the ring

$$2\pi\beta\rho r^2 \mathrm{d}r \tag{65}$$

Dividing the moment of force (65) by the moment of inertia (63) one gets that the angular acceleration of the ring is β, a constant value. The constants of the angular acceleration is needed for the fluid domain to spin like a solid with the same value of the angular acceleration of all the domain points.

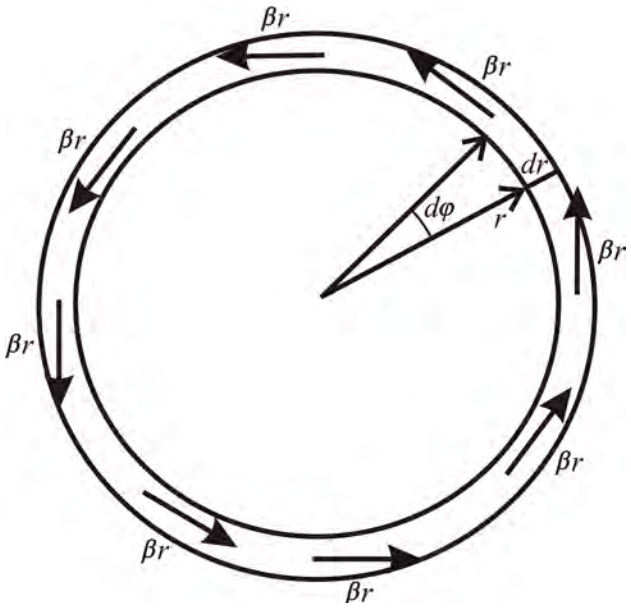

Figure 4. Shown is the fluid ring, with the volume force of the density βr having only one azimuth component applied to each point on the ring.

Let a flow be formed, due to the differences of the pressure, with the acceleration field

$$\mathrm{a} = \{\gamma y, 0\} = \gamma r \left\langle \cos\varphi \sin\varphi, -\sin^2\varphi \right\rangle \tag{66}$$

here γ is some coefficient of proportionality. In the broken brackets the value of the vector in the polar coordinates is shown. The acceleration in (66) has a linear dependence on the coordinate. This dependence can be obtained with an arbitrary field of acceleration by means of expansion into the Tailor series near the centre of the domain mass centre

$$a_i(x,y) = a_i(0,0) + \frac{\partial a_i}{\partial x_j}(0,0)\mathrm{d}x_j \tag{67}$$

The origin of the coordinates is in the centre of the domain mass.

The moment of the force acting on the ring with the inner radius r and the external radius $r+\mathrm{d}r$ will be derived by the multiplication of the azimuth component in (66) by $\rho r\mathrm{d}r$ and the integration with respect to φ from 0 to 2π. As a result, one obtains

$$-\pi\rho r^2\mathrm{d}r \tag{68}$$

Comparing (65) and (68) one can see that the acceleration field (66) has the moment of force acting on the ring that ensures spinning of the fluid domain like a solid having the same acceleration at each point.

The rotor $\nabla\times\mathrm{a}$ is the angular acceleration. If in a fluid the angular acceleration is a constant value for all the domain points, this domain produces a vortex.

The moment of force can be applied only to an object possessing the moment of inertia, which means that the object has to possess finite dimensions. A

material point has no moment of inertia. The moment of inertia is a characteristic taking into account the inertial properties of a system. The modern theory of hydrodynamics gives them little attention. As a result, the mechanism of the formation of vortices is disregarded. The mathematical description of a flow is made using the system of differential equations, *i.e.* a flow is considered at each point without integral characteristics. For instance, flowing around a sphere is one of the problems where the stalled character of a flow with the formation of vortices is manifested. All attempts to describe it taking into account viscous stresses are a failure.

4. Momentum Diffusion

At present it is considered that in the flow of a gas or a fluid there exist tangent or the so-called viscous stresses, their value, according to the Newton law is

$$p_{ij} = \nu \frac{\partial V_i}{\partial x_j} \tag{69}$$

Here ν is the viscosity coefficient, p_{ij} is the stress tensor and the nondiagonal components in it are the viscous stresses [1]. The equation of motion (10) has the form

$$\frac{\partial V_i}{\partial t} + V_j \frac{\partial V_i}{\partial x_j} = \frac{1}{\rho} \frac{\partial p_{ij}}{\partial x_j} \tag{70}$$

The physical reasons for the pressure in a gas and a condensed media are principally different. In the case of a gas, the pressure on the surface is produced only due to the collision of the molecules moving chaotically with the surface. So the source of the pressure in a gas is the kinetic energy of the molecules. The potential energy of the intermolecular interaction does not make contribution to the pressure, since the average distance between the molecules is much larger than the radius of the action of the interatomic forces. This property of a gas is the reason for the implementation of the thermodynamic relations, in particular, the Clapeyron-Mendelyeev law. For the tangential stresses to exist, it is necessary that the molecules be located near the equilibrium position and if they move there would be a force making them return to the previous position.

In condensed media the situation is different. The molecules are at distances at which the potential energy of the interatomic interaction is great, it has to be overcome in compression or tension and due to it the pressure is produced. Therefore, the dependencies of the density on the pressure for condensed media and gases are different. The interatomic interaction is responsible for the existence of the tangential stresses in the solids in which the average kinetic energy of the thermal atomic vibrations is lower than the potential barrier height for a shear. In fluids these energies are of the same order, the energy barrier for a shear is escaped by the thermal vibrations, which causes the flow of a fluid and its inability to resist a shear. Neither a fluid nor a gas can have tangential stresses, which is especially evident in the case of a gas. The point of mechanics on the

existence of viscous tangential stresses is erroneous, their inclusion in the equation of motion leads to an incorrect mathematical description of a flow.

In a gas the momentum of a molecule relative to the solid surface can be resolved into the normal and tangential components. In the collision against the wall both components of the molecule can change, since the surface is formed by the atomic sequences. A change of the normal component always leads to a transfer of the surface momentum in one direction—along the normal inside the wall. When the tangential component changes, the molecule has a force effect on the wall in the tangential direction. However, due to the stochastic character of motion, if the average tangential component of the momentum is zero, the gas is immobile, then the average tangential effect on the wall is also zero. When the average tangential momentum projection is not zero and is equal to w, the gas moves along the wall at the velocity w, the reflected molecules transfer to the wall part of the average potential momentum, the wall retards the gas and offers a viscous resistance.

The same happens under a motion inside a gas. If the derivative of the gas velocity in the direction perpendicular to the streamlines is not zero, in the adjacent layers the average velocities of the gas molecules are not the same: the molecules of the layer moving faster penetrate into the slower one and colliding against its molecules transfer an excess momentum. And vice versa, the molecules from the slower layer pass into the faster one retarding it. Thus, the momentum diffusion results in the occurrence of the momentum sources and discharges in the gas volume.

The boundary layer should be considered a diffusion layer, which is described by the equation of diffusion.

A change of the momentum of the elementary volume $\mathrm{d}Q$ is caused by two reasons. First, by the effect of the external forces on the volume $\mathrm{d}Q$ such as the difference of the pressure. Second, by the addition of the momentum to the volume $\mathrm{d}Q$ by diffusion. The total value of the change in the momentum is their sum. The momentum is a vector, one should consider the diffusion blow-in of each of its component through the surface of the elementary volume. Its entry for the time $\mathrm{d}t$ is

$$\mathrm{d}J_i = \eta\nabla\cdot\left(\nabla I_i\right)\mathrm{d}t \tag{71}$$

Here η is the coefficient of the momentum diffusion.

The momentum increment dI is the sum $\mathrm{dI} = \mathrm{dI}_1 + \mathrm{dJ}$, dI_1, we shall call it a force increment, it is produced by the difference of the pressure p and the external forces. The diffusion momentum dJ changes the momentum of the elementary volume even if there is no difference of the pressure and the external forces. Unlike dI_1, it does not enter the Bernoulli Equation (16). This division is somewhat arbitrary, it serves to illustrate the role of each phenomenon.

If due to the diffusion the momentum (71) is added to the material particles, then its velocity should increase by the value $\mathrm{d}u = \left(\mathrm{d}J/\mathrm{d}Q\right)/\rho$ and the surrounding particles will continue to move at the previous velocity, which

contradicts the continuity Equation (3). Therefore, the momentum transferred by the diffusion is divided into two parts

$$\mathrm{dJ} = \mathrm{d}\hat{\mathrm{J}} + \mathrm{d}\bar{\mathrm{J}} \tag{72}$$

here $\mathrm{d}\hat{\mathrm{J}}$ is the part of the momentum that passes into the velocity of the particle and part of the $\mathrm{d}\bar{\mathrm{J}}$, due to the retardation by the environment, passes into the additional pressure

$$\mathrm{d}p = \frac{\left(\mathrm{d}\bar{J}\right)^2}{2\rho} \tag{73}$$

and this excess pressure affects the motion of the surrounding particles in accordance with the equation of motion (11). Note that here, unlike the force momentum I_1, an increase in the velocity can result in an increase in the pressure. For a number of problems the value of $\mathrm{d}\hat{\mathrm{J}}$ is much higher than $\mathrm{d}\bar{\mathrm{J}}$ and it can be neglected in the first approximation $\mathrm{d}\bar{\mathrm{J}}$.

The diffusion momentum J is derived from the diffusion equation

$$\frac{\partial J_i}{\partial t} = \eta \sum_{j,k=1}^{3} \frac{\partial^2 I_i}{\partial x_j \partial x_k} \tag{74}$$

The double summation in this formula is related to the fact that each component of the momentum contributes to the diffusion through all sides of the elementary cube. Besides, in the right side there is the total momentum, whereas in the left one there is the diffusion momentum. This is because the diffusion is produced by the difference in the total momentum, and only the diffusion part of the momentum appears as a result of the diffusion.

For some problems it is possible to separate the force and the diffusion parts, for instance, for the diffusion in a stationary fluid when $\mathrm{I}_1 = 0$, with only the diffusion part of the momentum remaining. The Equation (74) for this case is written as

$$\frac{\partial J_i}{\partial t} = \eta \sum_{j,k=1}^{3} \frac{\partial^2 J_i}{\partial x_j \partial x_k} \tag{75}$$

The diffusion momentum corresponds to the appearance of the volume sources of the momentum with a power equal to the right side (74). These should be added to the continuity Equation (3) and, as a result, one obtains

$$\nabla \mathrm{I} = q(\mathrm{r}) + \eta \sum_{j,k=1}^{3} \frac{\partial^2 I_i}{\partial x_j \partial x_k} \tag{76}$$

From the point of view of mathematics one should solve simultaneously the equation of the momentum diffusion (74), the continuity Equation (76), the equation of motion (10), which is a complicated task. It is simpler to solve them one after another: to solve the diffusion equation as the first approximation, for the second approximation to derive the momentum taking into account the diffusion sources from the continuity Equation (76) and from the equation of motion to specify the field of velocities. In the present work the focus is on the

first approximation, *i.e.* the solution of the diffusion equation.

Momentum diffusion near a flat plate. Let us consider a problem in the two-dimensional statement when there is no dependence on the coordinate z and the vectors have only two components along the abscissa and the ordinate. Let some infinite space be occupied by a stationary fluid, therefore, one can use the diffusion Equation (75). At the origin of the coordinates at the moment $t=0$ there occurs an instaneous point source of momentum directed along the axis of abscissa

$$\mathrm{J}=\{J,0\}=\{J_0\delta(x)\delta(y)\delta(t),0\} \tag{77}$$

and it diffuses into the surrounding space. Here J_0 is the power of the momentum source. Physically the above momentum could be produced in the following way.

Let in a stationary gas parallel to the axis of abscissa at the origin of the coordinates there be a thin strip of the width dl, which at the moment of time $t=0$ moves jumpwise at the distance dx along the abscissa (Figure 5). The gas interacts with the surface of the strip due to the molecule collision. While the strip is immobile, it does not affect the distribution of the molecular velocities. If the strip moves, then due to the collisions of the gas molecules with it, the latter are imparted the momentum, so around the strip there appears a macroscopic motion of the gas diffusing into the surrounding space.

The equation of the momentum diffusion is written as

$$\frac{\partial J}{\partial t}-\eta\left(\frac{\partial^2 J}{\partial x^2}+\frac{\partial^2 J}{\partial y^2}\right)=J_0\delta(x)\delta(y)\delta(t) \tag{78}$$

If a fluid moves along the abscissa at the velocity $-w$, then the derivative with respect to time in (78) should be considered total and then (78) is written as

$$\frac{\partial J}{\partial t}-w\frac{\partial J}{\partial x}-\eta\left(\frac{\partial^2 J}{\partial x^2}+\frac{\partial^2 J}{\partial y^2}\right)=J_0\delta(x)\delta(y)\delta(t) \tag{79}$$

For the stationary case $\partial J/\partial t=0$ and the point source constant in time, $\delta(t)$ is replaced by unity and (79) changes to

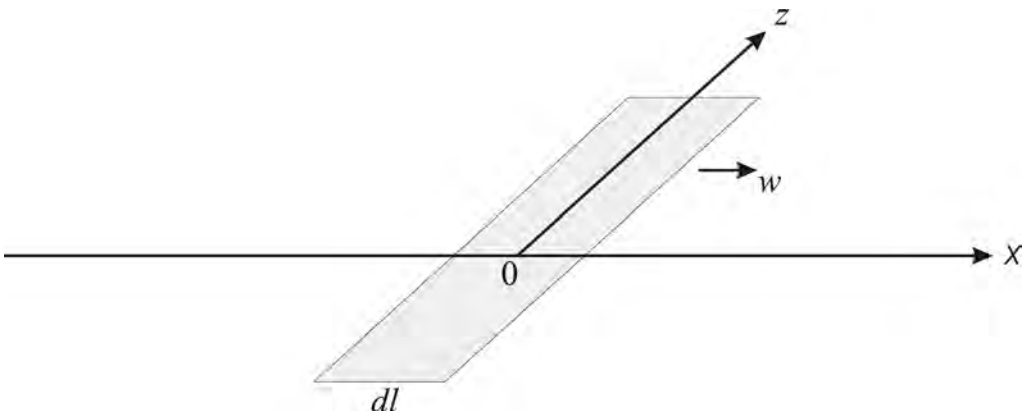

Figure 5. Shown is the thin strip located along the z-axis moving jumpwise along the abscissa.

$$w\frac{\partial J}{\partial x}+\eta\left(\frac{\partial^2 J}{\partial x^2}+\frac{\partial^2 J}{\partial y^2}\right)=-J_0\delta(x)\delta(y) \tag{80}$$

If a fluid is immobile $w=0$, then (79) is written as

$$\frac{\partial J}{\partial t}-\eta\left(\frac{\partial^2 J}{\partial x^2}+\frac{\partial^2 J}{\partial y^2}\right)=J_0\delta(x)\delta(y)\delta(t) \tag{81}$$

Let us introduce the scales of the distance L, the time t_m, the momentum $J_m=J_0/L^2$ then the variables are brought to the dimensionless form using the formulas $x=L\chi$, $y=L\zeta$, $t=t_m\tau$, $J=J_m\Upsilon$. Due to the arbitrariness of the scales of L and t_m, the following equalities should be fulfilled

$$\eta=L^2/t_m \tag{82}$$

$$w=L/t_m \tag{83}$$

then the scales are written as

$$t_m=\frac{\eta}{w^2} \tag{84}$$

$$L=\frac{\eta}{w} \tag{85}$$

$$J_m=J_0\frac{w^2}{\eta^2} \tag{86}$$

The Equation (79) is written as

$$\frac{\partial\Upsilon}{\partial\tau}-\frac{\partial\Upsilon}{\partial\chi}-\frac{\partial^2\Upsilon}{\partial\chi^2}-\frac{\partial^2\Upsilon}{\partial\zeta^2}=\delta(\chi)\delta(\zeta)\delta(\tau) \tag{87}$$

Here the property of the δ-function $\delta(L\chi)=\delta(\chi)/L$ is used. No parameters enter this equation. The Equation (87) describes the evolution of the dimensionless momentum in the dimensionless coordinates and time.

For estimation let us take the following values of the parameters in (115): $\eta=10^{-5}\,\mathrm{m}^2/\mathrm{s}$, $w=1\,\mathrm{m/s}$. The viscosity coefficient of the air is $1.5\times10^{-5}\,\mathrm{m}^2/\mathrm{s}$, then $L=10^{-5}\,\mathrm{m}$, $t_m=10^{-5}\,\mathrm{s}$.

The Equation (87) for a stationary fluid is written as

$$\frac{\partial\Upsilon}{\partial\tau}-\frac{\partial^2\Upsilon}{\partial\chi^2}-\frac{\partial^2\Upsilon}{\partial\zeta^2}=\delta(\chi)\delta(\zeta)\delta(\tau) \tag{88}$$

For the equation in a stationary fluid (81) the velocity $w=0$, therefore, (83) disappears and the scales L and t_m are chosen quite arbitrary. Since further I am planning to turn from a stationary fluid to that moving at the velocity w, the choice of the scales (84) - (86) is the same for the Equation (88).

The stationary Equation (80) for a fluid moving at the velocity equal to unity is presented in the dimensionless variables like

$$\frac{\partial\Upsilon}{\partial\chi}+\frac{\partial^2\Upsilon}{\partial\chi^2}+\frac{\partial^2\Upsilon}{\partial\zeta^2}=-\delta(\chi)\delta(\zeta) \tag{89}$$

Here (84) - (86) are used as the scales.

The value J_0. The average distance between the molecules λ from the Clapeyron-Mendelyeev law is written as

$$\lambda = \left(\frac{RT}{pN_A}\right)^{1/3} = \left(\frac{kT}{p}\right)^{1/3} \tag{90}$$

Here $R = N_A k$ is the gas constant, k is the Boltzmann constant, N_A is the Avogadro number, T is the absolute temperature, p is the gas pressure. For the air λ is by an order of magnitude larger than the interatomic distance in condensed substances.

The average velocity of the progressive motion of a molecule along the normal to the strip is

$$\overline{v} = \sqrt{\frac{kT}{\mu}} \tag{91}$$

Here μ is the molecule mass. This relation is valid for monoatomic gases. For polyatomic gases the dependence (91) between the temperature and the progressive velocity at high temperatures is more complicated due to the contribution of the molecule rotations and the intramolecular vibrations. Here the gases are considered for which the relation (91) is fulfilled. The time during which a molecule will cover the length λ will be equal to

$$\overline{t} = \frac{\lambda}{\overline{v}} = \left(\frac{\mu^3}{p^2 kT}\right)^{1/3} \tag{92}$$

The average length of the free path of the molecules in a gas is much larger than λ, it is possible to neglect the colliding ones and consider that half the molecules located at the distance λ from the strip reach its surface since the other half of them move back from it. From the Clapeyron-Mendelyeed equation one derives the number of the moles contained in the volume $\mathrm{d}V = \lambda \mathrm{d}l$ per unit of length along the coordinate z

$$\frac{p\mathrm{d}V}{RT} = \frac{p\lambda}{RT}\mathrm{d}l \tag{93}$$

Then the number of the molecules reaching the strip is such

$$\frac{p\lambda \mathrm{d}l}{2RT} N_A = \frac{1}{2}\left(\frac{p}{kT}\right)^{\frac{2}{3}} \mathrm{d}l \tag{94}$$

After the collision with the moving strip each molecule will receive from the plate the average momentum $\alpha\mu w$ directed along the abscissa. The value of α determines the average value of the transferred tangential momentum in the collision of a gas molecule with the atoms of the wall, w is the velocity of the motion of the strip in a jump. Multiplying this value by (94) one derives the momentum transferred from the plate to the gas due to the molecular interaction during the time of the elementary jump $\overline{t}$ in the form

$$J_0 = \frac{\alpha\mu w}{2}\left(\frac{p}{kT}\right)^{2/3} \mathrm{d}l \tag{95}$$

J_0 is the momentum per unit of the length of the plate along the *z*-axis.

Moving source. The continuous motion of the point source of the momentum at the velocity w can be presented in the following way. Let us take the plate length equal to $\mathrm{d}l = w\mathrm{d}t$. Then (95) will be written as

$$J_0 = w^2\omega\mathrm{d}t = \eta\omega\mathrm{d}\tau \tag{96}$$

Here the Equations (84)-(86) are used,

$$\omega = \alpha\frac{\mu}{2}\left(\frac{p}{kT}\right)^{\frac{2}{3}} \tag{97}$$

Let the plate be located at the moment of time $t_N = -N\mathrm{d}t$ on the negative part of the axis of abscissa at the point $x_N = -N\mathrm{d}l = -Nw\mathrm{d}t$ and then caused to move at the distance $\mathrm{d}l$ during the time $\mathrm{d}t$. Here N is the natural number. As a result, it will arrive at the point of the axis of abscissa $x_{N-1} = -(N-1)w\mathrm{d}t$. From this point at the moment of time $t_{N-1} = -(N-1)\mathrm{d}t$ it repeats a jump and gets to the point x_{N-2} and so on. In the time $t_n = n\mathrm{d}t$ it will make n jumps and find itself at the point of the axis of abscissa $x_n = (N-nw)\mathrm{d}t$. At the moment of the time $t = 0$, when $n = N$, the plate will be at the origin of the coordinates. With each jump the plate produces the diffusion field described by the Equation (78) whose solution is [2]:

$$J(x - wt_n, y, t_n) = J_0\frac{\theta(t-t_n)}{4\pi\eta(t-t_n)}\exp\left[-\frac{(x-wt_n)^2 + y^2}{4\eta(t-t_n)}\right] \tag{98}$$

Summing (98) with respect to n from 0 to N one obtains the solution of the problem on the evolution of the field of the diffusion momentum produced by the moving point source of the momentum in the stationary fluid from time $t = t_N < 0$ to time $t = 0$:

$$\begin{aligned}\hat{J}(x,y,t) &= \sum_{n=0}^{n=N} J(x - wt_{N-n}, y, t - t_{N-n}) \\ &= \frac{w^2\omega}{4\pi\eta}\mathrm{d}\tau\sum_{n=0}^{n=N}\frac{1}{t-t_{N-n}}\exp\left[-\frac{(x-wt_{N-n})^2 + y^2}{4\eta(t-t_{N-n})}\right]\end{aligned} \tag{99}$$

With the elementary jump $\mathrm{d}l \to 0$, this sum changes to the integral

$$\hat{J}(x,y,t) = \frac{u^2\omega}{4\pi\eta}\int_{t_N}^{0}\frac{1}{t-t_1}\exp\left[-\frac{(x-wt_1)^2 + y^2}{4\eta(t-t_1)}\right]\mathrm{d}t_1 \tag{100}$$

$\hat{J}(x,y,t)$ is the solution of (80) for $t > t_N$, since for $t < t_N$ the momentum $\hat{J}(x,y,t) = 0$ due to $\theta(t-t_N) = 0$. If $t_N < t < 0$, then in the sum in (99) summing should be interrupted when $t_{N-n} > t$ and the upper limit in the integral will be t rather than 0. Thus, (100) is the solution of the problem when at the moment $t = t_N$ at the point $x = wt_N$ of the axis of abscissa there appears the momentum source and moves in the positive direction, while at the moment of time $t = 0$ it disappears. In this case, the upper limit in the integral in (100) is zero. If after the moment $t = 0$ the momentum source continues to move, its

upper limit in (100) should be t, and the solution will be written as

$$\bar{J} = \frac{u^2\omega}{4\pi\eta}\int_{t_N}^{t}\frac{1}{t-t_1}\exp\left[-\frac{\left(x-wt_1\right)^2+y^2}{4\eta\left(t-t_1\right)}\right]\mathrm{d}t_1 \tag{101}$$

Note that as a result of the summation, the momentary character in time of the point source disappears, it becomes constant in time during its movement due to the summation. However, the momentum character of the spatial coordinates remains but changes to the form $\delta\left(x-wt\right)\delta\left(y\right)$.

At $t_N \to -\infty$ (101) changes to

$$\hat{J} = \frac{w^2\omega}{4\pi\eta}\int_{-\infty}^{t}\frac{1}{t-t_1}\exp\left[-\frac{\left(x-wt_1\right)^2+y^2}{4\eta\left(t-t_1\right)}\right]\mathrm{d}t_1 \tag{102}$$

Substituting $t_2 = t - t_1$ in (102) and turning to the moving system of the coordinates $\dot{x}, y$ the substitution of $\dot{x} = x - wt$ one derives

$$\tilde{J} = \frac{w^2\omega}{4\pi\eta}\int_{0}^{\infty}\frac{1}{t_2}\exp\left[-\frac{\left(\dot{x}+wt_2\right)^2+y^2}{4\eta t_2}\right]\mathrm{d}t_2 \tag{103}$$

In this system of the coordinates the stationary point momentum source is located at the origin of the coordinates, and the fluid moves along the axis of abscissa at the velocity $-w$. The function (103) is the solution of the stationary equation of diffusion in the moving fluid with the point momentum source at the origin of the coordinates (80).

Using the values (84)-(86) as the scales the solution (103) in the dimensionless form will be presented as

$$\Upsilon = \frac{1}{4\pi}\int_{0}^{\infty}\frac{1}{\tau}\exp\left[-\frac{\left(\chi-\tau\right)^2+\zeta^2}{4\tau}\right]\mathrm{d}\tau \tag{104}$$

Here $\chi = \dot{x}/L$, $\tau = t_2/t_m$, $\zeta = y/L$.

From (104) it follows that the solution does not depend on the time, and the integral is the function of only two dimensionless spatial coordinates χ, ζ. Let us show that (104) is the solution of the stationary equation of diffusion in the moving fluid (89). Substituting the function (104) into (89) one obtains

$$\int_{0}^{\infty}\frac{\Lambda}{\tau^3}\exp\left[-\frac{\left(\chi-\tau\right)^2+\zeta^2}{4\tau}\right]\mathrm{d}\tau \equiv 0 \tag{105}$$

Here it is designated

$$\Lambda = \chi^2 + \zeta^2 - 4\tau - \tau^2 \tag{106}$$

For the Equation (104) to be the solution of the equation (89), it is necessary that (105) be zero at any values of χ, ζ. I have failed to analytically prove it, however, the numerical calculation (105) supports it.

The sign Λ determines the sign of the integrand in (105). The equation $\Lambda = 0$ has only one positive root

$$\tau_* = \sqrt{4+\chi^2+\zeta^2} - 2 \tag{107}$$

At $0<\tau<\tau_*, \Lambda>0$, and at $\tau>\tau_*, \Lambda<0$. The integrand in (105) exponentially tends to zero both at $\tau\to 0$ and $\tau\to+\infty$. Really, $\Lambda\sim\tau^2$ at $\tau\to+\infty$, and the exponent in (105) tends to zero, since its index $\to-\infty$ at $\tau\to\infty$.

At any values of χ,ζ the following equality takes place

$$I_1(\chi,\zeta)=-I_2(\chi,\zeta) \tag{108}$$

Here it is designated

$$I_1(\chi,\zeta)=\int_0^{\tau_*}\frac{\Lambda}{\tau^3}\exp\left[-\frac{(\chi-\tau)^2+\zeta^2}{4\tau}\right]\mathrm{d}\tau \tag{109}$$

$$I_2(\chi,\zeta)=\int_{\tau_*}^{\infty}\frac{\Lambda}{\tau^3}\exp\left[-\frac{(\chi-\tau)^2+\zeta^2}{4\tau}\right]\mathrm{d}\tau \tag{110}$$

As an example, Figure 6 shows the results of the calculation of the integrals $I_1(\chi,\zeta)$ and $I_2(\chi,\zeta)$ for the abscissa $\chi=1$ and the ordinate ζ within the interval $(0,6)$. The curves in the plot are symmetric relative to the axis ζ, hence it follows that the equality (108) is fulfilled.

Note that the identity (105) is valid even for a more general form of the functions at the arbitrary ς

$$\int_0^{\infty}\frac{\Lambda}{\tau^3}\exp\left[-\frac{(\chi-\varsigma\tau)^2+\zeta^2}{4\tau}\right]\mathrm{d}\tau\equiv 0 \tag{111}$$

The plate of a finite length. To consider flowing around the plate with a finite length $\mathcal{L}$, it is necessary to use the momentum function $\delta_{\mathcal{L}}$, its carrier is the segment $\mathcal{L}$, *i.e.* to use the notion of a simple layer. It is determined as [2]

$$f(x,y)\overset{\mathcal{L}}{*}\mathcal{L}=\int_{t\in\mathcal{L}} f\big(x(t),y(t)\big)\mathrm{d}t \tag{112}$$

The plate length in the dimensionless form is

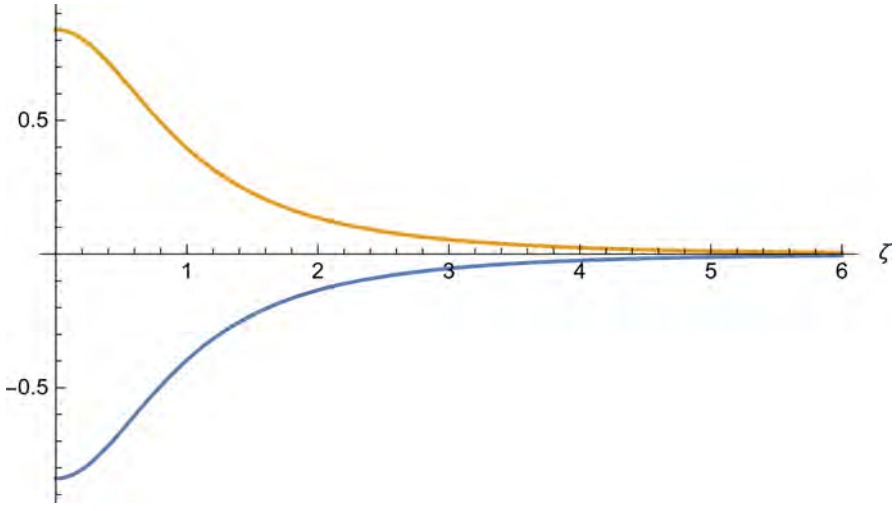

Figure 6. Plot of the functions $I_1(\chi,\zeta)$—(the upper curve) and $I_2(\chi,\zeta)$—(the lower curve) for $\chi=1$ $\zeta\in(0,6)$.

$$\lambda = \frac{\mathcal{L}}{L} \tag{113}$$

The equation (89) is written as

$$\frac{\partial \Upsilon}{\partial \chi} + \frac{\partial^2 \Upsilon}{\partial \chi^2} + \frac{\partial^2 \Upsilon}{\partial \zeta^2} = -\delta_\lambda \tag{114}$$

Here δ_λ is the δ-function with the carrier the segment λ in the dimensionless variables. Using (104), one derives the solution of the Equation (114) [2]

$$\begin{aligned} \Upsilon(\chi,\zeta) &= \int_0^\lambda \hat{\Upsilon}(\chi - s,\zeta)\,\mathrm{d}s = \frac{1}{4\pi}\int_0^\infty \mathrm{d}\tau \int_0^\lambda \frac{1}{\tau}\exp\left[-\frac{(\chi - s + \tau)^2 + \zeta^2}{\tau}\right]\mathrm{d}s \\ &= \frac{1}{8\sqrt{\pi}}\int_0^\infty \frac{1}{\sqrt{\tau}}\exp\left(-\frac{\zeta^2}{\tau}\right)\left[\operatorname{erf}\left(\frac{\chi+\tau}{\sqrt{\tau}}\right) - \operatorname{erf}\left(\frac{\chi+\tau-\lambda}{\sqrt{\tau}}\right)\right]\mathrm{d}\tau \end{aligned} \tag{115}$$

Figures 7-9 show the diffusion momentum Υ versus the coordinate ζ for the assigned values of χ. The values of χ are shown on the left of the plot, which gives the values of the momentum on the straight lines orthogonal to the plate $\chi = \text{const}$. In Figure 7 these lines go through the plate, in Figure 8 they cross the axis of abscissa χ behind the plate. In Figure 9 they pass in front of the plate.

The plots are symmetric to the axis of abscissa χ as it follows from (115), therefore, it would be enough to show the plots only for $\zeta \geq 0$. However, their behavior on the axis of abscissa at $\zeta = 0$ is of interest, therefore, the left half of the profile is shown in the truncated form.

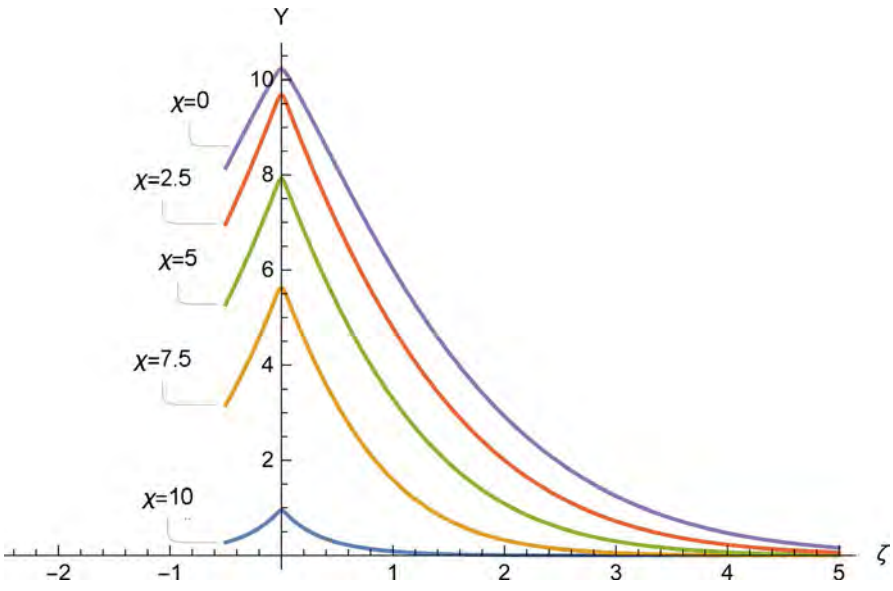

Figure 7. Plot of the diffusion momentum Υ near the plate when it is streamlined by a viscous fluid. The dimensionless length of the plate is 10 and it is located on the axis of abscissa χ at the interval $(0,10)$. The values of the coordinate χ are indicated on the left of the corresponding plot. The lower plot gives the values of the momentum at the beginning of the plate, the upper one at the end.

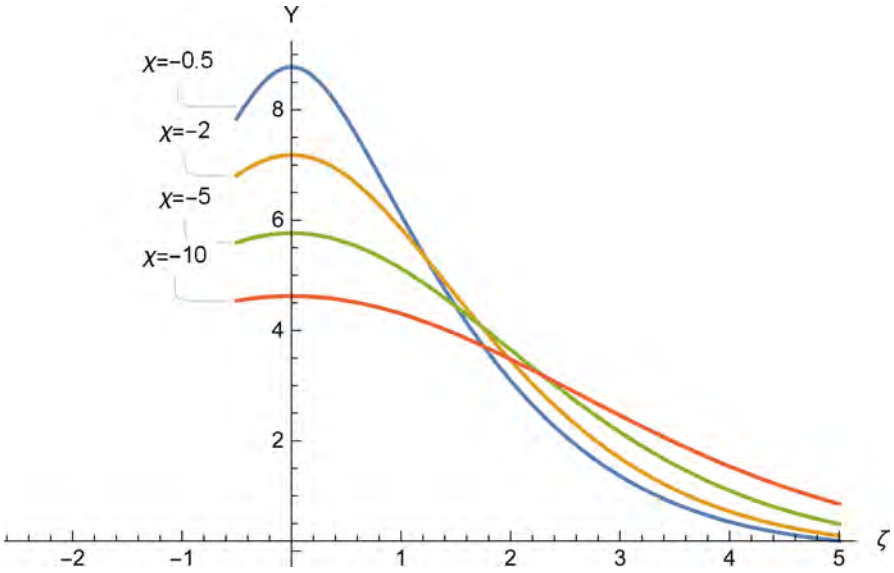

Figure 8. Plots of the momentum Υ behind the streamlined plate.

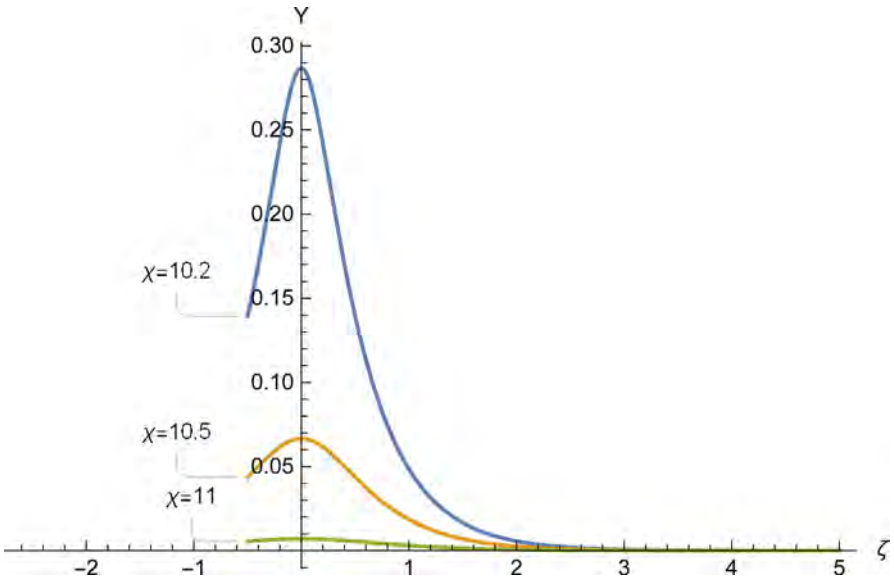

Figure 9. Profiles of the dimensionless momentum Υ in front of the plate.

In Figure 7 one can see that the plot of the momentum on the plate forms an acute angle, *i.e.* the derivative $\mathrm{d}\Upsilon/\mathrm{d}\zeta$ on the plate undergoes a break, which should be expected, since the plate is the momentum source. Outside the plate the momentum profile has an extremum with the continuous derivative $\mathrm{d}\Upsilon/\mathrm{d}\zeta = 0$.

In front of the plate there also exists a diffusion momentum shown in Figure 9. However, it disappears quickly with increasing distance from the plate up the flow.

The obtained results agree with the experimental data. The problem in the present theory of the boundary layer is the profile of the velocity near the front edge of the plate. The calculated profiles are much different from the measured

ones. The theory suggested here solves the above problem.

Flow in the cylindrical tube. As it has been shown here, the viscosity coefficient ν in (69) is a fictitous value, since there are no shear stresses in gases and fluids. There arises a question how the viscosity coefficient ν is related to the coefficient of the momentum diffusion η. One of the main methods of measurement of the viscosity coefficient is the flow in a cylindrical tube [1].

The rate of the flow through a cylindrical tube of the radius R under a laminar flow is [1]

$$\frac{\pi R^4}{8\nu}\frac{\Delta p}{l}=\frac{\pi R^4}{8\nu}P \tag{116}$$

Here $P=\Delta p/l$ is the difference of pressure per unit of the tube length.

For the stationary flow of a viscous fluid through a round tube of the radius R due to the viscosity there is a radial dependence of the velocity $u=u(r)$ that is smaller near the tube wall than on the axis. As the boundary condition let us take the adherence condition

$$u(r)=0,\quad r=R \tag{117}$$

The equation of the momentum diffusion for an incompressible fluid in the cylindrical coordinates is written as

$$\rho u\frac{\partial u}{\partial z}-\frac{\eta}{r}\frac{\partial}{\partial r}\left(r\frac{\partial u}{\partial r}\right)=P \tag{118}$$

The velocity u does not depend on z, then $\partial u/\partial z=0$ and this equation is brought to the form

$$-\frac{\eta}{r}\frac{\partial}{\partial r}\left(r\frac{\partial u}{\partial r}\right)=P \tag{119}$$

The solution of this equation is

$$u=\frac{P}{4\eta}r^2+c_4\ln r+c_5 \tag{120}$$

Here c_4 and c_5 are the arbitrary constants, from the limiting condition of the velocity it follows that $c_4=0$.

The value of the arbitrary constant c_5 is determined from the boundary condition (117).

In a general case, it is necessary to assign the momentum diffusion into the tube wall

$$u\big|_{r=R}=\alpha\tau \tag{121}$$

Here τ is the shear stress on the tube wall caused by the momentum diffusion into the tube wall, α is the proportionality coefficient otherwise called the friction coefficient. This variant of the boundary condition is fulfilled when "slipping" of the fluid along the tube wall takes place. From (117) one obtains

$$c_5 = -\frac{PR^2}{4\eta} \tag{122}$$

Finally, (120) is presented as

$$u(r) = \frac{P}{4\eta}\left(R^2 - r^2\right) \tag{123}$$

which completely coincides with the classical distribution of the velocities across the section of the tube [1]. The flow rate along the tube is determined by integrating (123) with respect to the tube section

$$\int_0^{2\pi} \mathrm{d}\varphi \int_0^R u(r)\,\mathrm{d}r = \frac{\pi R^4}{8\eta} P \tag{124}$$

The relations (116) and (124) coincide, which means that in the experiments on the measurement of the viscosity coefficient it is the coefficient of the momentum diffusion which is determined rather than that of viscosity.

Coefficients of the momentum diffusion and thermal conductivity. The relation of the viscosity coefficient to that of thermal conductivity is called the Prandtl number [1]. The mechanism of the momentum diffusion and the heat transfer is ensured in the same way—by the chaotic motion of the gas molecules and their collision. On the average for a monoatomic gas a kinetic energy of $kT/2$ falls at one degree of freedom and $3kT/2$ at three degrees of freedom, with the energy, *i.e.* the heat transferred by all three degrees of freedom. Unlike the heat transfer, the momentum has a definite direction, which is that of the flow of a fluid. The chaotic motion in this direction does not affect the transfer of the momentum that is transferred in the deterministic process. So only two directions remain for the diffusion. Therefore, the Prandtl number for monoatomic gases should be 2/3, which is really observed [7].

Superfluidity of helium. Fluid helium at a temperature below 2.6 K possesses superfluidity [8], *i.e.* the ability to flow at a large velocity through capillars, which means that the viscosity coefficient is either by orders of magnitude less than the known values or zero.

The diffusion mechanism of viscosity is responsible for superfluidity. At low temperatures the thermal energy of $3kT/2$ falling at a helium atom is small and by the laws of quantum mechanics the energy transfer is possible only by quanta. If the energy transferred is less than a quantum, then the momentum cannot be transferred from a streamlined body to helium atoms, which rules out its diffusion, which in turn means that the coefficient of cohesion in (95) $\alpha = 0$. Superfluidity is not the property of helium nor a phase transition leading to the disappearance of viscous stresses that do not exist in nature. It is the feature of the interaction of helium atoms with the atomic lattice of the surface at low temperatures.

One would suggest an alternative variant, e.g. at low temperatures the momentum cannot be transferred among the helium atoms and a streamlined surface, in this case, makes no difference, *i.e.* one deals here with a phase

transition. However, this variant does not work because at the above temperatures helium possesses thermal conductivity and the momentum is really transferred among the atoms.

In hydrodynamics d'Alembert's paradox is well-known: from the potential solution of the problem of the flow around a sphere by an incompressible ideal fluid it follows that the resistance of the flow is zero. However, helium does not manifest superfluidity in flowing around and the hydrodynamic resistance does exist. Superfluidity does not rule out the formation of stalled flows of helium, which produces resistance, according to the laws of hydrodynamics.

To explain superfluidity, a hypothesis [8] was suggested according to which at a temperature of 2.6 K in fluid helium there occurs a phase transition separating into two phases: a superfluid one with zero viscosity and a usual one, viscous. As it follows from the present article this is a mistake because there is no need to involve phase transitions to consider superfluidity.

5. Discussion

In theoretical hydrodynamics there exist serious delusions preventing one from theoretical understanding of flows.

1) Mathematical nonuniqueness of the solution of hydrodynamic problems. The classical potential solution of the problem of flowing around a sphere is not unique, there exist a nonpotential solution different from the classical one.

The nonuniqueness poses a problem of formulating additional conditions for choosing a physically realisable solution. Here the principle of the minimum total energy of a system, *i.e.* the sum of the kinetic and potential energies, is suggested as the above condition. The kinetic energy is determined by the momentum of a flow, and the potential one by the pressure for an incompressible fluid and the enthalpy for a compressible one. For the potential flow of an incompressible fluid the total energy density is the Bernoulli potential.

From the viewpoint of computational mathematics, nonuniqueness can result in the divergence of computational algorithms. Here the additional conditions that will depress the divergence and ensure a physically realisable solution are also important.

2) The neglect of the integral characteristics of the flow and the attention fixed only on the differential ones. As a result, the inertial properties of the flow are ignored in the consideration, and for this reason the mechanism of the formation of vortices by stalled flows is not clear. The formation of vortices is erroneously explained by the nonexisting viscous stresses. As a result, there is no mathematical theory of stalled flows even for the simplest problems, such as flowing around an orthogonal plate or a sphere. The consequence is also the absence of a consistent theory of turbulent flows.

3) The use of the viscous stresses that are fictious forces. They enter the equation of motion but do not exist in reality.

The momentum diffusion leads to the necessity of including into the continuity

equation the momentum sources caused by diffusion. The fictitious viscous stresses in the equation of motion result in the failure of the solution of hydrodynamic problems. For instance, it is impossible to obtain an adequate value of the profile of the velocities of a viscous fluid flowing around a flat plate.

The fictitious viscous stresses lead to the erroneous theory of the superfluidity of helium. Superfluidity is considered a phase transition under which the viscous stresses disappear. However, since they do not exist in nature, there is no phase transition. At low temperatures due to the small energy falling at a helium atom, the transfer of the momentum from the streamlined wall to helium atoms becomes impossible due to quantum effects. Superfluidity is manifested only during soaking of helium through capillars. In flowing around profiles there exists the hydrodynamic resistance as in usual fluids caused by the stalled character of the flow. Viscosity does not work here.

Then the fact that the Prandtl number for monoatomic gases is 2/3 finds the explanation.

The mathematical description of the flow of a viscous medium should include

- the equation of the momentum diffusion;
- the continuity equation that includes the diffusion momentum as the volume momentum source;
- the equation of motion without viscous stresses;
- the energy equation.

One should also take into account the integral characteristics of the flow and find the regions forming vortices. One should take into account nonuniqueness of the solution of a hydrodynamic problem and the existence of nonpotential solutions. It is necessary to include some additional conditions along with the initial and boundary ones to find a physically realisable solution, e.g. the condition of the minimum total energy of a system.

From the point of view of mathematics, there always exists a continuous solution of the continuity equation. However, there also exist broken solutions in which the region of the flow is divided into subregions inside which the flow is continuous, and on their borders there is a break of the tangent to the boundary of the velocity component. A broken solution can have the total system energy lower than the continuous one and, as a result, the latter solution is realised.

The above points should be taken into account in the theoretical solution of hydrodynamic problems and the development of the computational algorithms of their solution.

6. Conclusion

The analysis made here shows that at present in hydromechanics there exist serious gaps and erroneous notions both in the physical and mathematical aspects. These drawbacks block the application of theoretical hydrodynamics for the solution of practical problems and understanding of the processes related to

the flow. To avoid them, one should approach more strictly to the theoretical comprehension of the phenomena both from the viewpoint of physics and mathematics. For instance, if there is no proof of the uniqueness of the obtained solution of a physical problem, one should try to find another solution or a proof of the uniqueness. In physics it is necessary to keep watch on the correctness of the applied concepts. One should not use fictitious values as is the case of viscous stresses for a gas.

Conflicts of Interest

The author declares no conflicts of interest regarding the publication of this paper.

References

[1] Loytsanskii, L.G. (1974) Fluid Mechanics. Nauka, Moscow. (Russian)

[2] Vladimirov, V.S. (1981) Equations of Mathematical Physics. Nauka, Moscow. (Russian)

[3] Bazarov, I.P. (1991) Thermodynamics. Higher Scool, Moscow. (Russian)

[4] Ivanchin, A. (2017) Electrostatical Theory of Elementary Particles. http://www.scirp.org/journal/PaperInformation.aspx?PaperID=78462

[5] Korn, G.A. and Korn, T.M. (1968) Mathematical Handbook. McGraw-Hill Book Company, London.

[6] Landau, L.D. and Lifshitz, E.M. (1960) Mechanins. Pergamon Press Ltd., London.

[7] Kikoin, I.K. (ed.) (1990) Tables of Physical Values. *Biometrika*, **77**, 305-314.

[8] Landau, L.D. and Lifshitz, E.M. (1986) Theoretical Physics. Hydrodynamics, Nauka, Moscow. (Russian)

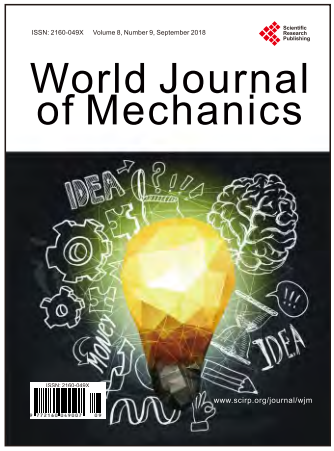

Call for Papers

World Journal of Mechanics (WJM)

ISSN 2160-049X (Print) ISSN 2160-0503 (Online)
http://www.scirp.org/journal/wjm

World Journal of Mechanics (WJM) is an international peer-reviewed journal dedicated to presenting the English original research studies, reviews in the general field of mechanics including the mechanics of solids, structures and fluids and their interaction.

Subject Coverage

This journal invites original research and review papers that address the following issues. Topics of interest include, but are not limited to:

- Applied Mathematics and Mechanics
- Biomechanics and Modeling in Mechanobiology
- Celestial Mechanics and Dynamical Astronomy
- Classical and Quantum Aspects of Mechanics
- Computational Mechanics
- Computer Methods in Applied Mechanics and Engineering
- Continuum Mechanics and Thermodynamics
- Damage Mechanics
- Dynamics and Vibration Control
- Elasticity and Plasticity
- Engineering Fracture Mechanics
- Environmental Fluid Mechanics
- Experimental Mechanics
- Fluid Mechanics and Aerodynamics
- Mathematical Fluid Mechanics
- Mathematics and Mechanics of Solids
- Mechanical Behavior of Biomedical Materials
- Mechanical Engineering Science
- Mechanical Systems and Signal Processing
- Mechanics & Astronomy
- Mechanics and Materials in Design
- Mechanics in Medicine and Biology
- Mechanics of Materials
- Mechanics of Time-Dependent Materials
- Microfluidics
- Micromechanics and Microengineering
- Multi-Scale Mechanics
- Nanomechanics
- Non-Linear Mechanics
- Non-Newtonian Fluid Mechanics
- Numerical and Analytical Methods in Geomechanics
- Probabilistic Engineering Mechanics
- Rock Mechanics and Mining Sciences
- Solid and Structural Mechanics
- Statistical Mechanics and Its Applications
- Terramechanics
- Theoretical and Applied Fracture Mechanics
- Thermophysics and Aeromechanics
- Thin Film Mechanics
- Viscoelasticity

We are also interested in short papers (letters) that clearly address a specific problem, and short survey or position papers that sketch the results or problems on a specific topic. Authors of selected short papers would be invited to write a regular paper on the same topic for future issues of World Journal of Mechanics.

Notes for Intending Authors

Submitted papers should not have been previously published nor be currently under consideration for publication elsewhere. Paper submission will be handled electronically through the website. All papers are refereed through a peer review process. For more details about the submissions, please access the website.

Website and E-Mail

http://www.scirp.org/journal/wjm E-mail: wjm@scirp.org

What is SCIRP?

Scientific Research Publishing (SCIRP) is one of the largest Open Access journal publishers. It is currently publishing more than 200 open access, online, peer-reviewed journals covering a wide range of academic disciplines. SCIRP serves the worldwide academic communities and contributes to the progress and application of science with its publication.

What is Open Access?

All original research papers published by SCIRP are made freely and permanently accessible online immediately upon publication. To be able to provide open access journals, SCIRP defrays operation costs from authors and subscription charges only for its printed version. Open access publishing allows an immediate, worldwide, barrier-free, open access to the full text of research papers, which is in the best interests of the scientific community.

- High visibility for maximum global exposure with open access publishing model
- Rigorous peer review of research papers
- Prompt faster publication with less cost
- Guaranteed targeted, multidisciplinary audience

Scientific Research Publishing

Website: http://www.scirp.org
Subscription: sub@scirp.org
Advertisement: service@scirp.org